ASSESSING THE SURFACE ENERGY BALANCE COMPONENTS

IN THE SNAKE RIVER BASIN

By

W Thilini Ajanthik Jaksa

A thesis

submitted in partial fulfillment

of the requirements for the degree of

Master of Science in Civil Engineering

Boise State University

August 2011

BOISE STATE UNIVERSITY GRADUATE COLLEGE

DEFENSE COMMITTEE AND FINAL READING APPROVALS

of the thesis submitted by

W Thilini Ajanthik Jaksa

Thesis Title: Assessing the Surface Energy Balance Components in the Snake River Basin

Date of Final Oral Examination: 02 May 2011

The following individuals read and discussed the thesis submitted by student W Thilini Ajanthik Jaksa, and they evaluated her presentation and response to questions during the final oral examination. They found that the student passed the final oral examination.

Venkataramana Sridhar, Ph.D. Chair, Supervisory Committee

Mandar Khanal, Ph.D. Member, Supervisory Committee

Arturo Leon, Ph.D. Member, Supervisory Committee

The final reading approval of the thesis was granted by Venkataramana Sridhar, Ph.D., Chair of the Supervisory Committee. The thesis was approved for the Graduate College by John R. Pelton, Ph.D., Dean of the Graduate College.

ACKNOWLEDGEMENTS

ABSTRACT

This study investigated the interaction of land-surface processes and vegetation in both natural ecosystems and irrigated agricultural lands in a semiarid region using the Noah land surface model (LSM) in combination with the Weather Research and Forecasting (WRF) Model. This study was conducted in the semiarid Snake River plains of south central Idaho comprising of both natural vegetation and agricultural lands. This area is characterized by warm, dry summers with irrigation being the main moisture source during the growing season. In order to properly represent the conditions of agricultural lands and also to investigate the effects of irrigation on land-surface processes, an irrigation algorithm was introduced into the existing LSM.

Land-atmosphere feedbacks of natural vegetation were investigated through the complementary relationship between the actual evapotranspiration (ET) and the potential evapotranspiration. Results from a coupled version of the LSM enabled this research to study the effects of land surface on near-surface atmospheric properties, potential air temperature, and specific humidity.

The results from this study proved the importance of including irrigation in LSMs over agricultural lands in semiarid regions. Irrigation changed the surface energy budget partitioning by increasing latent heat flux and reducing sensible heat flux. Vegetation has a greater role in partitioning the surface energy balance components. Surface cooling effects were observed through irrigation. There was a complementary behavior between

LSM-simulated actual ET and potential ET computed from the North American Regional Reanalysis (NARR) data in natural vegetation during the moisture limiting periods. It was found that the sensible heat has been underestimated for croplands by the uncoupled LSM when verified against the control runs from WRF. The impact of coupling on natural vegetation was low compared to croplands and forests showing that, in croplands and forests, feedback effects of land surface to the atmosphere were more important. Land surface has significant influences on the lower atmosphere and the evolution of the planetary boundary layer.

TABLE OF CONTENTS

LIST OF TABLES

LIST OF FIGURES

LIST OF ABBREVIATIONS

AA	Advection Aridity (model)
AVHRR	Advanced Very High Resolution Radiometer
C_h	Surface exchange coefficient for heat
CR	Complementary Relationship
CRAE	Complementary Relationship Areal Evaporation, a model
C_{zil}	An empirical coefficient (also known as Zilitinkevich coefficient)
DTR	Diurnal Temperature Range
EF	Evaporative Fraction
ET	Evapotranspiration
ET_{Noah}	Noah land surface model simulated evapotranspiration
ET_w	Wet environment evapotranspiration or equilibrium evapotranspiration
FIFE	First International Field Experiment
GCM	Global Circulation Model
GH	Ground Heat
HL	Hollister (measurement site)
HRLDAS	High Resolution Land Data Assimilation System
I	Irrigated
IDWR	Idaho Department of Water Resources
IHOP	International H_2O Experiment-2002

LAS	Large Aperture Scintillometer
LES	Large Eddy Simulation
LH	Latent Heat
LSM	Land Surface Model
METRIC	Satellite-Based Energy Balance for Mapping Evapotranspiration with Internalized Calibration
MM5	Fifth-Generation Pennsylvania State University- National Center for Atmospheric Research Mesoscale Model
MODIS	Moderate Resolution Imaging Spectroradiometer
MSM	Minimum Soil Moisture
NAM	North American Mesoscale, a model
NARR	North American Regional Reanalysis
NCAR	National Center for Atmospheric Research
NCEP	National Centers for Environmental Prediction
NI	Non-Irrigated
PBL	Planetary Boundary Layer
PET	Potential Evapotranspiration
RMSE	Root Mean Squared Error
R_n	Net Radiation
RPT	Rupert (measurement site)
RR	Raft River (measurement site)
SEBAL	Surface Energy Balance Algorithm for Land

SH	Sensible Heat
SM	Soil Moisture
ST	Skin Temperature (or land-surface temperature)
STATSGO	State Soil Geographic, soil data set
TWF	Twin Falls (measurement site)
USBR	United States Bureau of Reclamation
USDA	United States Department of Agriculture
USGS	United States Geological Survey
WPS	Weather Research and Forecasting Preprocessing System
WRF	Weather Research and Forecasting (model)

CHAPTER ONE: INTRODUCTION

This research seeks to address the inadequacy of understanding the land-surface

processes related to the interaction of surface fluxes and vegetation between irrigated and

non-irrigated areas of both natural ecosystem and agricultural landscapes in a semiarid

region. The study area of this research is in the semiarid Snake River Basin. This research

focused on investigating the effects of irrigation by incorporating an irrigation scheme to

the existing Noah Land Surface Model (LSM; Chen et al., 1996) in order to better

represent and characterize the surface energy balance over the agricultural and natural

ecosystems. Generally, LSMs resolve surface energy and water fluxes when provided

with the meteorological conditions. The main outputs from LSMs include surface energy

and water balance components. Impacts of the coupling of land and the atmosphere on

surface fluxes were evaluated by comparing the uncoupled model results with a coupled

version. Feedbacks from the land surface into the atmosphere were analyzed using the

near atmospheric properties of potential temperature and specific humidity. These

feedbacks are important in simulating the regional climate. In a data-limited region such

as the Snake River basin, this study additionally evaluated evapotranspiration using the

complementary relationship from both shrublands and grasslands.

Noah LSM is a commonly used model in both the research and weather

forecasting community. The uncoupled model simulations from Noah LSM have been

verified with field observations from different campaigns such as the First International

Field Experiment (FIFE; Chen et al., 1996), the Southern Great Plains 97 Experiment (Sridhar et al., 2002), the Cooperative Atmospheric Surface Exchange Study 97 Experiment (Chen et al., 2003), the International H_2O Experiment-2002 (IHOP-2002; LeMone et al., 2008; Rosero et al., 2009) and the Grasslands Destabilization Experiment in the Sand Hills of Nebraska (Radell and Rowe, 2008). Some of these studies have shown that it is ideal for arid and semiarid regions. Hence, this study focuses on using Noah LSM to model the land-surface processes with required changes to realistically represent the study region in the model.

South Central Idaho is a semiarid region characterized by low annual precipitation. Average annual precipitation ranges from 200 to 250 mm and the mean annual air temperature range is 5 °C- 10.9 °C, July being the warmest month with the highest evaporation (Kjelstrom, 1995). Extensive agricultural activities take place during the growing season, which heavily depend on irrigation supplied from both surface and ground-water resources due to the inadequacy of precipitation water in the plain. The Snake River is the main source of surface-water supply for irrigation. Figure 1.1 shows the agricultural lands in Idaho with a land area of approximately 13,468 km^2 and 91% of this land area is situated in the Snake River basin. The irrigated areas surrounded by dry, natural vegetation create an ideal location to study the land-surface interaction through advection between irrigated and non-irrigated regions. This area is important in this kind of study for various reasons. The addition of water to the system through irrigation changes the land-atmospheric interactions by affecting the energy and water budgets, by partitioning most of the energy into latent heat, and reducing sensible heat, thus

increasing evapotranspiration (ET). Therefore, irrigation is a key process during the

growing season. Due to the cooling effects induced by irrigation over the irrigated lands,

it creates a platform for advection from the surrounding dry, natural vegetation. However,

Noah LSM currently does not account for irrigation. In order to fulfill this requirement,

an irrigation scheme was added to the existing model code.
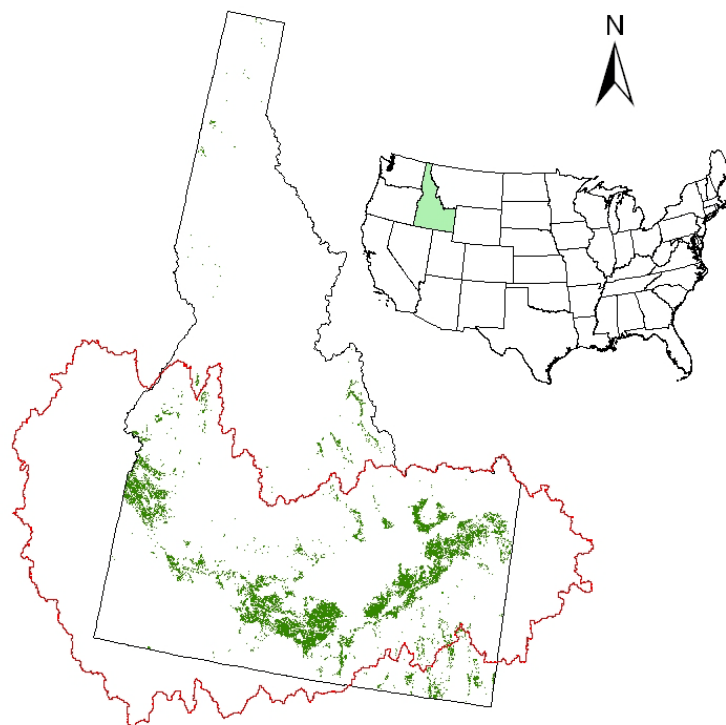
Figure 1.1. Agricultural Lands in Idaho (Shown by the Green Color; Pervez et al., 2008). The Snake River Basin Is Shown in Red Line

1.1 Background

As stated before, in semiarid regions like the Snake River Plain, ET plays a main

role in the energy and water budget. Therefore, accurate quantification of ET improves

the quality of energy and water balance studies. Influence of vegetation on surface fluxes

is identified as a factor that affects the regional climate (Pielke, 2001). Unfortunately, the unavailability of surface fluxes and ET records from this area hinders the opportunity of research related to ET and surface fluxes. These reasons hindered our understanding of the land-surface dynamics, which also motivated this research. Since field measurements were not available, an LSM was used to simulate ET and surface fluxes. Interaction between different land-cover types and their influence on surface fluxes were analyzed using LSM-simulated ET and surface fluxes.

Noah LSM has been widely used in many studies and has undergone improvements in terms physical parameterizations consistently over the last two decades in terms of physical parameterizations. Ek et al. (2003) showed the importance of upgrading the snowpack and adding frozen soil physics to the Noah LSM by comparing the results with observations at several study sites. The performance of Noah LSM was validated with the surface-flux measurements in Oklahoma by Sridhar et al. (2002), which showed reasonably good correlations with low bias and error. Chen et al. (2003) compared modeled surface flux maps with both surface and aircraft measurements. Their results indicated that the model was able to capture the surface heterogeneity. Radell and Rowe (2008) analyzed the influence of subsurface water on the surface fluxes using the Noah LSM and the observations in the Nebraska Sand Hills. Their results revealed that the Noah LSM performed well for the dry sites where the water table had negligible influence on the root zone. Chen et al. (2007) developed the High Resolution Land Data Assimilation System (HRLDAS), which runs the Noah LSM in an uncoupled fashion. This new platform enabled the application of gridded weather data available in the field.

They showed that HRLDAS simulations of soil moisture, temperature, and surface-heat

fluxes agreed well with Oklahoma Mesonet and IHOP-2002 field data.

Model results largely depend on the accuracy of the parameters. Most parameters

have been derived for specific regions and therefore using area specific values for other

regions does not always yield good results (Hogue et al., 2005). Further, the parameter

transferability depends more on climate than the similarity in vegetation and soil texture

(Rosero et al., 2010). Godfrey and Stensrud (2010) observed large errors with the existing

model forecasts. They developed a new empirical parameterization for latent heat flux

computation from principal-component regression using the measurements from

Oklahoma Mesonet. The empirical relationship for latent heat flux with an empirical

canopy transpiration scheme improved the prediction of latent and sensible heat and

energy partitioning in the LSM. Many studies (Chen et al., 2010; Hogue et at., 2005;

LeMone et al., 2008) have shown that Noah LSM tends to overestimate sensible heat flux

with the existing parameters. Chen and Zhang (2009) proposed a new parameterization

for the surface-exchange coefficient calculations, which improved the sensible heat flux

predictions in Noah LSM. This new parameterization was incorporated into the existing

Noah LSM in this study.

Usually, LSMs have the ability to be run in both coupled and uncoupled modes.

In the uncoupled mode, externally provided atmospheric variables drive land-surface

processes, and in the coupled mode the LSM is dynamically linked with an atmospheric

model, which allows feedbacks between the land surface and the atmosphere to be

modeled. Chen and Dudhia (2001a) coupled the fifth-generation Pennsylvania State

University National Center for Atmospheric Research Mesoscale Model (MM5; Grell et al., 1994) with Noah LSM (Chen et al., 1996) and validated it with FIFE observations (Chen and Dudhia, 2001b). Miao et al. (2007) coupled Noah LSM and Pleim-Xiu LSM (Xiu and Pleim, 2001) with MM5 and studied the spatial and temporal variations of near-surface air temperature. Coupled MM5-Noah was used to investigate the hydrological effects of irrigation in Syria and Turkey (Evans and Zaitchik, 2008). Huang and Margulis (2010) coupled Noah LSM with LES (Large Eddy Simulation). Their results showed that the coupled model reproduced area average fluxes and domain averaged vertical profiles of potential temperature and specific humidity well compared with observations. The WRF (Weather Research and Forecasting Model; Skamarock et al., 2005) is a coupled version of Noah LSM usually considered to be a state-of-the-art, next-generation model.

Noah LSM is the land-surface scheme, out of four currently available algorithms, to resolve the land-surface processes in WRF. In WRF, the feedbacks from the land surface are dynamically connected with the atmosphere, while Noah LSM does not provide feedbacks to the atmosphere in the uncoupled mode. WRF results from a parallel project at Boise State University were compared with the Noah LSM output to assess the effects of coupling on the surface processes. Both models used the same external meteorological data in this study. WRF model runs are computationally demanding and time consuming. This comparison enabled the researchers to decide if less demanding Noah LSM is capable of capturing the dynamics of land-surface processes, depending on the requirements.

1.2 Evapotranspiration

ET is the water flux leaving the land surface as the combination of evaporation and transpiration. Most of the precipitation that comes to the land is returned to the atmosphere through ET. It links the surface energy balance and the water balance, as ET is the common term in both cases. Therefore, ET is important in both water balance and energy balance studies. Considering its role in many processes, accurate estimation of ET is very important for applications like water resources management and planning, irrigation planning, and understanding climate change and land-atmosphere feedbacks.

ET varies over space and time depending on the vegetation, precipitation, soil properties, and anthropogenic effects. Irrigation is a main anthropogenic effect in agricultural areas that change both the water and energy budget, especially in semiarid regions. Many modeling and observational studies have shown its effects not only on ET, but also on atmospheric variables. It provides enough supply of water for ET. Observational studies have shown an increased in ET with irrigation (Lei and Yang, 2010; Suyker and Verma, 2009). Some observational studies have shown the effects of irrigation on lower atmospheric properties and cloud formation (Adegoke et al., 2007). Irrigation has been incorporated with many modeling studies and the results show effects on water and energy balance (Evans and Zaitchik, 2008; Ozdogan et al., 2010; Adegoke et al., 2003; Haddeland et al., 2006), and irrigation-induced surface cooling (Cook et al., 2010).

ET can be measured in the field by the eddy covariance method, weighing lysimeter, Bowen ratio method, and scintillometers. Other than the difficulties related and

expensiveness of instrumentation, these methods are often limited to point-scale measurements or small areas (few square kilometers). Due to the highly variable nature of ET, making estimates for regional scales using point measurements can be inaccurate. Therefore, there are several empirical and analytical methods commonly used in the field to arrive at best estimates of ET, primarily using numerical models. The computation of ET in these models is based on theories and equations that have been derived, such as the water balance and energy balance methods (Rana and Katerji, 2000). In water balance studies, ET is often computed as the difference between precipitation and runoff (Walter et al., 2004). LSMs and satellite-based models (Allen et al., 2007a; Allen et al, 2007b; Tang et al., 2009; Tang et al., 2010; Alfieri at al., 2009) are widely used to model ET. Another approach, which has been used in the field to compute ET with minimal meteorological data, is the complementary relationship (CR) approach. This is based on the feedback mechanism between actual ET and potential ET (Bouchet, 1963).

Satellite-based models have the ability to model ET for a regional area. Allen et al. (2007a) developed METRIC (Satellite-Based Energy Balance for Mapping Evapotranspiration with Internalized Calibration), which is based on SEBAL (Surface Energy Balance Algorithm for Land; Bastiaanssen et al., 1998) to map ET using remotely sensed images. The theory in the model is surface energy balance, and ET is calculated as the residual of the energy balance equation. Results from a method known as VI-T_s (Nishida et al., 2003; Tang et al., 2009), which uses the vegetation index and surface temperature to calculate ET, showed that it is more suitable to be used in irrigated areas. These methods are less expensive than field measurements. However, these remote

sensing-based methods are limited by temporal resolution of the remotely sensed data/images. Most of the time, these methods use evaporative fraction to get monthly or seasonal ET from the instantaneous ET. Some uncertainties can be related to these assumptions of temporal aggregation. Therefore, simulating the surface processes using LSM was preferred in this study.

1.3 Complementary Relationship

The complementary relationship (CR) approach was first identified by Bouchet (1963) based entirely on heuristic arguments. It is based on the feedback mechanism between the actual ET and potential ET. It is a relatively simple method to estimate ET using only meteorological variables. This method avoids the extremely cumbersome process of parameter calibration if the traditional ET computational methods of Penman and Priestly Taylor formulations are adopted where parameterizations are well understood. Many studies have identified the CR in many regions commonly using pan evaporation (Kahler and Brutsaert, 2006; Hobbins et al., 2001; Hobbins et al., 2004). Pan evaporation is normally used as an indication of the actual evaporation; it is usually higher than actual evaporation. Pan evaporation rates showed decreasing trends in many regions in the U.S when the precipitation showed increasing trends (Lawrimore and Peterson, 2000). Brutsaert and Parlange (1998) explained this evaporation paradox using the CR theory stating that the relationship between actual ET and pan ET is complementary but not proportional. Hobbins et al. (2004) proved the argument put forth by Brutsaert and Parlange (1998) on CR by relating pan ET and actual ET using the

trends in pan ET and actual ET for 655 basins across the conterminous U.S. They

concluded that decreasing pan ET is not an indication of decreasing actual ET, instead it

is evidence of increasing actual ET.

Three CR-based models that have been used are the advection-aridity (AA) model

(Brutsaert and Stricker, 1979), the complementary relationship areal evaporation (CRAE)

model (Morton, 1983), and the complementary relationship model (Granger and Gray,

1989). Xu and Singh (2005) showed that these models work well for regions where

climate variables are a controlling factor for ET, not soil moisture. Other than using only

observations in deriving the CR, studies have used results from numerical models.

Ozdogan et al. (2006) used a mesoscale climate model and meteorological data to

evaluate the CR between potential ET (PET) and actual ET. In addition to the CR, they

found that wind speed and stability effects are the main factors in maintaining the

complementarity. Oudin et al. (2005) applied CR in two rainfall-runoff models to

estimate ET.

Actual ET from natural vegetation solely depends on precipitation. ET is not only

affected by the vegetation properties, but also by the soil properties. In order to obtain

better results from numerical models, parameters should be properly known related to

vegetation and soil. Huntington et al. (2011) derived the complementary theory for

phreatophyte shrub species in eastern Nevada. Their results confirmed that CR is

applicable in that area to estimate ET. The study area in this research mainly comprises of

natural vegetation including grasslands and shrublands. Since CR is based on only

meteorological variables, it was tested if the CR approach can be used to estimate ET from natural vegetation in this study area.

1.4 Importance of Feedbacks and Motivation for This Study

Interactions between the land surface and the atmosphere via exchanges of heat, mass, and momentum creates a dynamically coupled system influencing the weather and climate (Pielke et al., 1998). These exchange processes are aided by atmospheric circulations that happen due to the uneven distribution of radiation on the earth surface (Shelton, 2009). There are several forms of land-atmospheric interactions that lead to different feedback processes. Many studies have been done using Global Circulation Models (GCM) to understand the influence of land-atmosphere interactions on climate. It has been found that the short-term biophysical and long-term biochemical processes have significant effects on weather and climate (Pielke et al, 1998). Raupach (1998) identified four short-term feedback pathways, namely aerodynamic coupling, physiological coupling, convective boundary-layer coupling, and radiative coupling. In all four situations, the surface energy budget plays a main role. In general, there is positive feedback between evaporation and precipitation, and also between soil moisture and precipitation. However, positive or negative feedbacks can result between soil moisture and precipitation depending on the climate region (Orlowsky and Seneviratne, 2010). Dry soil reduces precipitation, which further suppresses the soil moisture states. Formation of Sahel is an example for this latter situation, which is a result due to the high albedo from dry soil or the removal of vegetation (Charney, 1975). It has been found that seasonal

variations in vegetation phenology influence the regional climate by its control of water and energy exchange over the land surface (Lu et al., 2001). In dry and warm areas, relatively high temperature increases the evaporation demand, but dry soil moisture conditions simultaneously restrain the evaporation (Brubaker and Entekhabi, 1996). Additionally, the resulting high surface temperature causes stomatal closure (Monteith, 1975), restricting transpiration. Increased evaporation results in increased precipitation, which in turn increases soil moisture, creating a positive feedback. Some studies have identified the feedbacks between vegetation and convective precipitation (Anthes, 1984; Blyth et al., 1994). GCM studies have shown that Amazon deforestation can result in reduced precipitation due to the reduction in a moisture source (Henderson-Sellers at al. 1993; Shukla et al., 1990).

The evolution of the atmospheric boundary layer is mainly affected by the partitioning of net radiation into sensible heat flux and latent heat flux (Pielke et al., 1998). There are many land-surface conditions that affect this partitioning, such as the land-cover type and soil moisture state. High soil moisture conditions favor latent heat over sensible heat. This partitioning greatly varies with the land-cover types, varying from bare soil to forests. When vegetation is present, it consumes most of the energy and transpires water to the atmosphere, creating more latent heat flux than sensible heat flux. On the other hand, when the soil is dry, vegetation becomes water stressed and will close their stomata, restraining transpiration, in which case available energy is directed more to sensible heat flux (Avissar and Peilke, 1991). Over a vegetated surface, stomatal conductance and leaf area index variability are the main factors that affect the energy

fluxes while soil moisture is important in barren land under unstable conditions (Avissar et al., 2004).

This area of interest in the Snake River basin provides a good opportunity to investigate the above mentioned relationships between vegetation and surface energy partitioning. Irrigation in the agricultural area has the major effect of changing the whole process. It increases the soil moisture, leading to an increase in latent heat/ ET. This increased moisture source from ET changes the humidity in the near-surface atmosphere and decreases the vapor pressure deficit. This in turn alters the ET demand as identified by the complementary relationship (Bouchet, 1963). Another effect of increased ET is the enhanced precipitation recycling through moisture supply and reinforced moisture anomalies (Brubaker and Entekhabi, 1996). These different effects of land cover and variations of energy partitioning on the boundary layer development were examined using the WRF atmospheric results.

1.5 Objectives of the Study

The hypothesis in this study is that integrating human-induced changes with the land-surface processes via irrigation in the Noah land surface model is necessary for assessing regional climate feedbacks and surface energy budget partitioning. Given the amount of precipitation (less than 200 mm) in the region, the conventional models can not exactly quantify evapotranspiration unless the extra water added through irrigation is explicitly included in the computation of evapotranspiration within the model. Therefore, the objectives of this research are:

1. to improve the land-surface dynamics in Noah LSM by integrating an irrigation algorithm, which increases the availability of soil moisture during the growing season

2. to evaluate the ET, surface energy balance components, and soil moisture that is impacted by irrigation over agricultural areas

3. to derive the complementary relationship for both natural and agricultural ecosystems in order to estimate ET relatively easily during the moisture-limiting periods

4. to assess the effects of coupling and the feedback between the land surface and the atmosphere by analyzing the Noah LSM output with the results of WRF, a coupled version of Noah LSM

Noah LSM was used to simulate the land-surface processes for a study area located in Snake River Basin with both irrigated and non-irrigated lands. Noah LSM was used in the uncoupled mode to reduce the computational demand for long-term model runs to understand the regional energy-balance climatology. Model results for non-irrigated regions were validated against the recently instrumented sites at Hollister and Raft River, Idaho. In order to validate the effects of irrigation on ET, METRIC images were used in 1996, 2000, 2002, and 2006 during the growing season. Thirty-year model simulations were studied to examine the historic trends of ET, which will be a guide for future trends in ET. Finally, Noah LSM results were compared with the coupled WRF model results to see how the coupling affects the surface energy balance.

1.6 Limitations

Even though Noah LSM is widely used in the field, there are some limitations. It did not account for the water added through irrigation in agricultural regions. This study addressed that shortcoming by adding a new irrigation algorithm. As discussed before, vegetation has a great influence on the surface processes and also on the atmosphere. Different vegetations have different characteristics. In the Noah LSM, most of them are parameterized for simplicity like leaf area index, canopy resistance, and roughness lengths. However, vegetations are categorized and given the same parameters in the model. For example, all of the agricultural area with different crop types is categorized as croplands; there is only one shrubland category even though there are different types of shrubs. Vegetation parameters should be changed according to these different types. Due to the difficulty in finding the vegetation-specific parameters, the existing parameters with existing vegetation classes were used here.

Obtaining accurate, gridded weather forcing data is another difficult task in the modeling. Data collected at weather stations mostly represent the point scale or very small areal scale. Also, they are scattered and most of the time, there are not enough weather stations to represent the whole area. The North American Regional Reanalysis data set used in this study is a model-generated data set using field observations. In the absence of direct field observations, this data set was a valuable source of gridded weather data to be used in the model simulations. Yet the data comes in three hour intervals. Therefore, an interpolation procedure was required to temporally downscale it

into the model time steps. This data set is available only from 1979 to present. Due to this

limitation of data availability, historic simulations were restricted.

CHAPTER TWO: STUDY AREA

The study area is situated mainly in a semiarid region in the Snake River Basin of south central Idaho with some area extending to Utah and Nevada. It is located roughly between 41.37º N and 43.75º N, and between 112.13º W and 116.15º W. The land area is approximately 85,536 km^2, which consists of both irrigated and non-irrigated lands. All irrigated lands are located within the Snake River basin in Idaho. Figure 2.1 shows the study area with the field observing sites, which will be described below.
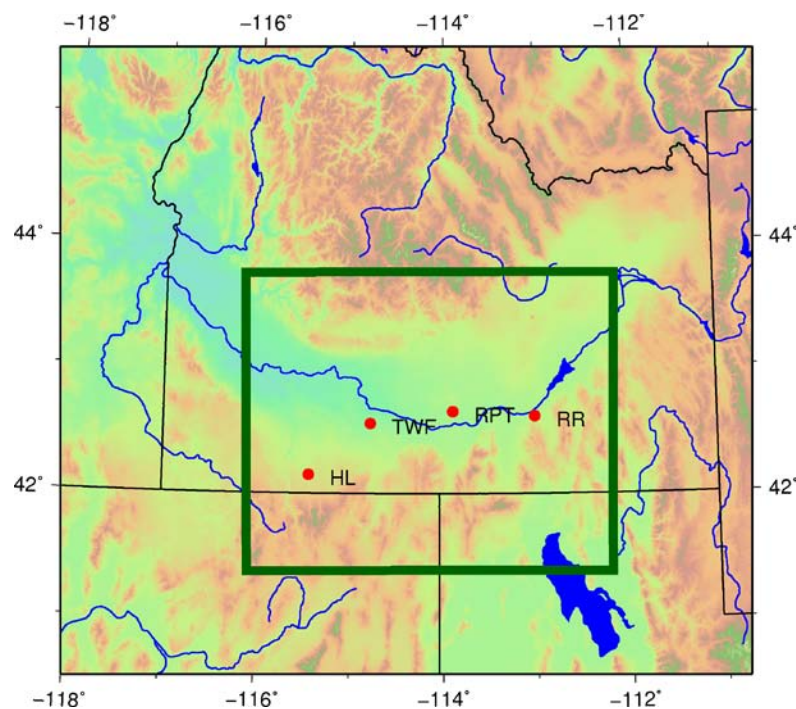
Figure 2.1. Noah LSM Domain Indicated by the Green Box. Four Measurement Sites Are Shown with Red Circles. HL - Hollister, TWF - Twin Falls, RPT - Rupert, and RR - Raft River. The Black Lines in the Figure Represent State Boundaries and Blue Lines Indicate the Rivers.

The Snake River, the largest tributary of the Columbia River, flows through the plains, an area that is heavily irrigated, in the Snake River plains. It originates in the mountainous area including the Teton Range in western Wyoming and Yellow Stone National Park. Cold winters and hot, dry summers are common in the area. While most of the precipitation during the summer is evaporated, precipitation in the winter and early spring is the main source for recharge of the ground water (Kjelstrom, 1995). Runoff from snow melt events from the mountains are the main source of water for irrigation diversions during the growing season.

According to the North American Regional Reanalysis (NARR) data set, the annual total precipitation, averaged for last 30 years, of the study area is 352 mm with total winter precipitation of about 100 mm. The maximum precipitation event has taken place in 1983. Elevation drops from 3005 m to 739 m in the whole area while the elevation range of the croplands is from 739 m to 2121 m. The mean annual temperature ranges from 7.2°C to 10.6°C for the whole domain. The mean temperature over the irrigated cropland is 8 °C – 12.5 °C.

The main land-cover types in the area are shrublands, grasslands, croplands, and forests while there is a small portion of developed land. The focus of this study is on irrigated croplands, which have great influence on the regional climate in the area through human induced activities like irrigation and land cover change. Alfalfa, potato, wheat, corn, and barley are the main crop types according to the extracted data from 2009 Idaho cropland data layer prepared by National Agricultural Statistics Service, United States Department of Agriculture (USDA; USDA, 2010).

Due to the semiarid conditions in this area, extensive irrigation takes place during the growing season in the cropland area to provide required water for the growth of crops. Sprinkler irrigation and surface irrigation are the two methods widely adopted in the area (Kenny et al., 2009). Irrigation is also a source for increased ET during the growing season. Since ET is the main phenomenon through which soil water is depleted, a correct estimation of ET is needed in planning irrigation diversions. Water managers face the challenge of planning scarce water resources.

While irrigation activities are concentrated along the Snake River, the agricultural area is surrounded by dry lands, mostly shrubland and grassland. Due to the limited soil moisture conditions in this landscape, the new moisture source from irrigation can cause increased land-atmospheric interactions. It is also a cause for change in energy budget partitioning, which in turn effects the boundary-layer development.

2.1 Field Observation Sites

There are field observation sites operating in the area to measure meteorological variables. AgriMet (AgriMet, 2011) is a network of automated agricultural weather stations that collect data required for water management. It is operated and maintained by the United States Bureau of Reclamation (USBR). Recently instrumented meteorological measuring sites have begun operating at Hollister, Raft River, and Island Park (Idaho NSF-EPSCoR, 2010) to measure the energy balance components in addition to a suite of meteorological and soil variables. The instruments used at these sites are Scintec BLS900 large aperture scintillometers for estimating sensible heat flux along 800 to 1600 m

transects, three 3-D sonic anemometers at each site for measuring sensible heat flux and

boundary-layer turbulence, and fast response hygrometers for estimating ET and CO_2

fluxes by the eddy covariance method. Each site has instruments for soil heat flux, soil

water content, soil temperature, and net radiation measurements. This instrumentation

project was sponsored by NSF Idaho EPSCoR and it was operated and maintained jointly

by Boise State University, Idaho State University, and the University of Idaho. Of the

three stations, Island Park was not instrumented until October, 2010. Therefore, no data

from that site was available to use in this study.

2.1.1 Hollister Site (HL)

There are four instrumentation sites at HL, namely, Large Aperture Scintillometer

(LAS) Transmitter, LAS Receiver, Eddy Covariance Site 1, and Eddy Covariance Site 2

(Figures 2.2 and 2.3). The transect between the transmitter and receiver sites is roughly

1.8 km running south to north. This is located approximately at 42.33 N and 114.7 W.

The dominant land-cover type of the site is sagebrush (Artemisia tridentata). It is a hardy

plant in arid climate conditions. Since this vegetation is common in shrubland in the

study area, measurements from this site provide near surface atmospheric conditions,

energy balance, and soil moisture information, which can be used in studies.

2.1.2 Raft River Site (RR)

Like HL, RR consists of four instrumentation sites, which are located around

42.58 N and 113.41 W (Figure 2.2 and 2.4). This transect here is around 1 km. This area

was used to be irrigated farmland in the past but has been converted to dry land. The

currently dominant vegetation is cheatgrass (bromus tectorum), which is an invasive

species. It is mixed with some bunch grass.
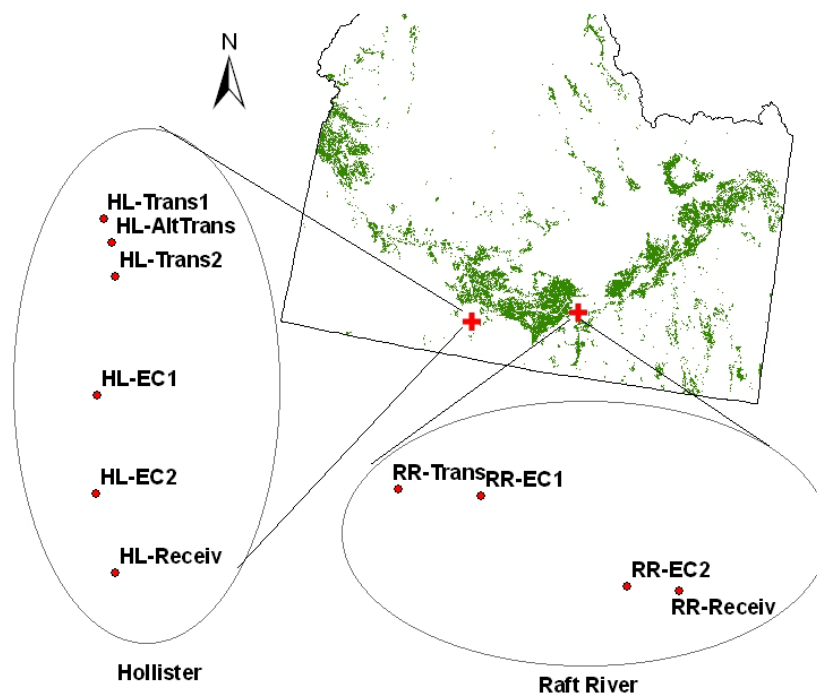
Figure 2.2. Instrumentation Locations at Hollister (HL) and Raft River (RR). The Definitions of the Names Are Trans1 - Transmitter 1 (Scintillometer), Trans2 - Transmitter 2 (Scintillometer), AltTrans - Alternate Transmitter (Scintillometer), Receiv - Receiver (Scintillometer), EC1 - Eddy Covariance Site 1, and EC2 - Eddy Covariance Site 2

2.1.3 AgriMet Weather Stations

There are several AgriMet weather stations situated in the area. Data from only

two stations were used in this study. They are Twin Falls (Lat: 42.546 N, Long: 114.345

W) and Rupert (Lat: 42.596 N, Long: 113.874 W). They are mainly located within the
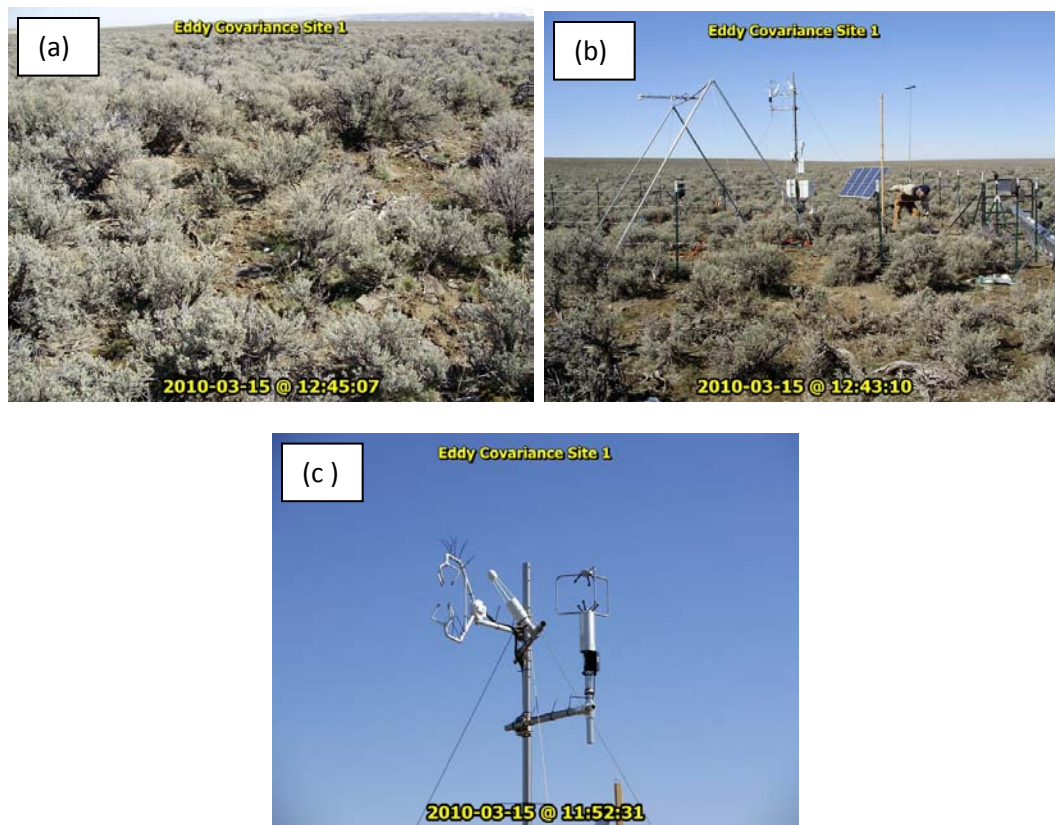
Figure 2.3. Pictures of the Instrumentation Site at Hollister: (a) Vegetation at the Site, (b) Instrumentations at Eddy Covariance Site 1, (c) Instrumentation for Eddy Covariance.
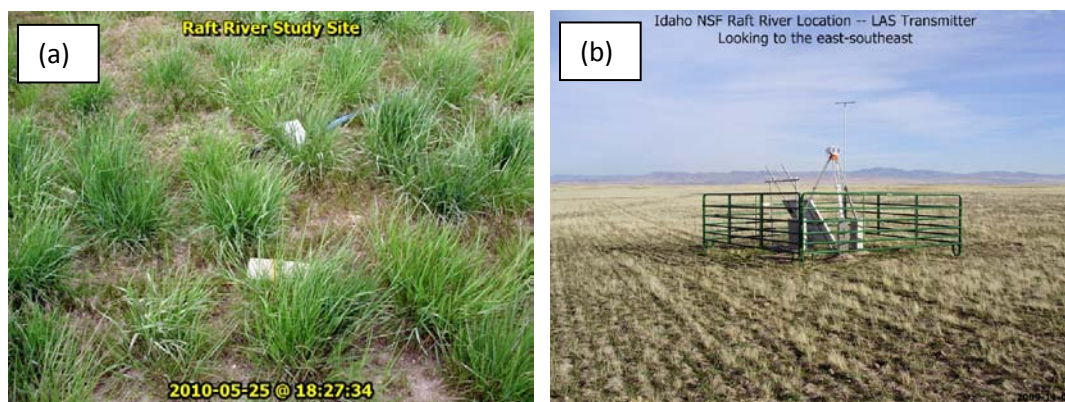
Figure 2.4. Pictures of the Instrumentation Site at Raft River: (a) Vegetation in May, (b) Large Aperture Scintillometer Transmitter.

agricultural fields to measure meteorological variables to compute evapotranspiration for

crop-water management purposes. Most of the records go back to 1990's period.

Observations are available both in daily and hourly time intervals.

CHAPTER THREE: METHODS

3.1 Noah LSM

The Noah LSM model is a widely recognized and evolving land-surface

algorithm to compute energy and water balance components, which originated by Pan

and Mahrt (1987), and has been constantly subjected to many improvements. Some of

them are modifications in the canopy-resistance formulation (Chen et al., 1996), bare soil

evaporation and vegetation phenology (Betts et al., 1997), surface runoff infiltration

(Schaake et al., 1996) and thermal roughness length treatment in the surface-layer

exchange coefficients (Chen et al., 1997), and the addition of frozen soil physics (Koren

et al., 1999). With continued advances, it is operationally used in many research studies,

weather prediction, data assimilation, etc., with spatial scale ranging from meters to

kilometers. It has the ability to be executed as both a coupled and uncoupled mode to

simulate the land-surface hydrology. In the uncoupled mode, atmospheric variables are

forced in models, while in the coupled mode, atmospheric input variables are

dynamically coupled with the atmospheric module. Some of the weather-prediction

models that Noah has been coupled to are the North American Mesoscale (NAM) model,

the fifth-generation Pennsylvania State University National Center for Atmospheric

Research (PSU-NCAR) Mesoscale Model (MM5; Chen and Dudhia, 2001b), and the

Weather Research and Forecasting model (WRF; Skamarock et al., 2005).

The Noah LSM has four soil layers, one canopy layer, and one snow layer. The depths of the soil layers from the surface are 10cm, 40 cm, 100cm, and 200cm. The total depth of the soil column is 2 m. Except for the forest vegetation type, the root zone lies within the first three layers (i.e., within top 1m of soil). The number of root zone layers is dependent on the vegetation type.   Water movement through the soil column is limited only in the vertical direction and there is no horizontal interaction between the neighboring grid cells. The lower 1 m of the soil column acts as a reservoir and drains the water out from the soil column at the bottom, which happens only due to gravity (Chen and Dudhia, 2001a). A schematic diagram of Noah LSM is shown in Figure 3.1.
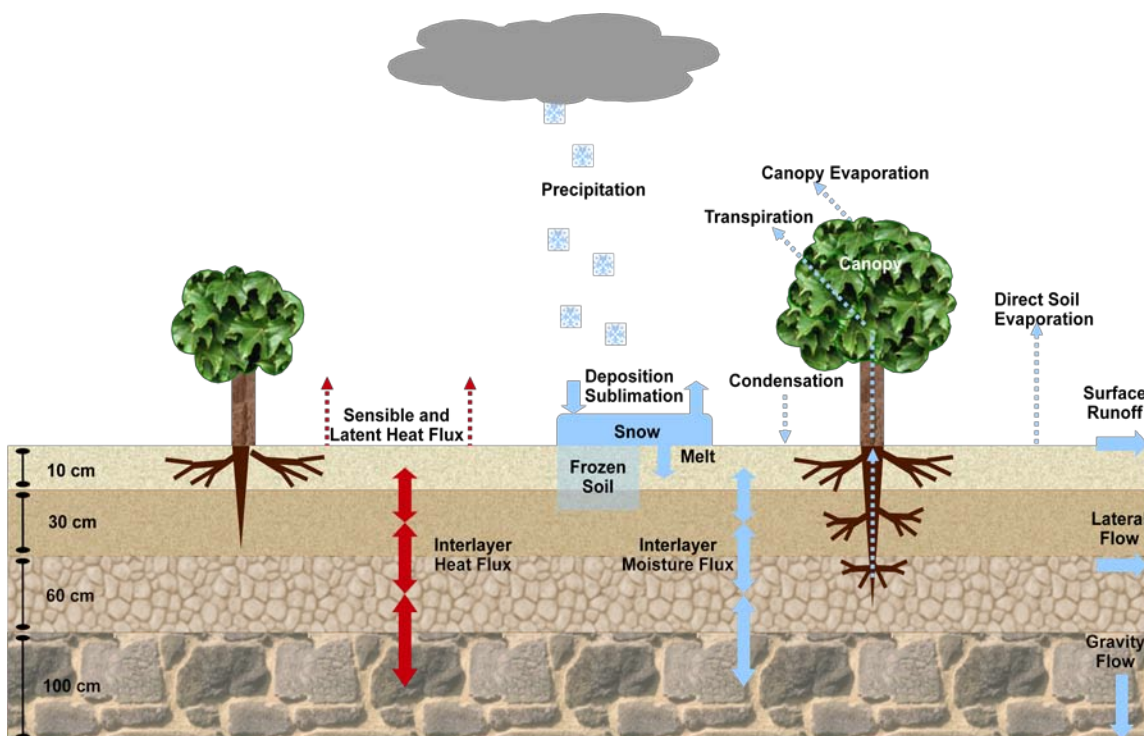
Figure 3.1. The Schematic Diagram of the Noah LSM

Many processes in Noah LSM are parameterized in order to simplify the computations. Vegetation type and soil texture are the two main inputs that determine most of the parameters. There are 10 vegetation parameters (Appendix A) and 10 soil parameters (Appendix B). They are read from the look-up tables when the model is run. Two options are available to select the vegetation classification from USGS (U.S. Geological Survey) and MODIS (Moderate Resolution Imaging Spectroradiometer). The USGS classification has 24 vegetation categories while MODIS- based classification consists of 19 categories. In addition to soil and vegetation-dependent parameters, there are some general parameters that are also read from the look-up table (Appendix C).

Model output includes surface fluxes, water budget components, soil moisture, and soil temperature. Generally, Noah LSM is run in hourly time steps, although it can be run in finer temporal resolution such as 30 minutes. The time step of at least one hour is required to track the movement of water in the surface layer and also to capture the land-atmospheric interactions through exchanges of heat and momentum.

3.1.1 Noah LSM Physics

3.1.1.1 Noah LSM Thermodynamics

Skin temperature, ground heat flux, and soil-layer temperatures are computed by the thermodynamics module within the model. Surface skin temperature (T_1) is calculated by applying the surface energy balance equation following Mahrt and Ek (1984). The fully implicit Crank-Nicholson scheme is used to predict the soil temperature at each layer with the skin temperature and the lower boundary temperature, which is assumed to

be 3 m below the surface. The lower boundary temperature of the soil column is taken as

the mean annual air temperature (Chen et al., 1996). Soil temperature (T) at i^{th} layer is

determined by

$$\Delta z_i C_i \frac{\partial T_i}{\partial t} = \left(K_T \frac{\partial T}{\partial z}\right)_{z_{i+1}} - \left(K_T \frac{\partial T}{\partial z}\right)_{z_i} \qquad (3.1)$$

where t and z are time (s) and vertical depth (m) from the soil surface. Both C

(volumetric heat capacity, $J\ m^{-3}\ K^{-1}$) and K_T (thermal conductivity, $W\ m^{-1}\ K^{-1}$) are

functions of soil water content (θ). The upper boundary condition of the model is

considered as the ground heat flux (GH, $W\ m^{-2}$), which is calculated by

$$GH = K_T(\theta)\left(\frac{\partial T}{\partial z}\right)_{z=0} \qquad (3.2)$$

3.1.1.2 Noah LSM Hydrology

In order to find the volumetric soil water content of each soil layer, the diffusive

form of Richard's equation, derived from Darcy's law, is used. Darcy's law is based on

the assumption of a rigid, isotropic, homogeneous, one-dimensional vertical flow. The

water flows only in vertical directions in the model. Volumetric soil moisture content (θ)

is given by

$$\frac{\partial \theta}{\partial t} = \frac{\partial}{\partial z}\left(D \frac{\partial \theta}{\partial z}\right) + \frac{\partial K}{\partial z} + F_\theta \qquad (3.3)$$

where D is the soil water diffusivity (m^2 s^{-1}), K is the hydraulic conductivity (m s^{-1}), and

F_θ is source and sink for soil water. Both D and K are functions of θ, which are

determined by

$$D = K(\theta)\left[\frac{\partial \psi}{\partial \theta}\right] \tag{3.4}$$

$$K(\theta) = K_s(\theta/\theta_s)^{2b+c} \tag{3.5}$$

where

$$\psi(\theta) = \psi_s/(\theta/\theta_s)^b \tag{3.6}$$

Ψ is the soil water tension function while K_s, Ψ_s, and θ_s are the conditions at saturation.

K_s, Ψ_s, θ_s, and b are read from the soil parameter table and are functions of the soil type.

Equation (3.3) is applied over each soil layer to obtain θ for each soil layer.

$$d_{z1}\frac{\partial \theta_1}{\partial t} = -D\left(\frac{\partial \theta}{\partial z}\right)_{z1} - K_{z1} + P_d - R - E_{dir} - E_{t1} \tag{3.7}$$

$$d_{z2}\frac{\partial \theta_2}{\partial t} = D\left(\frac{\partial \theta}{\partial z}\right)_{z1} - D\left(\frac{\partial \theta}{\partial z}\right)_{z2} + K_{z1} - K_{z2} - E_{t2} \tag{3.8}$$

$$d_{z3} \frac{\partial \theta_3}{\partial t} = D \left(\frac{\partial \theta}{\partial z} \right)_{z2} - D \left(\frac{\partial \theta}{\partial z} \right)_{z3} + K_{z2} - K_{z3} - E_{t3} \tag{3.9}$$

$$d_{z4} \frac{\partial \theta_3}{\partial t} = D \left(\frac{\partial \theta}{\partial z} \right)_{z3} + K_{z3} - K_{z4} \tag{3.10}$$

Equation (3.7) is applied to the top soil layer and Equations (3.8) and (3.9) are over the second and third soil layers when vegetation has three root zone layers. If the third soil layer is not classified as a root zone layer based on the vegetation type over the surface, then the last term in Equation (3.9), which is E_{t3}, should be eliminated. On the other hand, if any vegetation has four root zone layers, then a new term, E_{t4}, should be subtracted from Equation (3.10), which is applied over the bottom soil layer. In the above equations, d_{zi} is the soil layer thickness of the ith layer, P_d is the precipitation not intercepted by the canopy, and R is the surface runoff. E_{dir} and E_t are direct evaporation and transpiration, respectively. Hydraulic diffusivity of the bottom soil layer is assumed as zero. Water flow from the bottom layer happens only due to the gravitational percolation term K_{z4} (Chen and Dudhia, 2001a). Noah LSM calculates another runoff term as the numerical truncation when the water inflow of a soil layer is more than its porosity. This situation arises since there is no horizontal connection between grid cells for lateral flow to take place. Noah LSM adds the two runoff terms, the gravitational flow from the bottom layer and the runoff calculated as the numerical truncation, and outputs it as the underground runoff. This term includes both the lateral flow that can happen and

the recharge of ground water. The two-layer simple water balance model approach developed by Schaake et al. (1996) is used to calculate R. It consists of two layer or two reservoirs.

Noah LSM obtains the total evapotranspiration (ET) as the sum of E_{dir}, E_t, and E_c (canopy evaporation). The soil moisture condition of the first soil layer is a controlling factor for ET. It can proceed at the maximum or potential rate (PET) if the first soil layer is sufficiently wet. Otherwise, it can proceed only at a rate by which the soil layer can diffuse water. E_{dir} is given by

$$E_{dir} = (1 - \sigma_f) \, MIN \left(\left[D \left(\frac{\partial \theta}{\partial z} \right)_{z1} - K_{z1} \right], PET \right) \qquad (3.11)$$

where σ_f is the plant shading factor or green vegetation fraction (dimensionless). Evaporation of the precipitation intercepted water by the canopy layer is given by E_c as

$$E_c = \sigma_f E_p \left(\frac{W_c}{S} \right)^n \qquad (3.12)$$

$$\frac{\partial W_c}{\partial t} = \sigma_f P - D - E_c \qquad (3.13)$$

where W_c the is canopy water content intercepted by the plants (m), S is the maximum intercepted canopy water capacity (m), and P is the precipitation. W_c is increased by

precipitation at first for a while and then it is reduced by the evaporation. Both S and n

factor (dimensionless) are read from the vegetation parameter table and the values are 0.5

mm and 0.5, respectively. When W_c exceeds S, the excess water drips to the ground (D,

m). Transpiration occurs from canopy and roots as

$$E_t = \sigma_f E_p B_c \left[1 - \left(\frac{W_c}{S} \right)^n \right] \qquad (3.14)$$

The factor $(W_c/S)^n$ is used to reduce transpiration during a precipitation event

when the canopy surface becomes increasingly wet and canopy evaporation takes place.

B_c is incorporated with the plant resistance to transpiration, including soil moisture stress.

Transpiration depreciates soil moisture in root zone layers to limiting points known as

reference soil moisture (θ_{ref}) and wilting point (θ_{wilt}). When soil moisture reaches θ_{ref},

transpiration begins to decrease. At θ_{wilt}, transpiration stops (Mahrt and Pan, 1984). The

vegetation parameter table provides the values for θ_{ref} and θ_{wilt} for each vegetation type.

The existing form of B_c follows Ek and Mahrt (1991), which represents the effects from

solar radiation, the vapor pressure deficit, air temperature, and soil moisture stress.

3.1.1.3 Noah LSM Energy Balance

The energy balance in the model is the net radiation (R_n) partitioned into latent

(LH), sensible (SH), and ground heat (GH) flux as follows.

$$R_n = LH + SH + GH \tag{3.15}$$

Each component on the right-hand side of the Equation (3.15) is determined using physically-based formulations (Sridhar et al., 2003). LH is calculated as the energy required for total ET obtained as the sum of direct evaporation, transpiration, and canopy evaporation, while GH is determined with Equation (3.2). Sensible heat flux is derived from the bulk transfer approach given by

$$SH = \rho \, c_p C_h |U| (PT_s - PT_a) \tag{3.16}$$

where ρ is air density, c_p is specific heat of air (J kg^{-1} K^{-1}), C_h is heat transfer coefficient, U is the wind speed (m s^{-1}) at a certain height above the ground, PT_s is the potential temperature of the surface (K), and PT_a is potential air temperature (K). The importance of C_h in the model is described in Section 3.1.2.3. Net radiation (R_n) is computed by the Equation (3.17) as

$$R_n = (1 - \alpha) \, S \downarrow + L \downarrow - Emissivity \times \sigma T_s^4 \tag{3.17}$$

where S is shortwave solar radiation (W m^{-2}), L is longwave radiation (W m^{-2}), α is surface albedo, which is a function of surface characteristics, σ is the Stefan-Boltzmann constant (5.6696 x 10^{-8} W m^{-2} K^{-4}), and T_s is the skin temperature (K). Emissivity has a value between 0 – 1. S and L are model forcing variables.

3.1.1.4 HRLDAS Platform

The High Resolution Data Assimilation System (HRLDAS) runs Noah LSM in an uncoupled mode, which was developed to address the issues arising in initializing soil moisture and temperature (Chen et al., 2007). It has been developed to mesh with WRF. HRLDAS differs from WRF in a way that there are no feedbacks from Noah LSM to the atmospheric forcing conditions. A schematic of HRLDAS is shown in Figure 3.2. HRLDAS v3.1 was used here with some changes as explained in Section 3.1.2.

The process starts with acquiring data from an external source. A computer program that comes along with HRLDAS is used to organize the acquired raw data in a suitable way to be used in later stages. Grid configurations of the model and obtaining of parametric fields, like soil categories, land-use categories, and green vegetation fraction, are done by using the WRF Preprocessing System (WPS). Then, the data is extracted to the model domain defined by the WPS and required spatial and temporal interpolations are carried out using the output from WPS and the organized data. The output from the previous step as well as the output of WPS is used to run the Noah LSM in uncoupled mode.

3.1.2 Modifications

3.1.2.1 Changes in HRLDAS and Noah LSM

Instead of using the program called 'gribextract' that comes with HRLDAS in order to organize the raw data, a new program was used in this study called 'wgrib.' It is an operational NCEP (National Centers for Environmental Predictions) program written
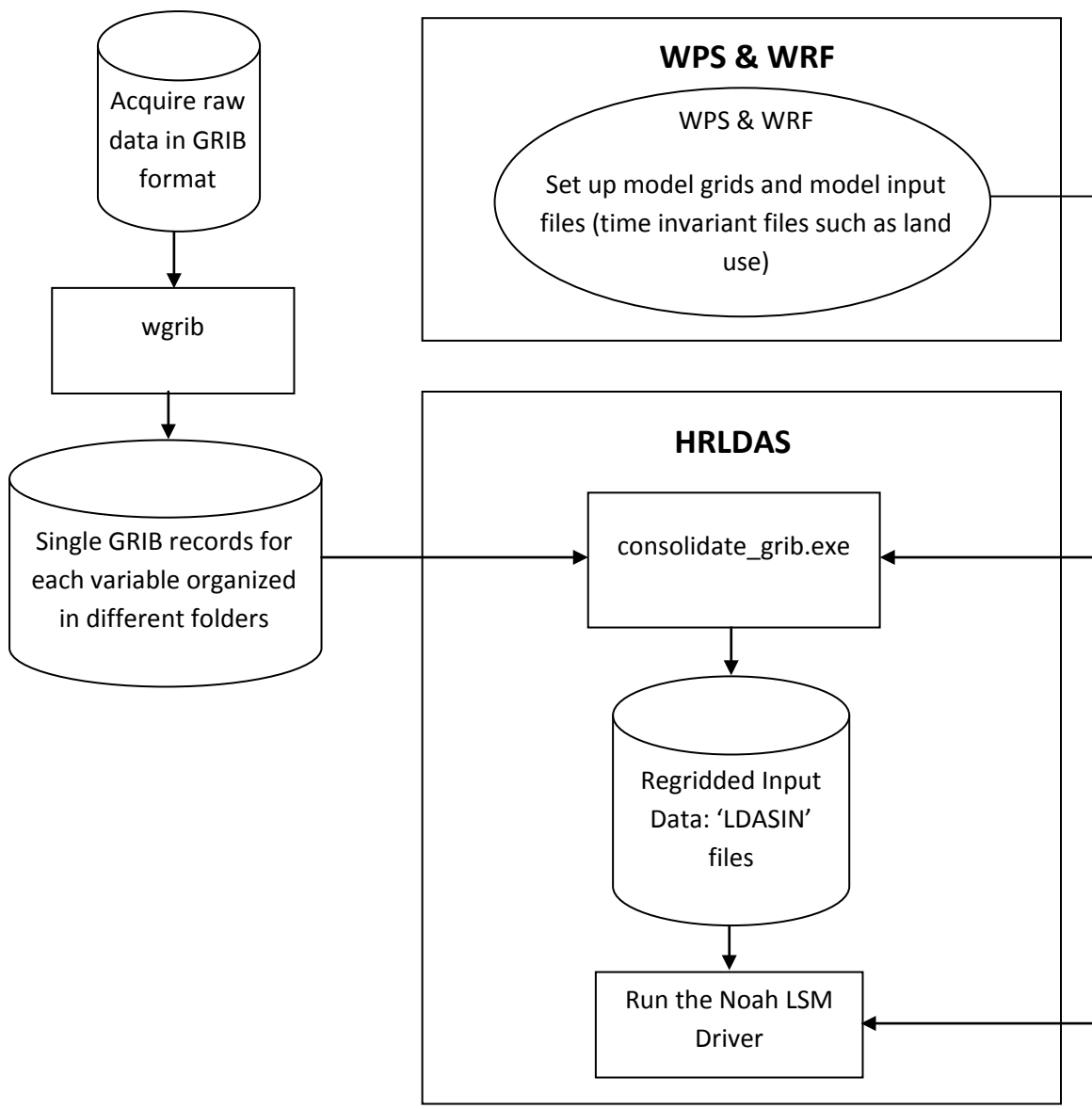
Figure 3.2. Flow Diagram of HRLDAS Platform

to read and manipulate GRIB (GRIdded Binary) files that are created by the

NCEP/NCAR Reanalysis Project (NCEP, 2010).

In order to be compatible with WRF v3.2.1 results (explained later), the Noah

LSM that comes with HRLDAS v3.1 was changed according to the Noah LSM v3.2 in

WRF. That way, all the land-surface physics were made the same for all the simulations.

New formulations of surface-exchange processes, which are already in WRF, were

included in the driver program, which is explained in Section 3.1.2.3. All the other

programs that come with HRLDAS were utilized in the study.

3.1.2.2 Irrigation Scheme

In a semiarid region like the study area here, the main input of water in an

agricultural area is received via irrigation. Many studies have identified the importance of

irrigation through different processes (Ozdogan et al., 2010; Adegoke et al., 2003; Lei

and Yang, 2010; Tang et al., 2007; Haddeland et al., 2006; Mahmood and Hubbard,

2002; Cook et al., 2010). Even with constant improvements, current Noah LSM does not

account for irrigation in agricultural areas. Since irrigation is the main anthropogenic

activity in the area and the main focus of the study is on irrigated cropland, an irrigation

scheme was added to the existing Noah LSM to maintain the soil moisture during the

growing season. Figure 3.3 shows the flow diagram of Noah LSM processes with

irrigation.

Since the choice of irrigation method (flood or surface irrigation), frequency of

irrigation, and the amount of water applied in one irrigation event depends on the

irrigation practice of each farmer, a common method was applied for all the fields in the

area considering only the water need of the soil instead of applying water at the same

frequency. Only the cells classified as irrigated cropland in the land-use categories were

subjected for irrigation in the model. There are three adjustable parameters: 1) minimum
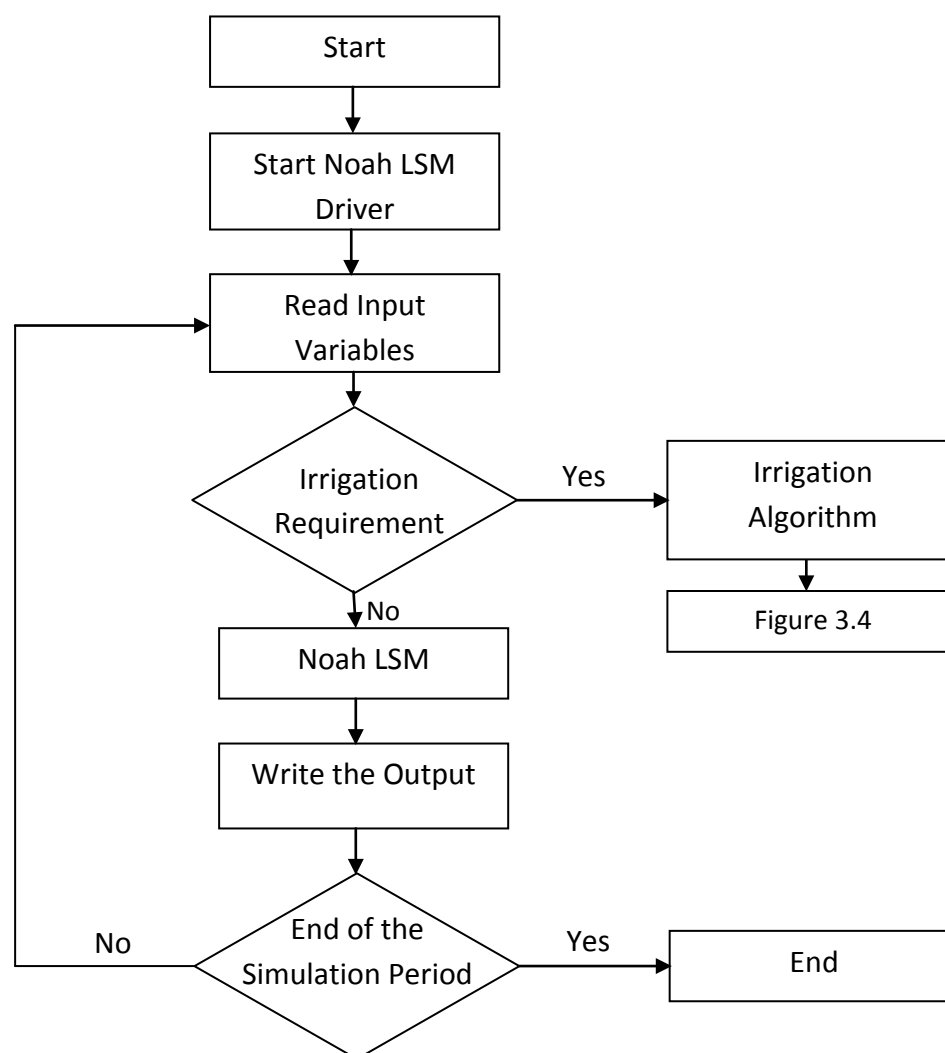
Figure 3.3. Flow Diagram of Noah LSM Processes with Irrigation

percentage of soil moisture (MinPCT), which serves as an irrigation trigger, 2) the start

date of the irrigation season, and 3) the end date. The available soil moisture of the

second soil layer (10 – 40 cm) was used to trigger irrigation. The second layer's soil

moisture was compared with minimum soil moisture (MSM) to determine if irrigation is

required. This is because the thin first soil layer of 10 cm is subjected to direct

evaporation and will be dried soon. Figure 3.4 is the flow chart of irrigation. MSM is

defined by

$$MSM = \left(\theta_{ref} - \theta_{wilt}\right) \times MinPCT + \theta_{wilt} \qquad (3.18)$$

where θ_{ref} and θ_{wilt} have the same meanings as in Section 3.1.1.2. The period from April

1st through October 31st were chosen as the irrigation season based on the information

available from a main canal company in the region, which provides water to this area

(Twin Falls Canal Company, 2011).

Firstly, it was decided if a simulation date is within the irrigation season and if the

grid is classified as an irrigated cropland. Then, the available soil moisture was compared

with MSM to decide if the irrigation is required at this time step. If the available soil

moisture is below MSM, the soil moisture of the first soil layer was saturated at this time

step as done by Adegoke et al. (2003) and Evans and Zaitchik (2008) even though there

are other differences between the methods. The minimum percentage (MinPCT) used in

this study is 50%, which is a recommended threshold limit for many crops as the

depletion level at which to start irrigation. Saturating the top layer would allow water to

flow to the soil layers below. The water loss from runoff and losses during irrigation

were not accounted here and it was assumed that enough water is available for fulfilling

the irrigation requirement in the model.

Start: per cell per timestep

Land Use classification as 'Irrigated'
And
Start Date of Irrigation≤ Day of the Year≤ End Date of Irrigation

No

Cannot Irrigate the Cell

Yes

Can Irrigate the Cell

Available Soil Moisture ≤
(Field Capacity – Wilting Point) * Minimum Percentage + Wilting Point

No

Should not Irrigate this Time

Yes

Should Irrigate this Time

Soil Moisture = Saturated Soil Moisture

Figure 3.4. Flow Diagram of the Irrigation Scheme

3.1.2.3 Surface Exchange Coefficients

Land surface and atmospheric processes are interconnected with each other

through exchanges of heat, mass, and momentum. Surface-exchange coefficients of heat

and mass, C_h and C_e, play a major role in coupling the two systems in LSMs. In LSMs,

these exchange coefficients are related with SH and LH. These are the fluxes that cause

the evolution of the atmospheric boundary layer and also affect the precipitation and

cloud formation by controlling the amount of energy that goes back to the atmosphere

(Chen and Zhang, 2009). Noah LSM treats C_h and C_e as equal. Noah LSM calculates the

surface-exchange coefficient for heat (C_h) using a similarity theory-based stability

function of Paulson (1970). It uses aerodynamic roughness length (z_{0m}), thermal

roughness length (z_{0t}), and current atmospheric conditions. The equation to calculate C_h

in Noah LSM is given by Chen et al. (1997) as

$$C_h = \frac{k^2/R}{\left[ln\left(\frac{z}{z_{om}}\right) - \psi_m\left(\frac{z}{L}\right) + \psi_m\left(\frac{z_{om}}{L}\right)\right]\left[ln\left(\frac{z}{z_{ot}}\right) - \psi_h\left(\frac{z}{L}\right) + \psi\left(\frac{z_{ot}}{L}\right)\right]} \quad (3.19)$$

where k is the von Kármán constant, z is the reference height within the surface layer, R

is the ratio of exchange coefficients for momentum and heat in the neutral limit estimated

at 1.0, and L is the Obukhov length given by

$$L = -\frac{\overline{\Theta_v}u_*^3}{kg\overline{w'\Theta_v'}} \quad (3.20)$$

where Θ_v is the virtual potential temperature, u_* is the friction velocity, g is the

acceleration of gravity, and w is the vertical wind velocity. The stability functions Ψ_m and

Ψ_h are given by

$$\Psi_m = \begin{cases} -5\zeta & 0 < \zeta < 1 \\ 2\ln\left(\dfrac{1+x}{2}\right) + \ln\left(\dfrac{1+x^2}{2}\right) - 2\tan^{-1}(x) + \dfrac{\pi}{2} & -5 < \zeta < 0 \end{cases} \qquad (3.21)$$

$$\Psi_h = \begin{cases} -5\zeta & 0 < \zeta < 1 \\ 2\ln\left(\dfrac{1+x^2}{2}\right) & -5 < \zeta < 0 \end{cases} \qquad (3.22)$$

where $\zeta = z / L$ and $x = (1 - 16\,\zeta)^{1/4}$. Within Noah, z_{0t} is calculated according to

Zilitinkevich (1995) as

$$z_{ot} = z_{om} \times \exp\left(-k\,C_{zil}\sqrt{R_e}\right) \qquad (3.23)$$

where z_{0m} is based on the vegetation category (read from the vegetation look-up table;

Appendix A and Appendix B) and k is the von Kármán constant. The empirical

coefficient, C_{zil}, has a value of 0.1 in the existing model selected based on FIFE field

observations (Chen et al., 1997). Several studies have found that the Noah LSM tends to

overestimate sensible heat flux with the existing parameterization of C_h equation (Chen et

al., 2010; Hogue et at., 2005; LeMone et al., 2008). Chen and Zhang (2009) showed that

by using 0.1 for C_{zil}, C_h was overestimated for short vegetation and underestimated for

tall vegetation. They proposed a new formulation to derive C_{zil} as a function of z_{om},

which is in turn dependent on the vegetation type. The new relationship was tested for

different land-cover types at different places in the US and showed better results. The
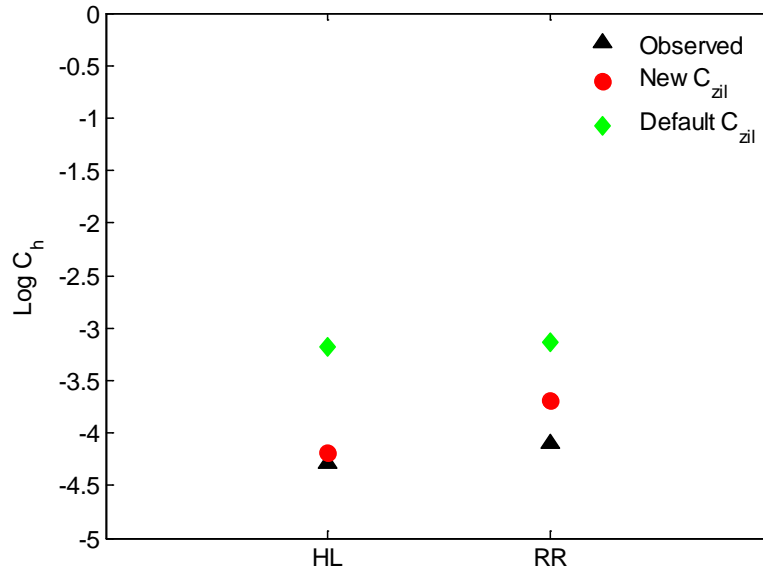
Figure 3.5. The Median Values of C_h for Four Months from March to June in 2010. Observations Are Represented by Black Triangles, Noah C_h Values Using the Default $C_{zil}=0.1$ Are Represented by Green Diamonds, and Noah C_h Values with New Formulation Are Represented by Red Circles

new formulation for C_{zil} was used here, which was derived from z_{0m}, for the vegetation type.

$$C_{zil} = 10^{\left(-0.4 \times \frac{z_{om}}{0.07}\right)} \tag{3.24}$$

Derived C_{zil}, using the above equation, is always higher than the default value 0.1. In 2010, the mean value of C_{zil} for winter is 0.92, which was reduced to a mean value of 0.51 for summer. Figure 3.5 shows the variation of log C_h using the new equation for C_{zil} in Noah model when compared with observations at HL shrubland and RR grassland sites. Therefore, in this study, we employed Equation (3.24) to compute C_{zil}, which will

be used in Equation (3.23) to calculate z_{ot}. The formulation to calculate C_h was not changed, but affected with the new z_{ot} calculations.

3.1.3 Noah LSM Input Data

3.1.3.1 Forcing Fields

Forcing data fields and their measurement heights are given in Table 3.1. These data were obtained from the NCEP North American Regional Reanalysis (NARR) data set. It was developed at the Environmental Modeling Center (EMC) of NCEP. With ground observations, NARR was generated using the NCEP Eta model, its Data Assimilation System, and a recent version of the Noah LSM (Mesinger et al., 2006; Luo et al., 2007). NARR data are three hourly composites and cover the North American domain with a horizontal resolution of 0.3 degrees (32 km). The model domain has 45 vertical atmospheric levels. These levels ranges from pressure levels 1000 millibar to 100 millibar in the atmosphere. The height is roughly around 14 km or 15 km, varying with

Table 3.1. Forcing Data and Their Measurement Heights Obtained from NARR

Forcing Data	Unit	Measurement Height (m)
Air Temperature	K	2
Atmospheric Mixing Ratio	$kg\ kg^{-1}$	2
U Component of the Horizontal Wind	$m\ s^{-1}$	10
V Component of the Horizontal Wind	$m\ s^{-1}$	10
Surface Pressure	Pa	0
Precipitation Rate	$kg\ m^{-2}$	0
Downward Shortwave Radiation Flux at the Surface	$W\ m^{-2}$	0
Downward Longwave Radiation Flux at the Surface	$W\ m^{-2}$	0

time and space. It is a long-term data set and covers the period from 1979 to present. The observational data used in the data assimilation includes temperature, wind, moisture, and pressure. There are other data added or improved upon for NARR, including gridded analysis of rain gauge precipitation over the Continental US, Mexico, and Canada.

For the HRLDAS platform to run Noah LSM, all of the forcing fields are required for each hour in the simulating period. Therefore, three hourly NARR data was interpolated into hourly data in HRLDAS.

3.1.3.2 Initialization Fields

At the initial time step, Noah LSM should be provided with the initial conditions of the land surface. This includes the water and energy states at the beginning of the simulation (Rodell et al., 2005). This would lead to better simulations of the surface processes. Required initialization fields are soil temperature and soil moisture at each soil layer, canopy water content, skin temperature, and water equivalent of the snow depth. These data were also extracted from NARR. By providing area-specific soil moisture and temperature, it will reduce the requirement of spin-up years. Accurate initial conditions are critical in the regions where land and atmospheric feedback is strong. Erroneous initializing data can lead to incorrect and biased model outputs (Rodell et al., 2005).

3.1.3.3 Parametric Fields

These consist of both static and time variables. A time variable is the green vegetation fraction (GVF) based on 5-year monthly averages of the Normalized

Difference Vegetation Index (NDVI). NDVI is calculated using 0.15° Advanced Very

High Resolution Radiometer (AVHRR) data (Chen et al., 2007). GVF is based on the

expression developed by Gutman and Ignatov (1998).

$$GVF = \frac{NDVI - NDVI_{min}}{NDVI_{max} - NDVI_{min}} \tag{3.25}$$

The green vegetation fraction is an important first order parameter identified by

Jacquemin and Noilhan (1990) from a sensitivity analysis. It acts as a weighting factor to

partition total ET into three categories, the bare soil evaporation, transpiration, and

canopy evaporation (Chen and Dudhia, 2001a). Others are static fields namely latitude,

longitude, vegetation category, soil texture, minimum and maximum GVF for a typical

year, and time invariant deep soil temperature. These data are produced by the WPS

program. Soil texture data comes from 1 km resolution State Soil Geographic

(STATSGO) soil data, which has 19 categories (Appendix B). According to the

STATSGO soil data, silt loam and loam are the most common soil types in the area

(Figure 3.6). Roughly 50% of the crop area is silt loam. MODIS-based land-surface

characterization provided the land-cover types for this study. Figure 3.7 shows the land-

cover types according to the MODIS-based classification. The study area mostly consists

of grassland. Only 7% of the area is classified as cropland.
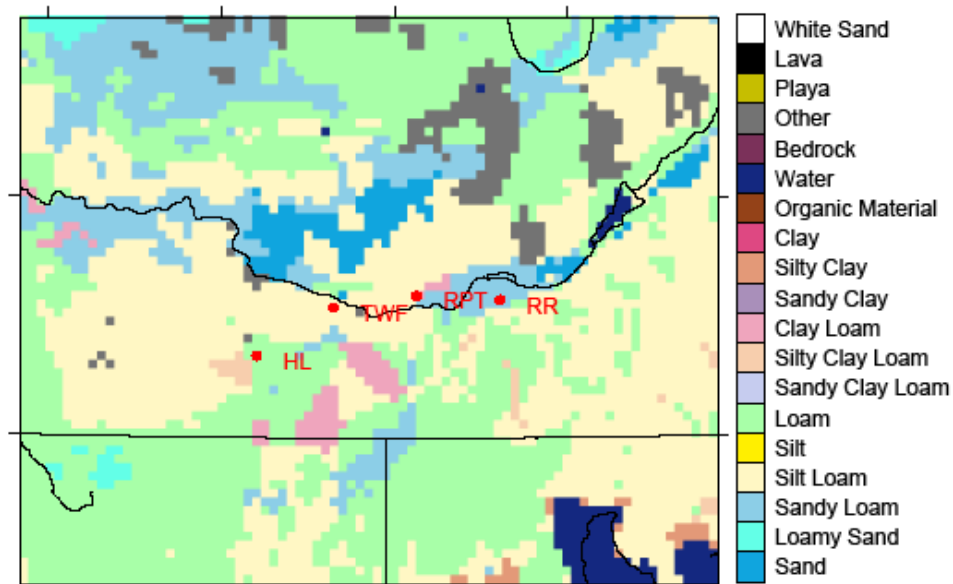
Figure 3.6. Soil Types in the Study Area Based on State Soil Geographic (STATSGO) Classification. Four Measurement Sites Are Shown with Red Circles: HL - Hollister, TWF - Twin Falls, RPT - Rupert, and RR - Raft River.
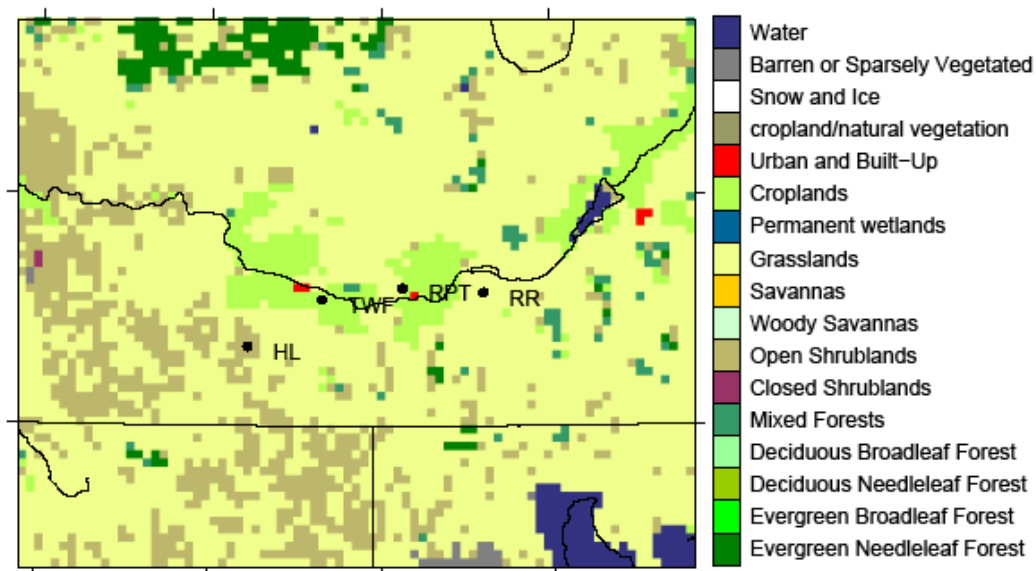
Figure 3.7. Vegetation Types in the Study Area According to the MODIS-Based Classification. Four Measurement Sites Are Shown with Black Circles: HL - Hollister, TWF - Twin Falls, RPT - Rupert, and RR - Raft River.

3.2 Weather Research and Forecast Model

WRF has been developed as a collaborative effort of several agencies in order to improve the understanding and predictability of mesoscale weather (Skamarock et al., 2005). It is considered to be a state-of-the-art weather forecasting model. There is a two-way feedback between the atmosphere and the land surface in WRF. Some atmospheric conditions are forced to drive the land-surface processes and influence the land-surface condition, and in turn the land-surface processes influence the atmospheric processes, especially in the planetary boundary layer.

WRF has a number of options for model physics. These model physics are divided into six categories with each one having several options. Those categories are 1) microphysics, 2) cumulus parameterization, 3) planetary boundary layer (PBL), 4) surface layer, 5) land surface model, and 6) radiation scheme. In model execution, radiation scheme is called first to obtain the radiative forces required for the LSM. Radiative fluxes along with previous time step's precipitation from the microphysics and cumulus scheme are used by the LSM. Heat and moisture fluxes from the LSM are then fed to the boundary-layer scheme. Appendix D shows a schematic diagram of WRF. According to Skamarock et al. (2005) and the User's Guide for Advanced Research WRF (ARW) version 3.1 (NCAR, 2010), the purposes of the above schemes are as follows.

3.2.1 WRF Schemes

    3.2.1.1 Microphysics

Microphysics explicitly resolves water vapor, cloud, and precipitation processes in modeling. Under microphysics, there are eleven options for physics.

1. Kessler scheme

2. Purdue Lin scheme

3. WRF Single-Moment 3-class scheme

4. WRF Single-Moment 5-class scheme

5. WRF Single-Moment 6-class scheme

6. Eta Grid-Scale Cloud and Precipitation scheme

7. Thompson et al. scheme

8. Goddard Microphysics scheme

9. Morrison Double Moment scheme

10. WRF Double-Moment 5-Class scheme

11. WRF Double-Moment 6-Class scheme

Purdue Lin scheme (Lin et al., 1983; Rutledge and Hobbs, 1984) was selected for this study. This has been recommended for researches with real data and high resolution simulations (WRF-ARW V3.1: User's Guide). The hydrometeors in this scheme include water vapor, cloud water, rain, cloud ice, snow, and graupel (snow pellets).

3.2.1.2 Cumulus Parameterization

Sub-grid-scale effects of convective and/or shallow clouds are represented by cumulus parameterization. The five options available are

1. Kain-Fritsch scheme

2. Betts-Miller-Janjic

3. Grell-Devenyi ensemble

4. Grell 3D ensemble cumulus scheme

5. Old Kain-Fritsch scheme

Generally, cumulus parameterizations are advised for use on coarser grid sizes (greater than 10 km). Grell 3D ensemble cumulus scheme was selected here as it is suitable for higher resolution domains since it allows subsidence in neighboring columns.

3.2.1.3 Planetary Boundary Layer

This resolves sub-grid-scale fluxes due to eddy transports in the whole atmospheric column. With surface fluxes from the land surface model, PBL scheme determines the flux profiles within the well-mixed boundary layer and stable layer. The options are

1. Medium Range Forecast Model (MRF) PBL

2. Yonsei University (YSU) PBL

3. Mellor-Yamada-Janjic (MYJ) PBL

4. Asymmetric Convective Model 2 (ACM2) PBL

5. Large Eddy Simulation (LES) PBL

6. Quasi-Normal Scale Elimination PBL

7. Mellor-Yamada Nakanishi and Niino Level 2.5 PBL

8. Mellor-Yamada Nakanishi and Niino Level 3 PBL

9. Bougeault-Lacarrere (BouLac) PBL

MYJ PBL (Janjic, 1990, 1996, 2002; Mellor and Yamada, 1982) was used in the model for this study. This is an operational scheme that calculates turbulent kinetic energy important in developing the PBL from effects of the land surface. This scheme is also used in the ETA model.

3.2.1.4 Surface Layer

This scheme is responsible for friction velocities and exchange coefficients that will be used in surface heat and moisture flux calculations in LSMs and surface stress in the PBL scheme. There are five options;

1. Similarity Theory (MM5)

2. Similarity Theory (ETA)

3. Pleim-Xiu surface layer

4. Quasi-Normal Scale Elimination (QNSE) surface layer

5. Mellor-Yamada Nakanishi and Niino (MYNN) surface layer

Similarity theory, which was used in the Eta model, was chosen. It is based on Monin-Obukhov similarity theory (Monin and Obukhov, 1954) with Zilitinkevich (Zilitinkevich, 1995) thermal roughness length. This should be run in conjunction with the MYJ PBL scheme.

3.2.1.5 Land Surface Model

An update of land-surface states is achieved by this scheme by using the atmospheric information from the land-surface scheme, radiative forcing from the radiation scheme, precipitation from the microphysics and cumulus schemes, along with other land-surface properties and variables. The LSM provides heat and moisture fluxes from the underlying land surface to the atmosphere, creating the lower boundary conditions. There are four options available, which are

1. 5-Layer Thermal Diffusion

2. Noah Land Surface Model

3. Rapid Update Cycle (RUC) Land Surface Model

4. Pleim-Xiu Land Surface Model

Noah LSM was selected to be comparable with the uncoupled model. A description about the Noah LSM is given in Section 3.1.1.

3.2.1.6 Atmospheric Radiation Physics

This scheme determines the atmospheric heating due to longwave and shortwave radiation fluxes. Infrared and/or thermal radiation emitted or absorbed by the gasses and land surface fall under longwave radiation. Shortwave incoming radiation comes from the Sun with wavelengths belonging to the solar spectrum and subjected to absorption, reflection, and scattering in the atmosphere, as well as at the land surface. Surface albedo causes upward shortwave flux. The effect of model predicted clouds, water vapor, and different gasses on radiation flux is also included in this scheme. There are several

options for both longwave and shortwave radiation schemes. The options for longwave

radiation are

1. Rapid Radiative Transfer Model (RRTM) Longwave scheme

2. Eta Geophysical Fluid Dynamics Laboratory (GFDL) Longwave scheme

3. Community Atmosphere Model (CAM) scheme

4. RRTMG (Rapid Radiative Transfer Model for GCMs) scheme

Shortwave radiation scheme options are

1. MM5 (Dudhia) Shortwave scheme

2. Goddard Shortwave

3. Eta Geophysical Fluid Dynamics Laboratory (GFDL) Shortwave scheme

4. Community Atmosphere Model (CAM) scheme

5. RRTMG (Rapid Radiative Transfer Model for GCMs) shortwave

RRTMG shortwave and longwave schemes were chosen for this study. This is the

latest option and it has the ability to handle the clouds well.

3.2.2 WRF Input Data

Unlike Noah LSM, WRF requires only the initial conditions at the beginning and

the lateral-boundary conditions at specific time intervals while it is running. This data

was also acquired from the NARR model output. The frequency of the provided

boundary conditions was three hours.

Vegetation, soil, elevation, land-water masks, and monthly vegetation field data are common for both WRF and HRLDAS created by the WPS program. For parameters related to vegetation and soil, both models share the same look-up tables.

3.3 Complementary Relationship

3.3.1 Theoretical Background on Complementary Relationship

Bouchet (1963) hypothesized that with enough moisture available, ET increases and approaches PET. This condition is denoted by a term called equilibrium ET (ET_w), which takes place from a well-watered natural surface covered with vegetation. Under water-limited conditions, independent from the available energy, ET decreases below ET_w, creating a certain amount of energy, Q, available.

$$ET_w - ET = Q \tag{3.26}$$

This available energy Q is used for sensible heat flux. As a result, air temperature increases and humidity decreases, causing an increase in PET by an amount of Q.

$$ET_w + Q = PET \tag{3.27}$$

The CR can be obtained by combining Equations (3.26) and (3.27), which is given by

$$ET + PET = 2ET_w \qquad (3.28)$$

The above is a symmetric CR. That is a one unit decrease in ET results in one unit increase in PET. Figure 3.8 shows the schematic diagram of a theoretical complementary relationship. A general form of CR can be written as

$$(1 + b)ET_w = PET + bET \qquad (3.29)$$

where b is proportionality constant. In symmetric CR, b becomes one. However, Kahler and Brutsaert (2006) explained that b can take values greater than 1 when pan evaporation is used. This happens due to the energy received from exposed sides and bottom of the pan and larger water vapor transfer coefficient from local advection due to its small size.
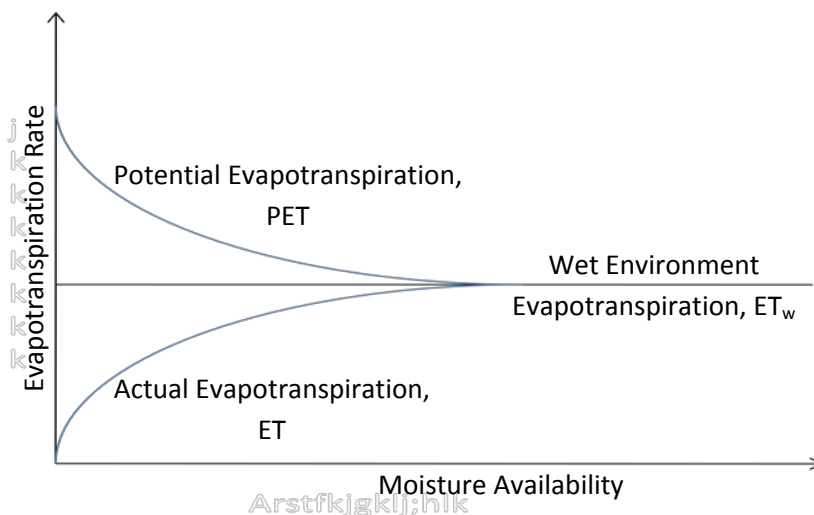
Figure 3.8. Schematic Diagram of Complementary Relationship

3.4 Experimental Setup

3.4.1 Noah LSM

The model domain (Figure 2.1) was divided into 81 x 66 cells with 4 km resolution using the WPS program. All weather forcing data and data for the initial conditions were interpolated spatially into 4 km and temporally into 1 hour in the HRLDAS platform. Interpolation of the parametric fields was carried out by WPS program. Resolution on the order of 2 km was recommended by a previous study (Sridhar et al., 2003) in order to best represent the highly heterogeneous regions. However, since the resolution of input weather data is coarse (32 km for NARR), going to a resolution higher than 1 km may not be of much help. The resolution of 4 km was selected considering the computational difficulties arising due to long-term model runs, data processing, and storage.

The total depth of the soil column was 2 m with the root zone depths read from the vegetation look-up table. HRLDAS v3.1 was used to run Noah LSM in an uncoupled mode with the changes explained in Section 3.1.2. Four experiments were performed. Long-term simulations were done for 30 years with 4 km spatial resolution and with the irrigation scheme in it. The Noah LSM was initialized at 00 hour in 1 January 1979. The first 24 months were treated as the spin-up period. Model simulations spanned through 31 December 2010 in 1 hour time steps. Vegetation information is static for the whole simulation period. Short-term simulations were done from 1 January 2008 through 31 December 2010 in two ways, leaving 2008 simulation year as the spin-up period. The first experimental simulation was with the irrigation scheme and the spatial resolution of

4 km. The second experiment was without irrigation but with a 4 km resolution in order

to access the effects of irrigation. The last experimental set up was with an irrigation

scheme, but from 1 January 2009 through 31 December 2010. Only 2009 simulation year

was excluded as the spin-up period in order to evaluate suitable spin-up time for this

region.
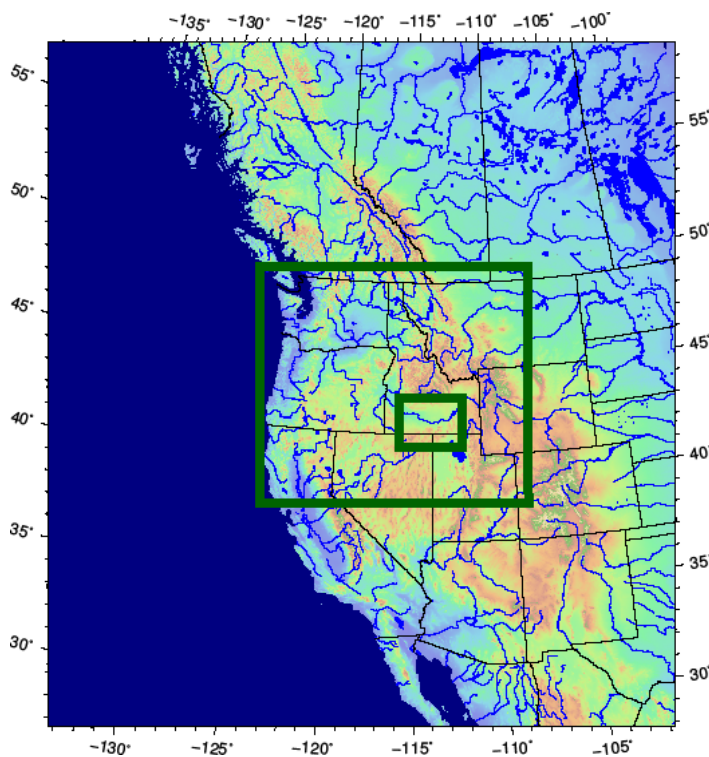
Figure 3.9. Outlines of the 3 WRF Domains (Outermost Domain Is the Figure Box)

3.4.2 WRF

The output from WRF V3.2.1 was used in this study with three nested domains.

WRF output was obtained from a parallel project carried out at Boise State University.

Three model domains were created with the innermost domain being the same as the

domain used in Noah LSM (Figure 3.9). The outermost domain is 36 km in resolution with 98 rows and 89 columns of grid cells. The middle domain has 102 x 114 grid cells of 12 km and it helps to resolve orographic effects. The innermost domain is 4 km and consists of 81 x 61 grid cells. All three domains have 38 vertical grid cells of varying heights, with the lowest having an average height of 36 m. Due to the extensive computational power required, WRF results were obtained only for a selected time period of 1 March 2010 to 30 September 2010.

3.5 Validation

Both inputs and outputs of the model were subjected to validation. Model forcing data extracted from NARR was verified using the data collected from field observation sites at HL and RR and AgriMet weather stations. This kind of verification is necessary since the NARR data used to force the models are also modeled data. It is important to know if the errors in the input data are significant enough to propagate in the model output. When Chen et al. (2007) verified their input data against IHOP_2002 field observations, they found that NCEP stage-IV rainfall was slightly overestimated in dry regions and underestimated over the transitional and wet regions. While the largest error was found in satellite-derived solar radiation, other atmospheric forcing data obtained from NCEP EDAS were accurate with low errors.

Model output was validated in two ways, as spatial data and point-scale data. For point-scale output, data for the station locations were extracted. Spatial validation was

done by comparing the model-simulated ET estimates with METRIC images for the years

1996, 2000, 2002, and 2006.

3.5.1 Field Observations

The surface energy balance components for the model, latent heat, sensible heat,

ground heat, and net radiation, were validated against fluxes measured at HL and RR

sites in 2010. The input variables of air temperature and precipitation were validated by

comparing them with the field observations. These variables are important drivers of

land-surface processes and have been measured at all observation sites.

3.5.2 METRIC Images

METRIC (Satellite-Based Energy Balance for Mapping Evapotranspiration with

Internalized Calibration) is a satellite-based, surface energy balance model to predict

evapotranspiration. It uses an image processing tool, such as ERDAS, to link various

modules (Allen et al., 2007a). It calculates actual ET as a residual of energy balance

using satellite images containing both shortwave and thermal information. It is based on

another satellite-based model, SEBAL (Bastiaanssen et al., 1998). The intention was to

produce higher resolution spatial maps of ET with more accuracy compared to other

models. The resolution of the ET map depends on the resolution of the satellite images.

METRIC computes net radiation, soil heat flux and sensible heat flux, and ET, then is

calculated as the residual according to the energy balance equation. It has been designed

to be calibrated internally using ground-based alfalfa reference ET, calculated from

hourly weather data. The instantaneous ET computed for the time of the satellite image can be converted to daily ET or seasonal ET using a reference ET fraction (ET_rF). It assumes the ET_rF at the image time is the same as the average ET_rF over the day (24 hour) in calculating the daily ET. METRIC provides useful information of ET, which can be used in the field for various purposes. Monitoring water-rights compliance and aquifer depletion in Idaho, mapping ET from agricultural and riparian vegetation in New Mexico, and assessing irrigation adequacy and salinity management in California are examples of usages of METRIC in the field (Allen et al., 2007b).

CHAPTER FOUR: VALIDATION AND RESULTS OF IRRIGATION IN THE

MODEL

4.1 Evaluation of NARR Data with Field Observations

4.1.1 Air Temperature

Air temperature from the NARR (North American Regional Reanalysis) data set

was compared against field observations at Hollister (HL) and Raft River (RR) for 2010,

and at Twin Falls (TWF) and Rupert (RPT) for 20 years from 1991-2010. A comparison
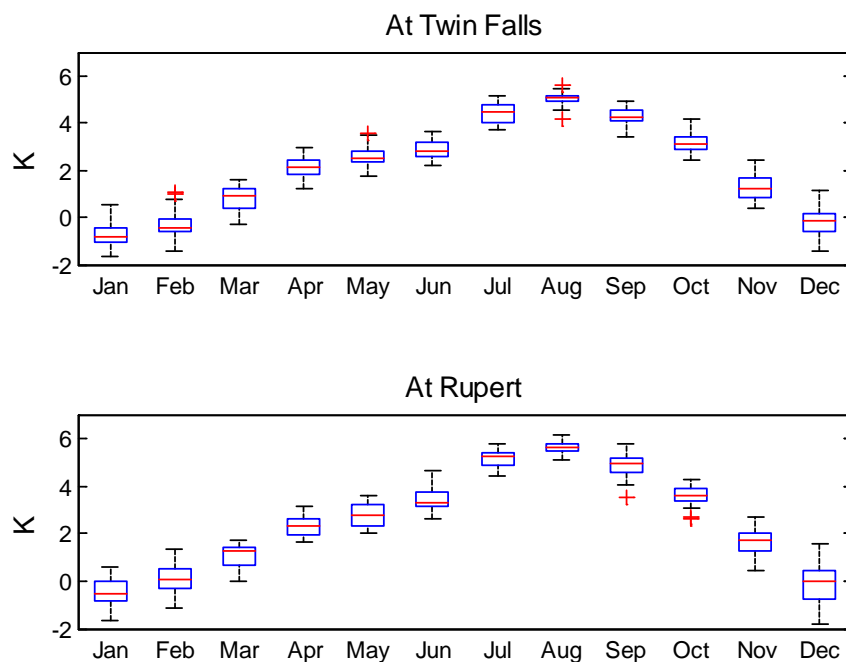
**Figure 4.1. Box Plot of Mean Daily Temperature Difference (NARR – AgriMet)
Between NARR and Measured at AgriMet Weather Stations at Twin Falls (Top)
and Rupert (Bottom) Averaged over 20 Years from 1991-2010**

of daily average temperature showed that NARR temperature was slightly higher during the summer. The root mean squared error (RMSE) of air temperature for the natural vegetation at HL and RR was around 3 °K. The same for the agricultural lands were 4 °K and 4.5 °K at TWF and RPT. NARR temperature had a bias of around 2 °K when compared with measured air temperature at AgriMet weather stations, while it was below 1 °K for natural vegetation sites. It was observed that the errors/bias for the wintertime were generally low as observed by Chen et al. (2007). Figure 4.1 is the box plots of the daily average temperature differences at TWF and RPT for each month and Figure 4.2 is the same at HL and RR for 2010. For TWF and RPT, average temperatures for each day
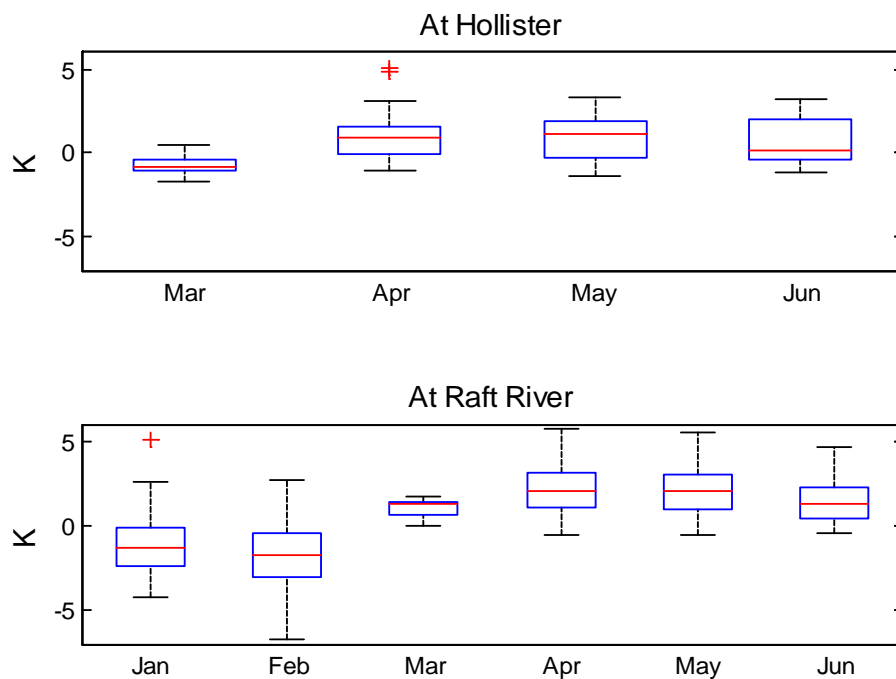
Figure 4.2. Box Plot of Mean Daily Temperature Difference (NARR – Observed) Between NARR and Measured at Hollister and Raft River for 2010

for all 20 years were computed and the difference was taken. It is shown from Figures 4.1 and 4.2 that during winter months, NARR has a cold bias, and during the summer months NARR has a warm bias.
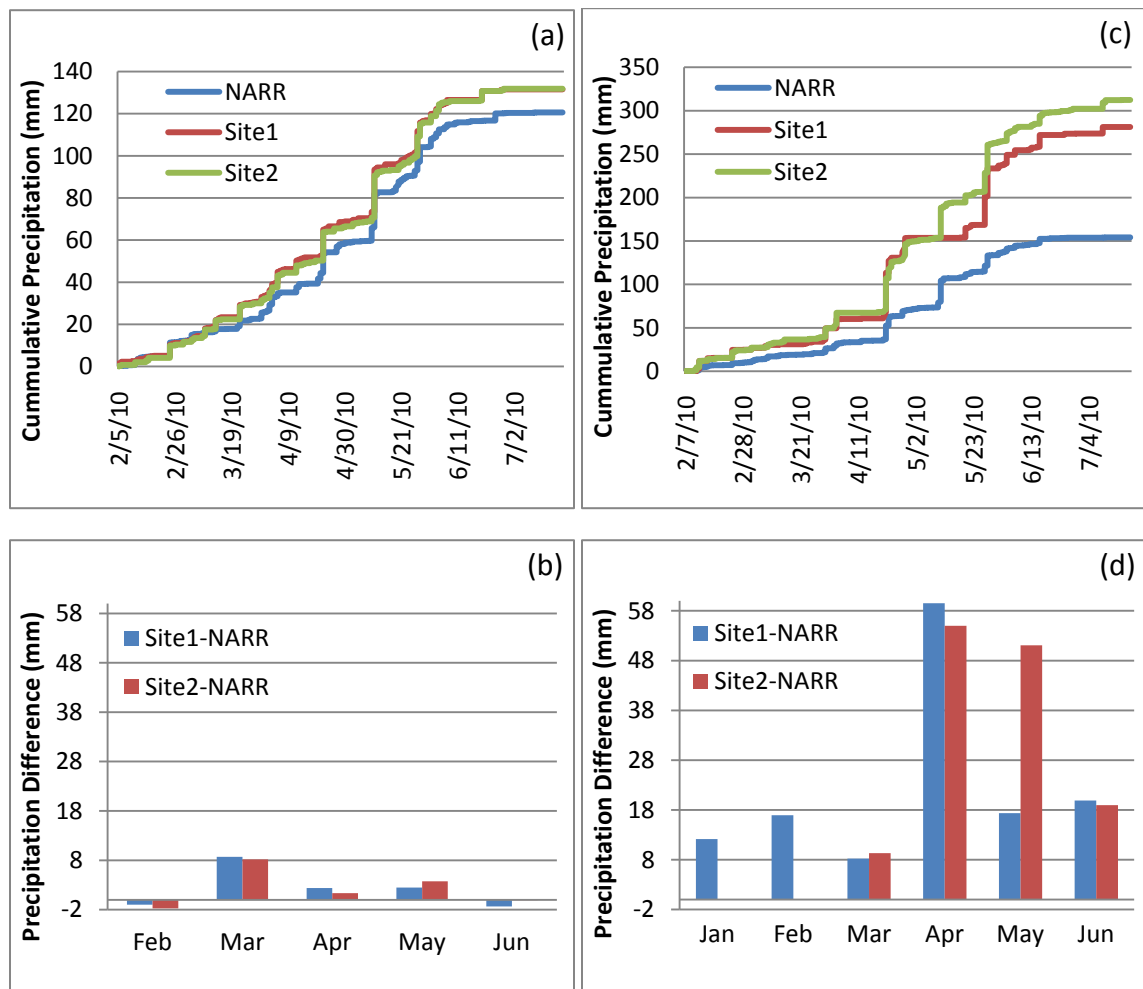
Figure 4.3. Comparison of Precipitation Data from NARR with Field Observation at (a) HL and (c) RR. The Differences in Monthly Precipitation Is Shown in (b) for HL and in (d) for RR.

4.1.2 Precipitation

Comparisons were made between NARR and field-measured precipitation. At

HL, for the period from 02/05/2010 – 07/20/2010, NARR underestimated 11 mm of the

total precipitation. Underestimation for RR was higher, which were 127 mm and 158 mm

compared with measurements at two sites for the period 02/07/2010 – 07/19/2010. Figure

4.3 shows the cumulative precipitation for the whole period and monthly underestimation

at two sites. At HL, underestimation was high in March. Raft River recorded the highest

underestimation in April, while all April, May, and June were higher compared to

January – March.

4.2 Evaluation of Field Observations

4.2.1 Energy Budget Closure

The energy balance closure was checked as a quality measure of the site data.

Many studies have found that the measured turbulent fluxes, which are sensible heat flux

(SH) and latent heat flux (LH), from the eddy covariance (EC) method do not close the

energy budget (Wilson et al., 2002; Foken, 2008; Maayar et al., 2008; Lei and Yang,

2010). In most of the experiments, this is due to the overestimation of available energy

(R_n - G) or underestimation of SH and/or LH. Wilson et al. (2002) summarized the

primary reasons for the imbalance as systematic errors related to sampling mismatch

between the flux footprint and the sensor, instrument bias, neglected energy sinks like

heat storage in soil, low and high frequency loss of turbulent fluxes, and advection of

heat and vapor. This has a significant effect when the unclosed data is used to validate the models (Maayar et al., 2008).

Correlation coefficient and linear-regression coefficients between available energy and the sum of SH and LH were calculated for the two locations, HL and RR, using half-hourly data. For an ideal energy balance closure, the slope and intercept should be 1 and 0, respectively. As the first step, average values of fluxes for all instrumentation sites at a location were computed as the arithmetic mean of each time step. Then, the spikes in the measurements were removed. The spikes were seen in measured SH from scintillometer and EC site 1 at HL (Figure 2.2), and only from scintillometer at RR. LH measurements from EC site 1 at HL contained spikes in the measurements. Figure 4.4 shows the scatter plots turbulent fluxes (SH + LH) Vs available energy (R_n - GH) for HL
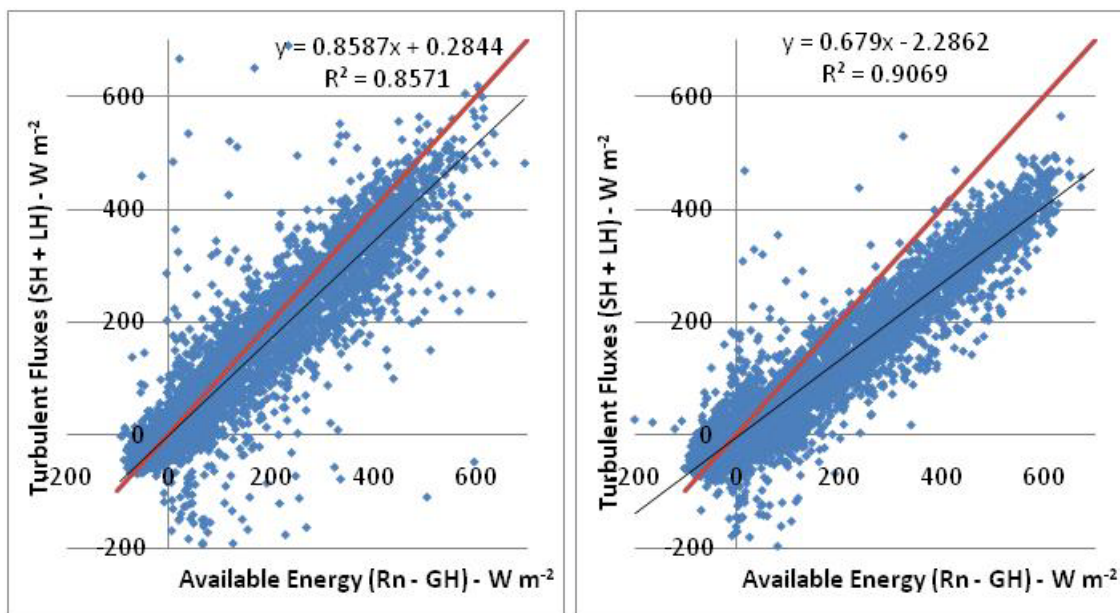
Figure 4.4. Energy Balance Closure at Two Sites: Hollister (HL; Top) and Raft River (RR; Bottom). Red Line Is the 1:1 Line and Black Line Is the Regression Line with the Equation Mentioned on the Figure

and RR sites. With slope values of 0.86 and 0.68 at HL and RR, respectively, both cases

indicated that the SH and/or LH has been underestimated. Average underestimation for

the whole period was about 14 W m^{-2} for HL and 24 W m^{-2} for RR. Even with a greater

correlation coefficient at RR, underestimation was higher than at HL. However,

compared with the ranges of slope and intercept reported from other studies (Wilson et

al., 2002; Lei and Yang, 2010), the statistics for these two sites were reasonable.

4.3 Validation

4.3.1 Validation with Field Measurements

Hourly averaged LH and SH of measured data were compared against the same

from Noah LSM. Figure 4.5 and Figure 4.6 shows the mean hourly fluxes only for May

and June in 2010. Table 4.1 shows the daily total energy of fluxes for each month from

measurements and Noah LSM. Noah has underestimated SH in January, February, and

March for HL, while from April to June the fluxes are close to the measurements (within

10% of measured fluxes). From January to March, the peak SH from Noah LSM was 66

W m^{-2} (average for the three months) less than the observed. In all months from January

to June except February, SH has been overestimated by Noah for RR, most of the time

more than 100%. LH has been overestimated by Noah in January and February at RR. At

HL, overestimation of LH was significant in January and June (i.e., overestimation was

more than 10% of the measured flux). Part of the overestimation of SH and LH by Noah

LSM can be explained by the poor energy balance closure at the site (i.e.,

underestimation of SH and/or LH at both sites). At RR, SH and/or LH were
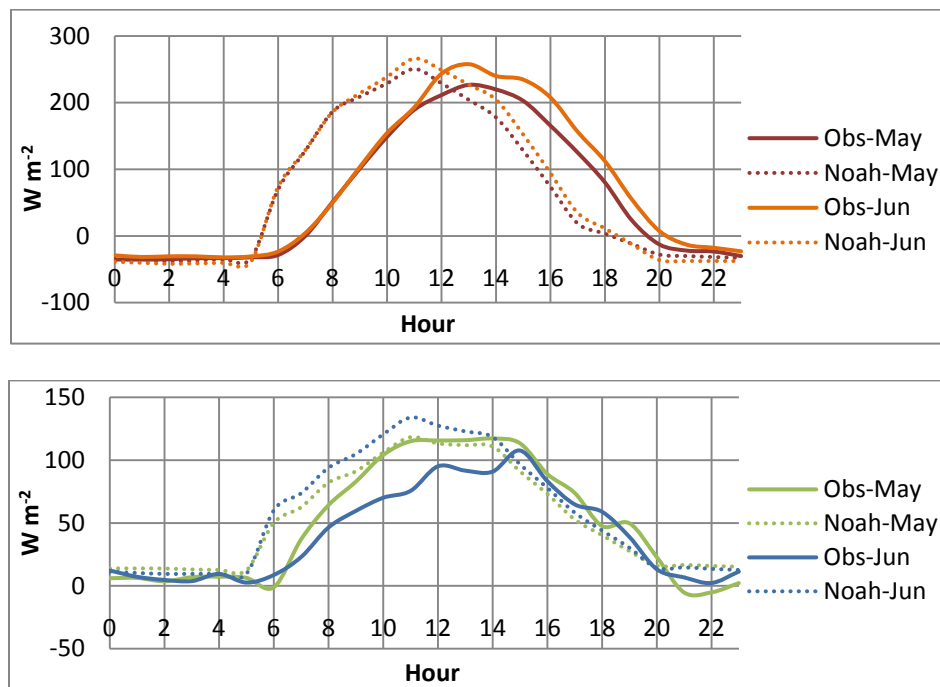
Figure 4.5. Measured and Noah LSM Sensible (Top) and Latent (Bottom) Heat at Hollister

underestimated by roughly 30%; and at HL, it was by 15%. This can lead to lower SH and/or LH values from sites compared to the Noah LSM. When all the measured fluxes were checked, it was observed that there was a residual term in almost every month.

Another important point visible from these plots was the difference in the time of peak fluxes. Fluxes from Noah LSM peak about two hours earlier than the observations. In observed fluxes, the peak happens around 1 p.m. when the Noah LSM fluxes peak around 11 a.m. This can be explained with the frequency of radiation data taken from NARR. NARR data comes in every three hours. Hours during the day time are 11 a.m. and 2 p.m. The HRLDAS platform interpolates and obtains the input data for the intermediate hours. Since the NARR data does not come at 1 p.m., the radiation data
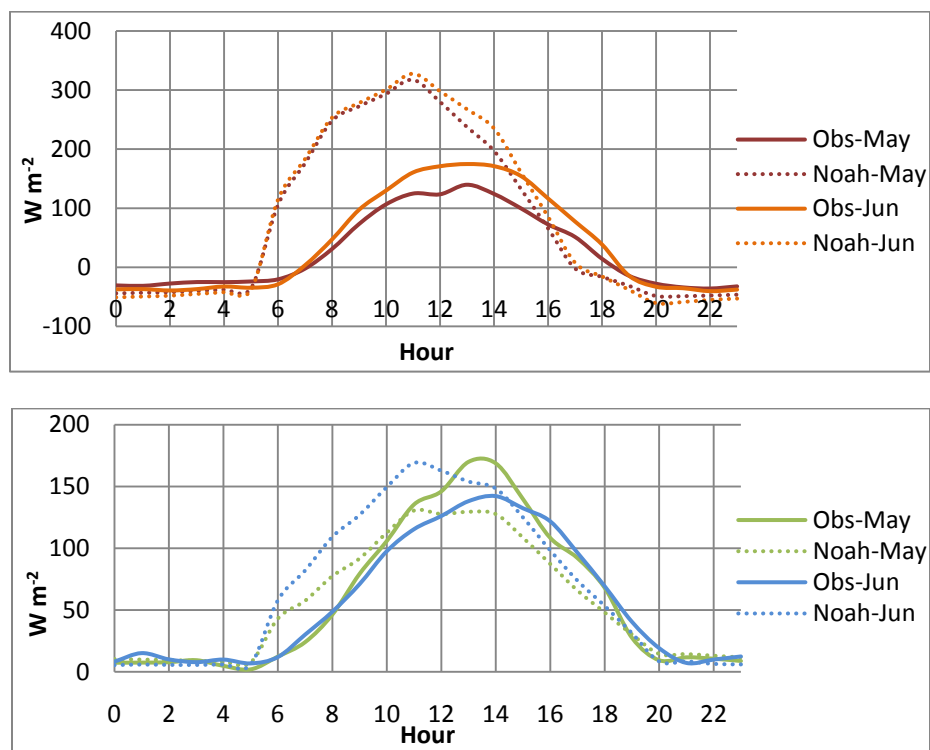
Figure 4.6. Measured and Noah LSM Sensible (Top) and Latent (Bottom) Heat at Raft River

misses the hour where actual solar peak happens. Due to this reason, these differences in the time of peak were visible between modeled and observed fluxes.

Mean evaporative fraction (EF), which is the ratio of LH to available energy (R_n-G), was checked with the related uncertainty in terms of one standard deviation (Figure 4.7). At HL, EF was computed using the measurements from March through June 2010, and at RR from January through July 2010, depending on the availability of the measured data. At both sites, Noah LSM produced EFs agreed well with EFs calculated from measured fluxes at two sites. The variation/uncertainty of the EFs is larger in the morning hours and the night time. LH is relatively small during the night time and morning hours,

Table 4.1. Daily Total Energy Fluxes (MJ m^{-2} day^{-1}), from Site Measurements and Noah LSM, for Each Month for Hollister (HL) and Raft River (RR)

			Jan	Feb	Mar	Apr	May	Jun
HL	SH	Site	0.08	1.50	2.61	3.64	5.13	6.33
		Noah	-1.97	-1.35	1.27	3.70	5.62	6.04
	LH	Site	1.44		2.64	3.77	4.23	3.56
		Noah	1.81		2.76	4.02	4.59	4.96
	GH	Site		-0.02	0.36	0.49	0.66	1.50
		Noah		0.13	0.91	0.41	0.51	0.90
	R_n	Site		4.40	6.69	9.26	11.63	12.60
		Noah		0.82	5.00	8.12	10.64	11.74
RR	SH	Site	-1.56	-0.65	1.02	1.85	2.28	3.36
		Noah	-0.93	-1.07	2.86	5.92	6.63	7.03
	LH	Site	0.38	0.29	2.16	3.92	5.05	4.86
		Noah	1.17	1.67	2.18	3.23	4.84	5.77
	GH	Site	-0.15	-0.21	0.09	-0.01	0.11	0.71
		Noah	-0.29	-0.20	0.98	0.28	0.37	0.55
	R_n	Site	-1.12	-0.04	5.88	9.01	11.27	12.42
		Noah	-0.06	0.35	6.03	9.42	11.80	13.28

which consumes only a small portion of net radiation. This results in larger EF during the night time, and morning varies depending on the season. Since the period concerned here included more than one season, night time EF showed substantial variability and hence large uncertainties during the study period.

4.3.2 Comparison with METRIC

METRIC ET maps are spatial maps of ET. They show the variability of ET in space and time. This comparison would enable us to validate the Noah LSM simulated ET across the study domain. METRIC ET maps developed by IDWR (Idaho Department of Water Resources) were used in this study. These maps have been developed by using
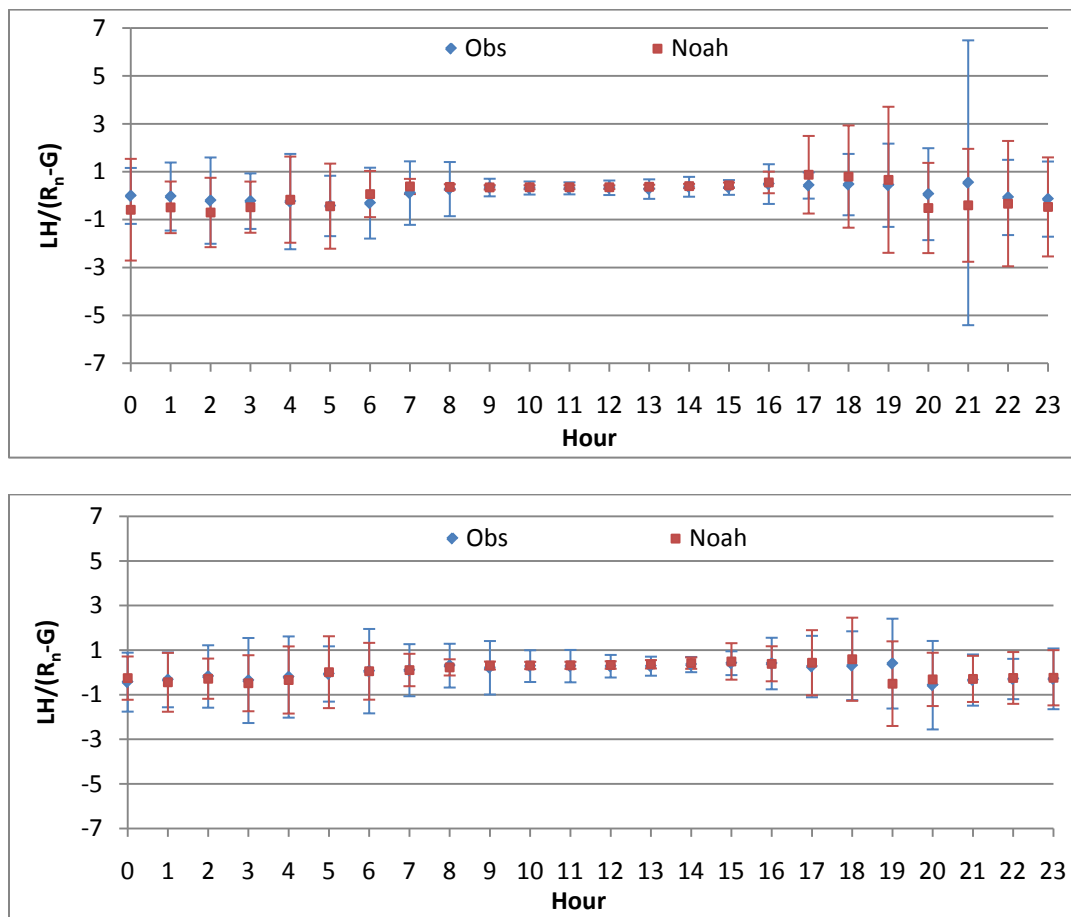
Figure 4.7. Mean Evaporative Fraction Calculated from Observations and Noah Results at Hollister (HL) and Raft River (RR)

Landsat satellite data. The resolution is 30 m and the cell values in maps represent the total ET for the particular month in millimeters. A main point to note here is that 30 m resolution METRIC ET maps were compared against the 4 km resolution Noah simulated ET (ET_{Noah}). METRIC has been developed to produce high resolution ET maps. Resampling of these maps into high resolution maps can smooth the variations of ET. Therefore, the original METRIC ET maps were not altered, but used as they were in this comparison.

Figure 4.8 shows the spatial distribution of monthly total ET from METRIC and Noah LSM from May to October in 2006. METRIC ET maps do not cover the whole model domain and thus only the section that coincides with the model domain is shown in Figure 4.8. It clearly indicates that spatial patterns of ET_{Noah} follow METRIC ET even though low resolution in Noah LSM has caused some smoothing in ET. Especially in the irrigated croplands, the application of irrigation has improved the model predictions compared to METRIC ET. Impacts of irrigation on surface energy balance and ET is discussed in Section 4.6. ET peaks in July for irrigated croplands in both models. The maximum ET in the region from METRIC is 383 mm, and from Noah LSM it is 225 mm. Appendix E shows the comparison of ET from METRIC and Noah LSM from May to October in for the years, 1996, 2000, and 2002. All these images show that compared to METRIC, Noah was able to simulate ET well with the application of irrigation.

4.4 Spin-up of HRLDAS

Spin-up is an adjustment process in which the LSM needs to achieve an equilibrium state (Yang et al., 1995). The time required for the spin-up is different for each LSM because of the differences in physical processes and parameterization in them. Rodell et al. (2005) showed that even with the same LSM, the spin-up time varies depending on the data used as initial conditions and method/data that is used during the spin-up period. They stated both meteorological and non-meteorological controls on soil moisture spin-up times. The meteorological controls include precipitation and freezing temperatures. Non-meteorological controls are soil layer depth, hydraulic conductivity,
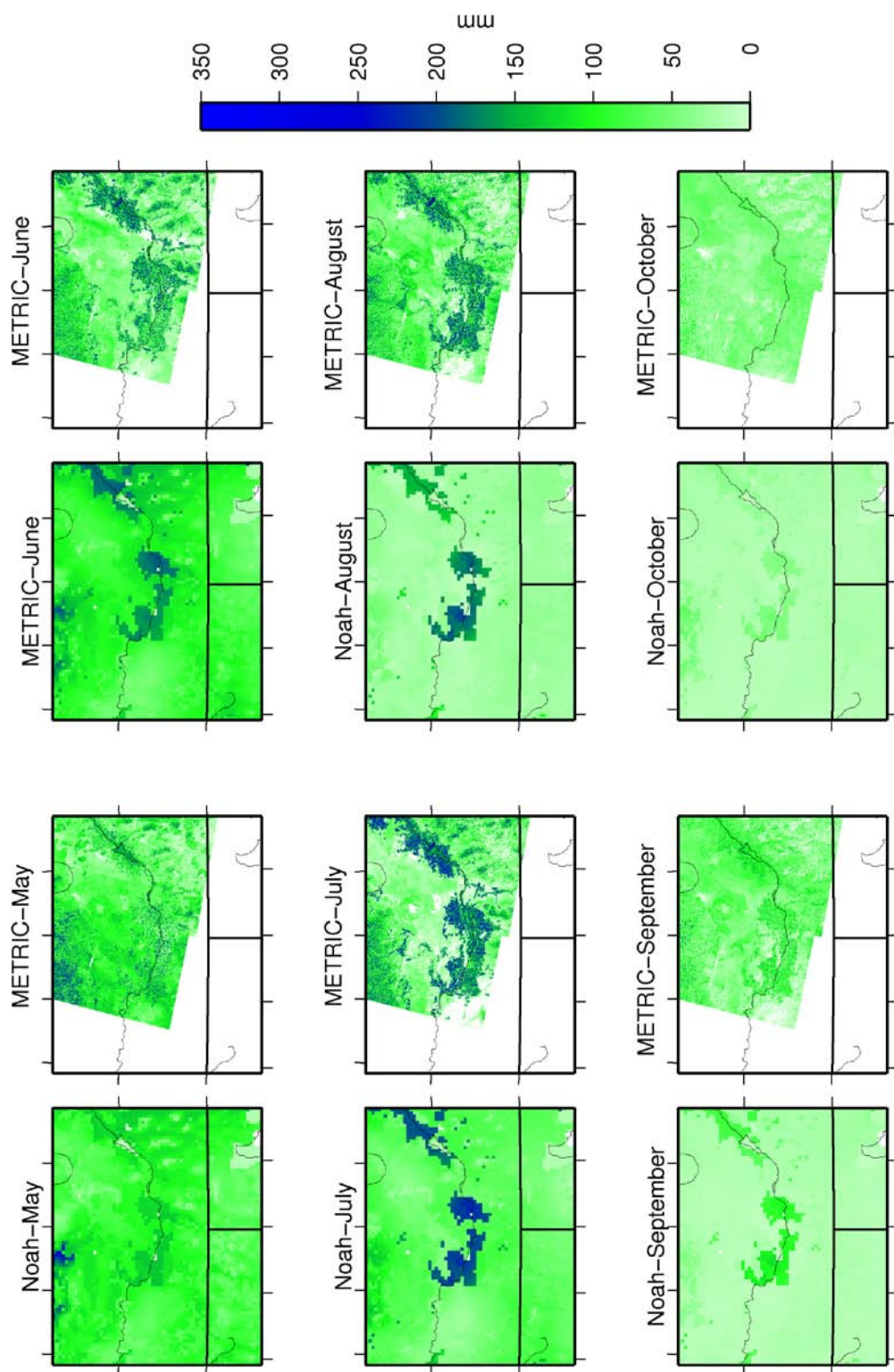
Figure 4.8. Spatial Distribution of Monthly Total ET from METRIC and Noah LSM from May to October in 2006

root depth, and persistence of snow cover. When the soil is coarse and has large soil

hydraulic conductivity, the spin-up time required is less. Chen et al. (2007) showed that

HRLDAS needs about 12 months to attain the quasi-equilibrium.

A simple experiment was done to find the suitable spin-up period for this study

area. Soil moisture in 2010 from three different model runs with different spin-up was

compared. One model run was spin-up with 2 years (2008-2009), second model run with

one year (2009), and the other one with 31 years (1979-2009). Results for 2010 from the

model runs with one and two years were compared with the results with 31-year spin-up,

assuming that after 31 years LSM has achieved the equilibrium state. Figure 4.9 shows

the comparison of soil moisture at four soil layers for three locations, RR, HL, and for an

irrigated cropland cell. As shown in Figure 4.9, soil moisture with one-year spin-up

showed some variations when compared with soil moisture with 30-year spin-up. Close

examination showed that soil moisture with 2-year spin-up was closer to an equilibrium

Table 4.2. RMSE of Simulated Surface Fluxes for Two Sets of Experiments: (a) 31-Year and 2-Year Spin-up, and (b) 31-Year and 1-Year Spin-up

	Flux	HL	RR	Crop
Fluxes with One Year Spin-up	ET	0.00037	0.00148	0.02344
	GH	0.81295	0.66002	2.73476
	SH	0.47648	1.01852	11.72898
	LH	0.26051	1.03164	16.28484
	R_n	0.16467	0.18320	2.19841
Fluxes with Two Year Spin-up	ET	0.00032	0.00034	0.00255
	GH	0.61713	0.70746	0.87317
	SH	0.30689	0.51341	0.89491
	LH	0.22776	0.23582	1.77327
	R_n	0.10814	0.07830	0.23395
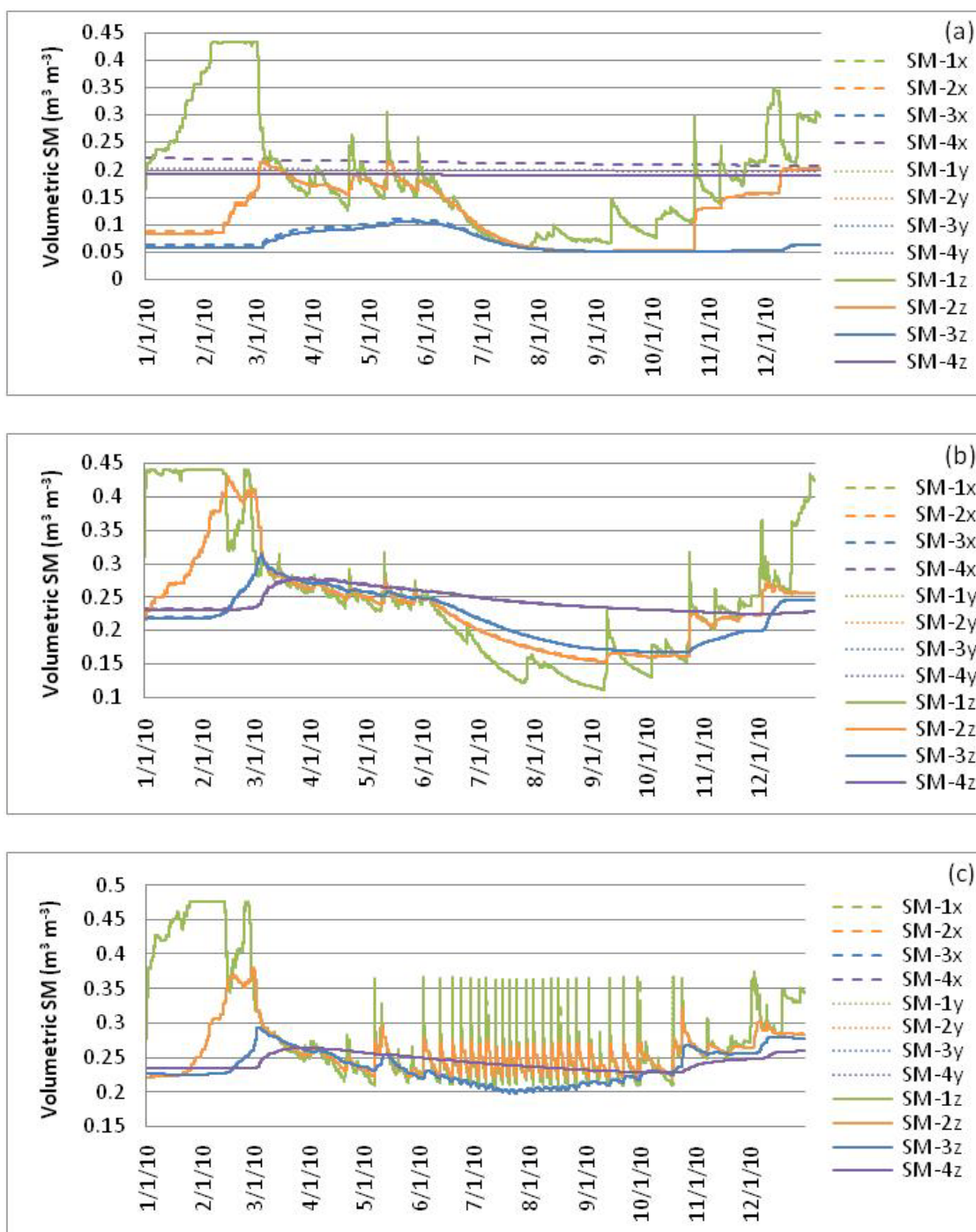
Figure 4.9. Soil Moisture (SM) Content at Four Soil Layers with Different Spin-up Times at (a) Raft River, (b) Hollister, and (c) Irrigated Cropland Cell. In the legend, 'x' Is with 1-Year Spin-up, 'y' Is with 2-Year Spin-up, and 'z' Is with 30-Year Spin-up

state than soil moisture with 1-year spin-up. It was more visible for the RR site. The

RMSE of surface fluxes between data with 31-year and 2-year spin-up and between data

with 31-year and 1-year spin-up were computed. Table 4.2 shows the error was reduced

with 2-year spin-up data except for GH at RR site. This reduction in error was significant

for crop cells compared to the other two locations. Based on these results, 2-year spin-up

time was applied for all the model runs here.

4.5 Irrigation in the Model

Being identified as a critical process during the growing season over agricultural

lands, irrigation water was added to replenish soil moisture periodically to the first soil

layer (0 - 10cm). This was done throughout the growing season from April to October.

As an average over croplands, the total irrigation amount of water applied was

approximately 620 mm per year over the past 30 years (1981 - 2010). It varied with the

amount of total precipitation (Figure 4.10). As an example, the maximum amount of

irrigation, which was approximately 790 mm, was applied when the total annual

precipitation was minimum for the last 30 years. That was in 1992 when precipitation

was around 200 mm. However, the other way was not true. That is when the maximum

precipitation occurred in 1983, the applied irrigation was 540 mm which was not the

minimum. Analyzing the seasonal and monthly precipitation that year, it was seen that

most of the precipitation within that year occurred during November (80 mm), which was

after the growing season. Therefore, even with maximum precipitation, the amount of

irrigation was not reduced as expected. Irrigation usually peaked in July and August with
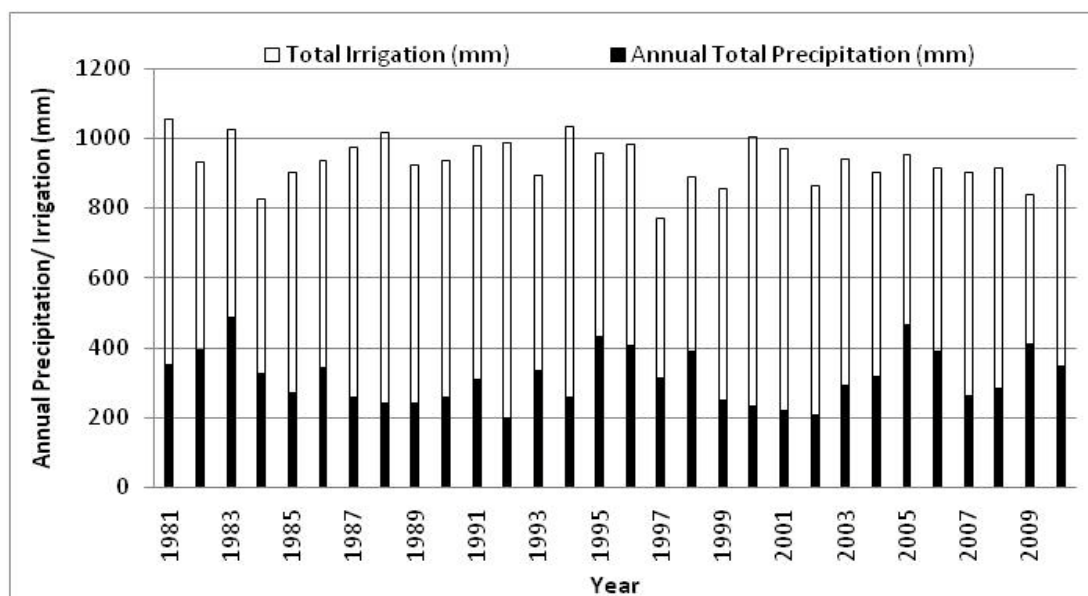
Figure 4.10. Noah LSM Irrigation and Precipitation as an Average for Croplands for the Last 30 Years (1981-2010)

the maximum number of events. The maximum irrigation amount was applied in 1992 in the year the maximum irrigation was recorded. Minimum irrigation was 430 mm in 2009 where precipitation was 410 mm.

4.6 Effects of Irrigation

4.6.1 Effects on Surface Temperature and Soil Moisture

Irrigation affects many land-surface processes in many ways. Figure 4.11 shows the variation of soil moisture at four soil layers with and without irrigation for a cell classified as cropland. As stated in early sections, soil layer thicknesses in the order from the land surface are 10 cm, 30 cm, 60 cm, and 100 cm. In the absence of irrigation, soil moisture decreased rapidly during the growing season and became minimum during the
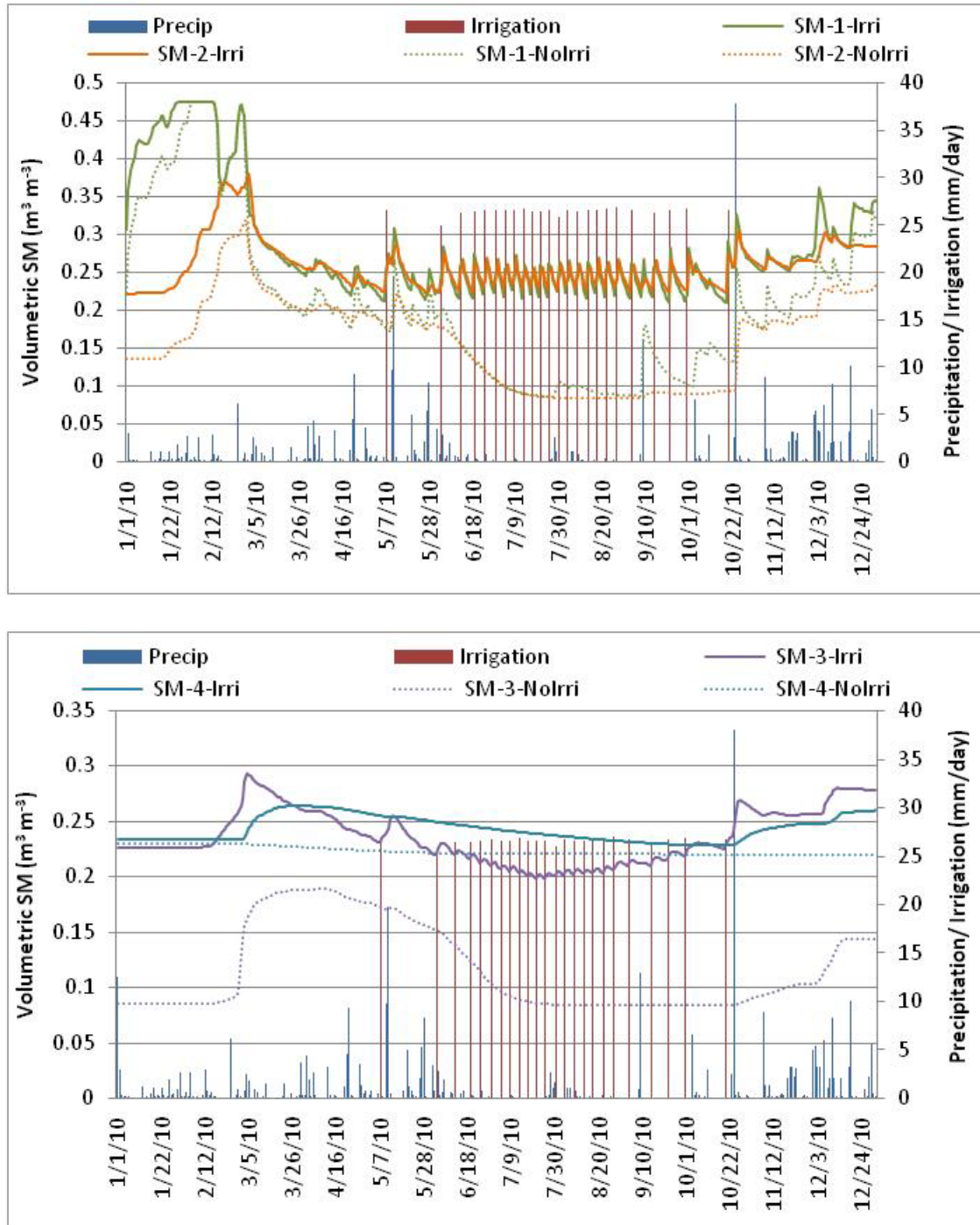
Figure 4.11. Variation of Soil Moisture (SM) at Four Soil Layers (SM-1, SM-2, SM-3 and SM-4) with (Irri) and without (NoIrri) Irrigation. Precipitation and Irrigation Are also Given

peak growing months (July and August). Irrigation affected the soil moisture more in the first three soil layers than in the fourth soil layer. During July, the soil moisture content in the first layer was increased roughly by 0.15 m^3 m^{-3}. In order to examine its spatial effect on the variables, the spatial plots were made comparing the irrigated model runs with non-irrigated model runs and the differences (irrigated – non-irrigated; I-NI) were plotted. Figure 4.12 shows the differences in surface (skin) temperature (first column) and soil moisture (second column) at the first soil layer. The positive values over the irrigated areas in the first column indicate that the irrigation has cooled the surface temperature over the cropland in the area. Increased moisture on the surface favored the LH and thus cooled the surface. During July and August in 2010, irrigation has caused the maximum cooling effect. As an average over croplands, irrigation reduced surface temperature by 3.6 ºK in July and this reduction in April was 0.5 ºK. There was a reduction of about 1.8 ºK in skin temperature averaging over croplands during the growing season. There were no changes over other land-cover types because of the absence of feedbacks from the uncoupled Noah LSM to the atmosphere.

Soil moisture was directly affected by the added irrigation as it was applied as an increment in soil moisture. The volumetric soil moisture of the first soil layer (1-10 cm) was increased by 0.09 m^3 m^{-3} and the increase in the second layer (10- 40 cm) was 0.11 m^3 m^{-3}. The increment was higher in the second layer than the first layer even though the irrigation was applied to the first soil layer. The possible reason can be the quick drying of the first soil layer through direct evaporation (which happened only through this layer) so that the water does not retain longer in that layer. Water is removed from the second
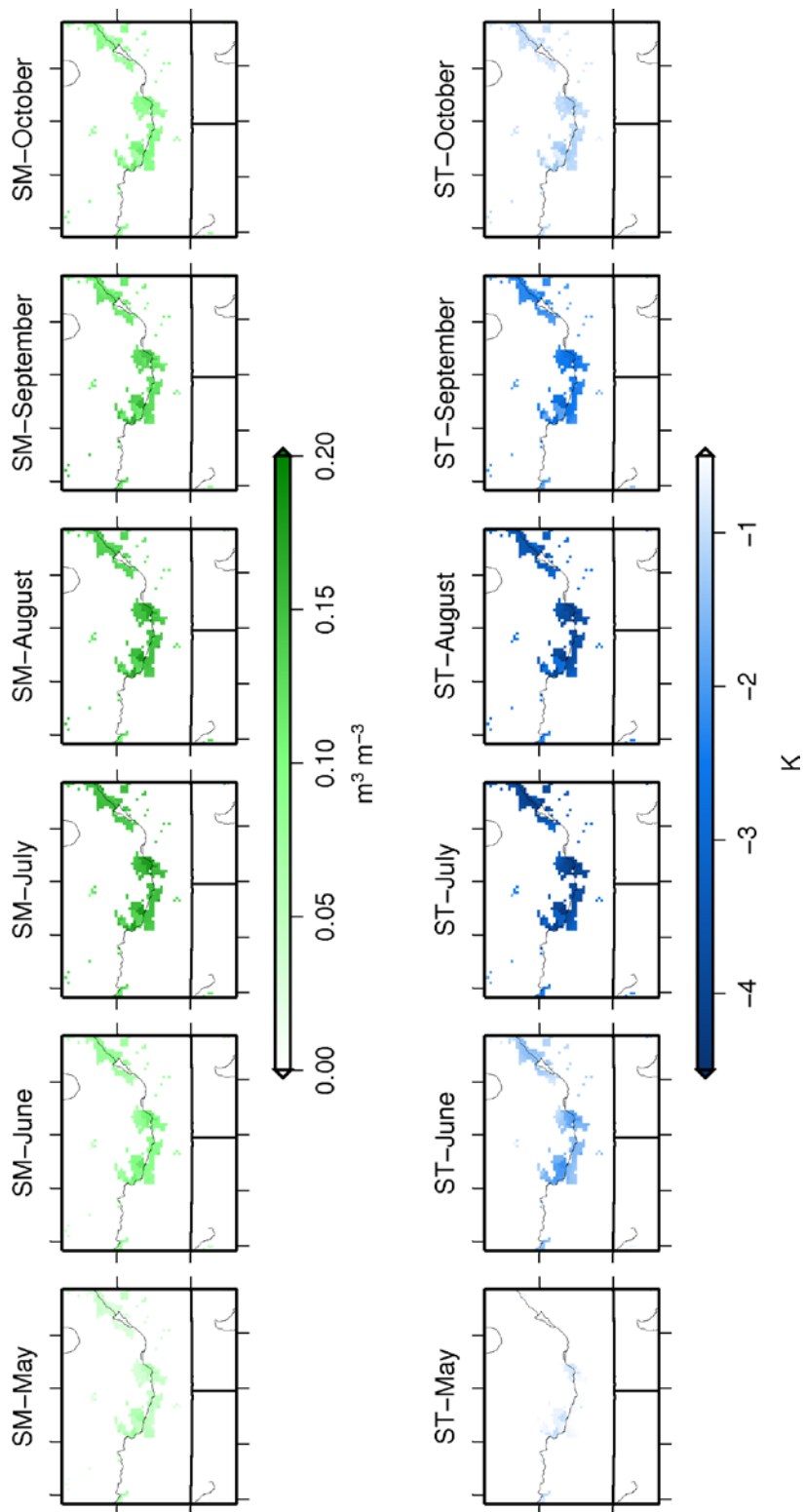
Figure 4.12. Effects of Irrigation on Skin Temperature (ST) and Soil Moisture (SM). The Values Were Obtained by Subtracting ET without Irrigation (NI) from ET with Irrigation (I): (I Minus NI)

soil layer only through transpiration from the root zone and through percolating to the third soil layer. The bottom layer had the least effect, which showed a difference of only 0.018 m^3 m^{-3}. All the values are averages for the whole growing season over irrigated lands.

4.6.2 Effects on the Surface Fluxes

The surface energy balance is affected by irrigation through soil moisture. Increased soil moisture by irrigation changes the energy partitioning between LH and SH. Figure 4.13 illustrates the changes in surface fluxes with applied irrigation. Surface fluxes are mean hourly, averaged over each month. The effects were limited only to the irrigated areas since the irrigation induced changes happened only over croplands and there were no feedbacks provided to the atmosphere from the uncoupled LSM. The addition of irrigation water has increased LH over agricultural areas, which led to an increase in ET. Conversely, SH was reduced over the same area. As an example, in July, LH was increased by 11 W m^{-2} and SH was decreased by 10 W m^{-2} averaged for the region. Changes in R_n and GH were minimal, which were a 1.6 W m^{-2} increase and a 0.15 W m^{-2} increase, respectively. The R_n change can be explained in two ways, with surface cooling and increased near-surface humidity (Cook et al., 2010). Irrigation has cooled the surface with increased ET, which possibly caused a reduction in outgoing longwave radiation. Increased humidity resulting from increased ET creates more downward longwave radiation. Due to these situations, net longwave radiation increases resulted in a simultaneous increase in net radiation. Ground heat flux showed very small variations
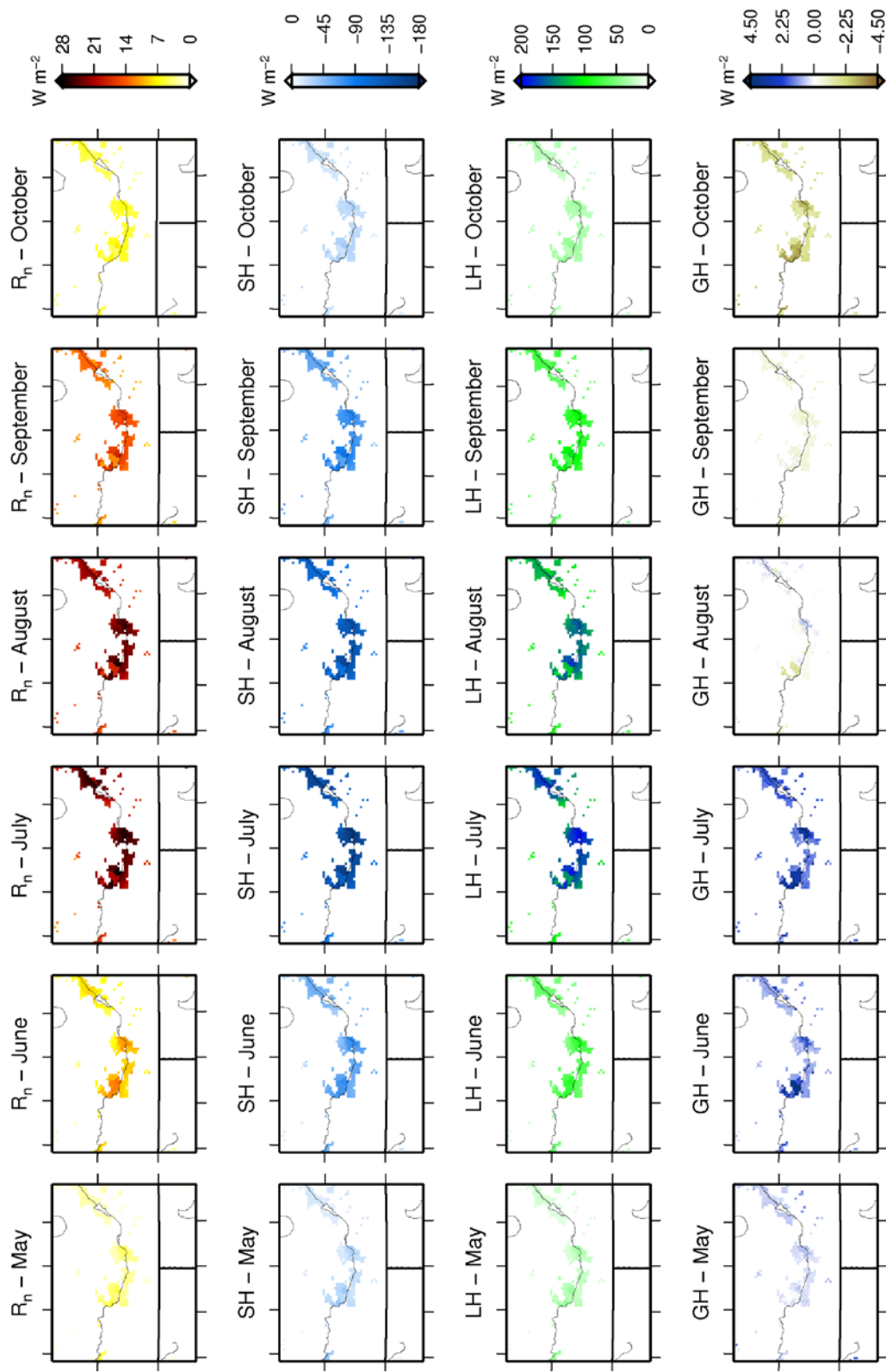
Figure 4.13. Irrigation Effects on Surface Fluxes. The Values Were Obtained by Subtracting ET without Irrigation (NI) from ET with Irrigation (I): (I Minus NI)

due to the cooled surface. Ground heat flux has increased up to July and from August it has been decreased. The effects were high during peak growing months in this area, like in July and August, when intensive irrigation took place. Ozdogan et al. (2010) also showed the effects were significant mostly during July and August when considering the entire United States. Results showed that the number of irrigation events was maximum during July or August.

Taking the average change over the irrigated cropland during the growing season (April-October), LH was increased by 72 W m^{-2} (193%), SH was decreased by 62 W m^{-2} (91%), ground heat was increased by 0.34 W m^{-2} (16%), and net radiation was increased by 11 W m^{-2} (10%) in 2010.

4.6.3 Effects on Evapotranspiration

There was a significant increment of ET caused by the added irrigation scheme. Figure 4.14 shows the increment (I- NI) of monthly total ET in the months during the growing season. Peak ET increment occurred during July as other variables discussed above. The average increment over croplands was 169 mm in July. Throughout the whole irrigation period in 2010, ET was increased by 540 mm. Added soil moisture due to irrigation within that year was 580 mm. Most of the water applied through irrigation has been converted to ET. Ozdogan et al. (2010) showed that in some parts of United States, ET was increased at least by 100% with irrigation. Even though the maximum increment was visible in July, as a percentage increase, August had the maximum percentage of increase in ET.

May

June

July

August

September

October

0   50   100   150   200

mm
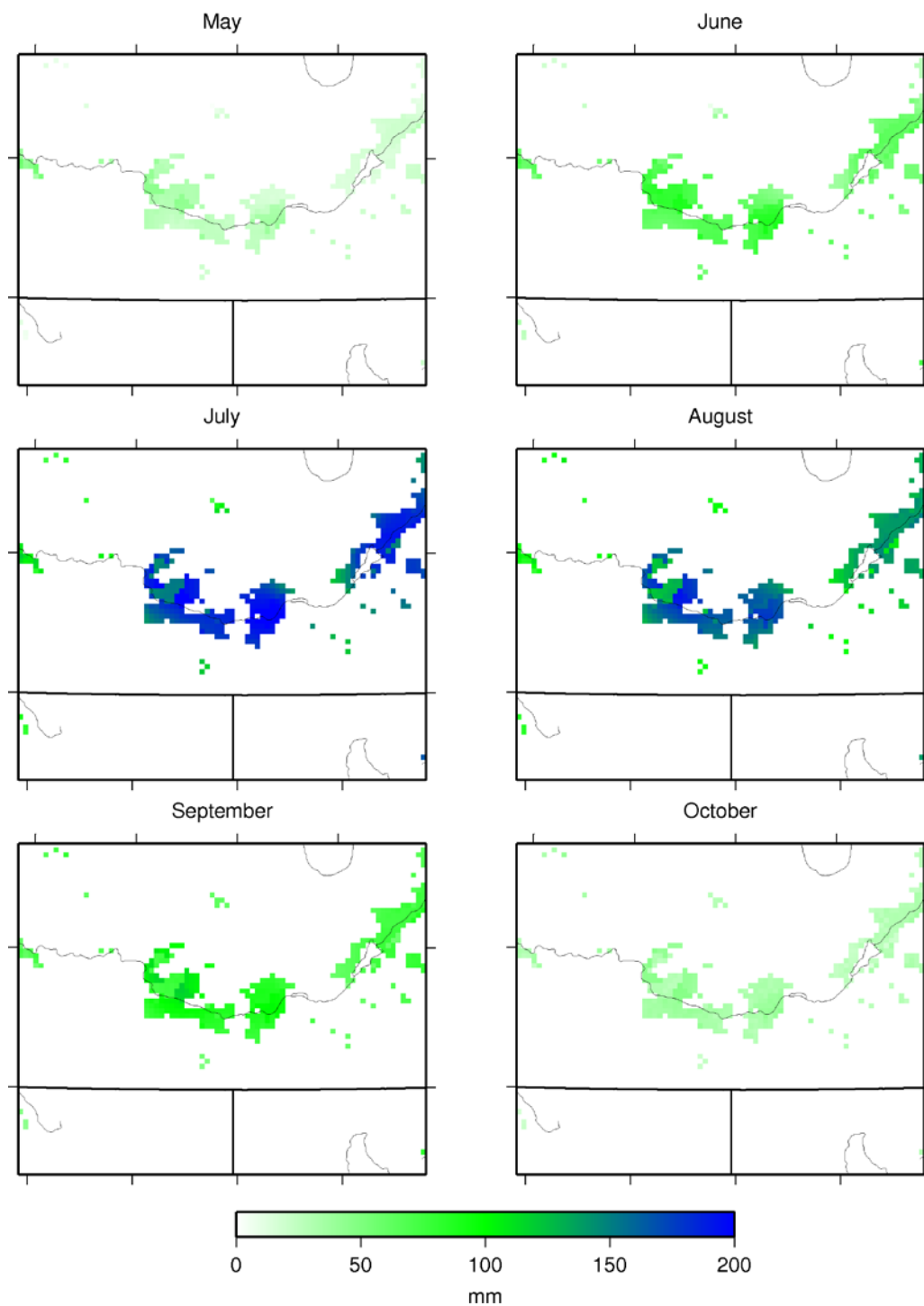
Figure 4.14. Differences in Monthly Total ET in Millimeters. The Values Were Obtained by Subtracting ET without Irrigation (NI) from ET with Irrigation (I): (I Minus NI)

4.7 Long-Term Trends

4.7.1 Annual Trends of Evapotranspiration

Annual total values of ET were plotted for trend evaluation for three land-cover types, grassland, shrubland, and cropland. Monthly total ET indicates that two natural vegetations sites, HL and RR, have increasing trends with gradients of 0.0004 and 0.0002. To explain the monthly variations in ET, precipitation and surface fluxes were studied. It showed that the ET was more correlated with precipitation than with available energy. ET changed with the changes in precipitation while the variations in available energy were negligible. Cropland site did not show much correlation with annual precipitation. However, over the last thirty years, there was a decreasing trend at the crop
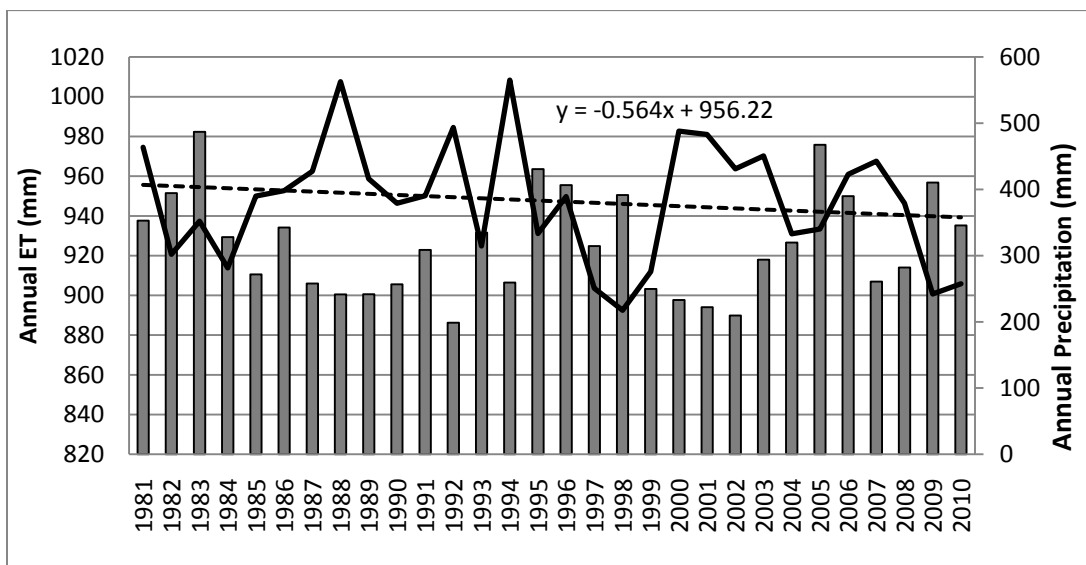
Figure 4.15. Annual Total ET and Precipitation in Croplands for the Past 30-Year Period from 1981- 2010. Annual Precipitation Is Shown by Gray Bars, Annual ET Is Shown by the Solid Black Line, and the Dotted Black Line Is the Trend Line for Annual ET. Equation for the Trend Line Is Mentioned in the Figure.
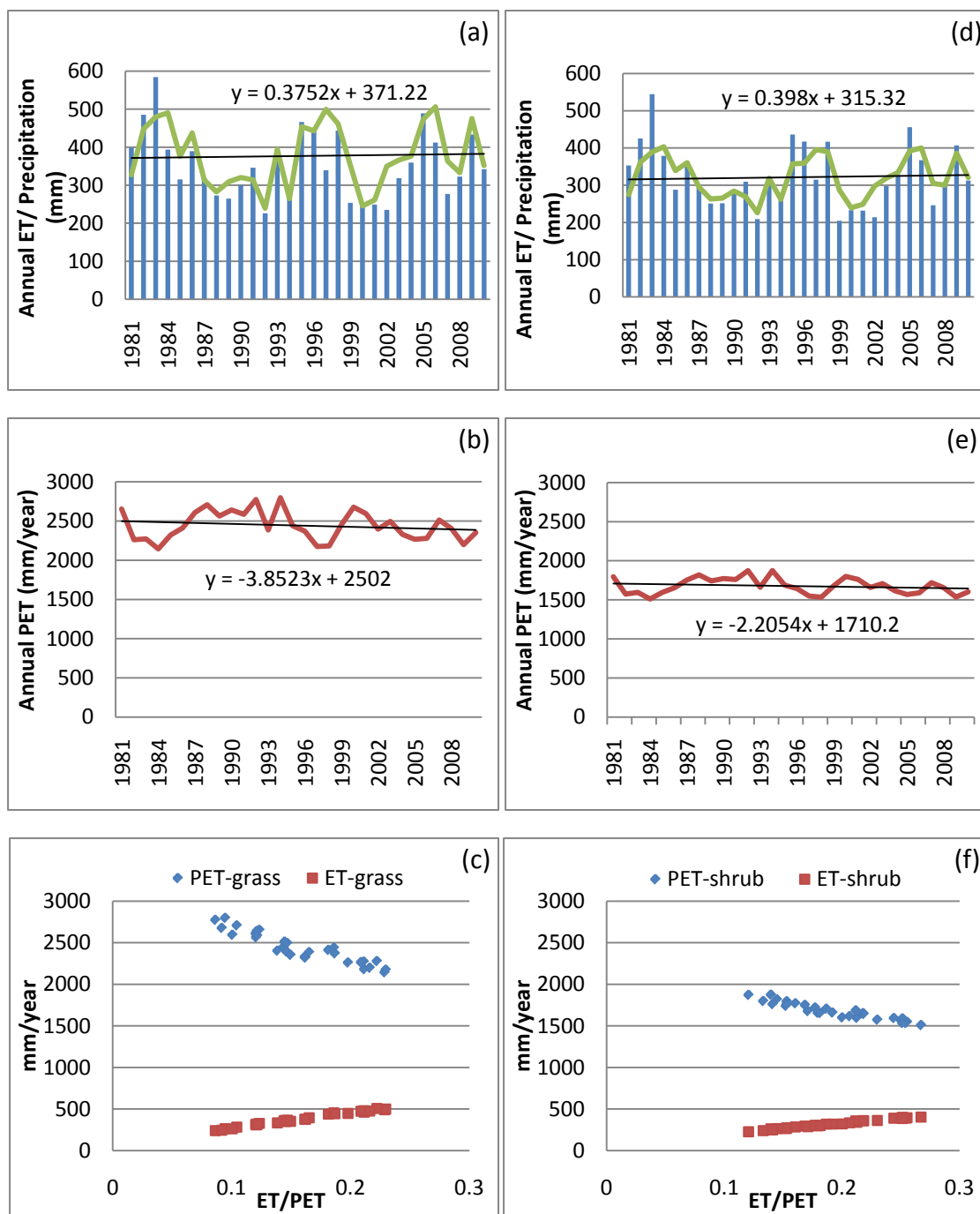
Figure 4.16. Annual Trends of ET (AET) and PET and CR for the 30-Year Period from 1981- 2010 for Two Natural Vegetations: (a) Actual ET from Grasslands, (b) Potential ET from Grasslands, (c) CR for Grasslands, (d) Actual ET from Shrublands, (e) Potential ET from Shrublands, and (f) CR for Shrublands. Annual Precipitation Is Shown by Blue Bars in (a) and (d).

site. Data were averaged over three land-cover types, croplands, shrublands, and grasslands, and the annual total ET trends were as same as monthly trends for the main three land-cover types. Table 4.3 shows the long minimum, maximum, and mean of monthly total ET, and Figure 4.15 shows the annual trend of ET for croplands.

Within croplands, ET was not correlated with precipitation because the main source of moisture input for this area was received through irrigation. Therefore, annual trends of only natural vegetation were further analyzed. It was observed that annual PET averaged for both natural vegetations had a decreasing trend. This agrees with the findings of decreasing pan evaporation in this area (Lawrimore and Peterson, 2000; Peterson et al., 1995). Figure 4.16 shows annual ET, PET trends, and the CR between annual ET and PET for the past 30 years for shrublands and grasslands. Past studies have shown that the diurnal temperature range (DTR) has more effect on decreasing pan evaporation (Roderick and Farquhar, 2002; Peterson et al., 1995). Daily minimum and maximum temperature, as well as DTR, were analyzed to see if they explained the decreasing trends in PET. It was observed that the DTR has decreasing trends for both shrublands and grasslands (Figure 4.17). Both annual minimum and maximum temperature showed increasing trends (with slopes of 0.04 for maximum temperature and 0.08 for minimum temperature). However, the rate of increase in minimum temperature was higher than the rate of increase in the maximum temperature by roughly a factor of 2. This caused reduction in DTR. This is in agreement with the findings of Easterling et al. (1997).

Table 4.3. Long-Term Monthly Minimum, Maximum, and Mean ET (in mm) for Croplands, Grasslands, and Shrublands

	Croplands	Grasslands	Shrublands
Minimum	5.29 mm	2.00 mm	4.23 mm
Maximum	217.86 mm	99.36 mm	77.11 mm
Mean	78.96 mm	31.42 mm	26.79 mm
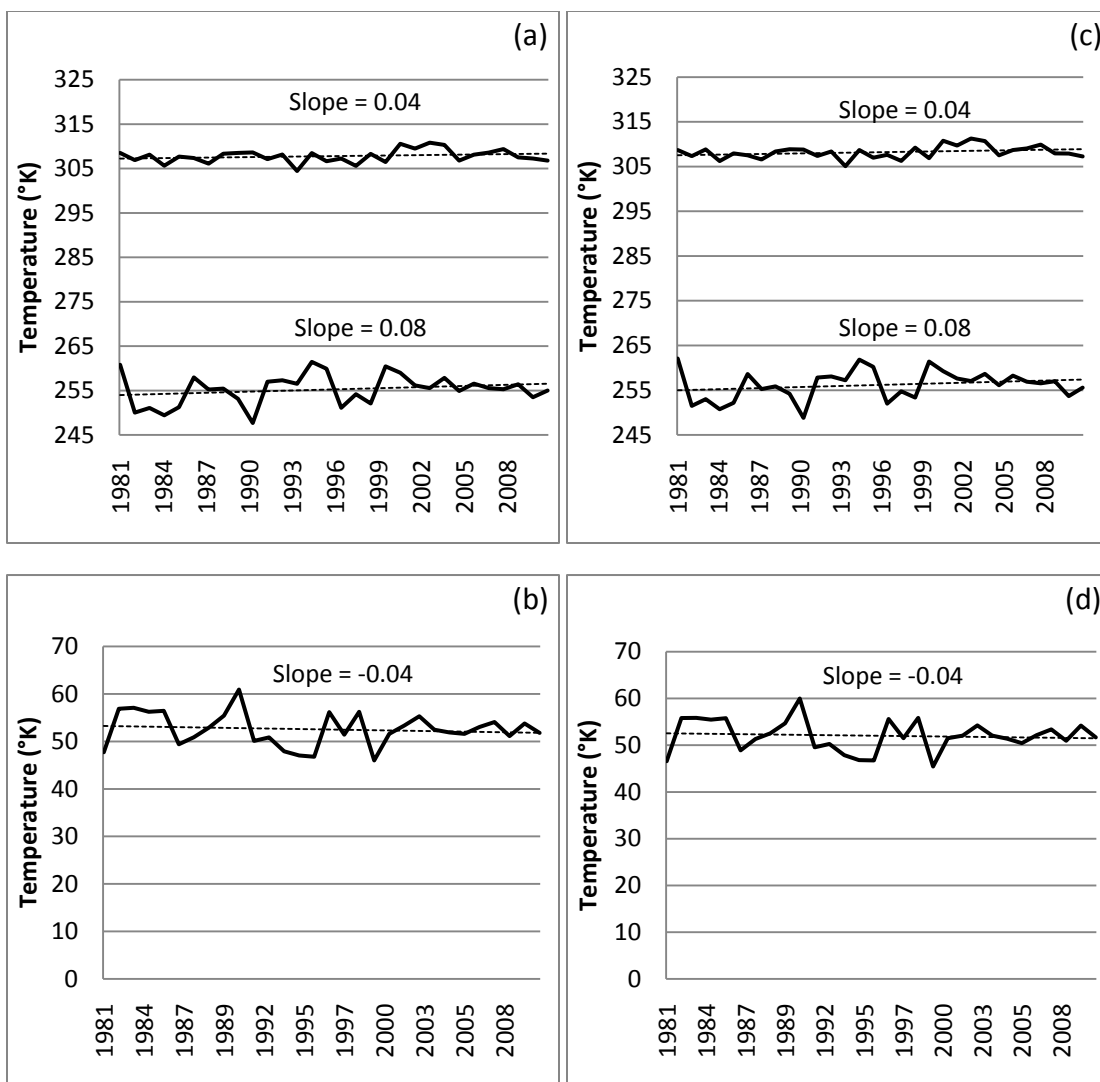
Figure 4.17. Annual Minimum and Maximum Temperature (a and c) and Diurnal Temperature Ranges (b and d) for Grasslands (a and b) and Shrublands (c and d).

4.7.2 Seasonal Trends of Evapotranspiration

      Seasonal trends were analyzed for the three locations as well as for the area averaged values. Spring showed increasing ET for all three vegetations with high gradients for shrublands (0.45) and grasslands (0.53). Winter time ET also showed a slight increasing trend. During the summer, croplands and grasslands indicated decreasing patterns while shrubland ET showed an increasing trend. Croplands showed the least variations in the summer. This is again a result of irrigation applied, which maintains the water requirement of the vegetation during the summer. All three vegetation showed decreasing ET in fall over the past thirty years.

4.7.3 Long-Term Energy Balance Climatology

      Long-term monthly average fluxes were studied for the three main land-cover types by taking the spatial average values. Figures 4.18, 4.19, and 4.20 show the monthly mean fluxes for 12 months. The error bars are one standard deviation. The figures indicate that the errors were higher during the summer for all four fluxes. During the other seasons except summer, R_n was very small and soil moisture was not limiting LH. Therefore, the energy portioning was approximately similar for all land-cover types and the error was small. SH and LH showed higher errors with ranges $2.5 – 15.8$ W m^{-2} and $2.5 – 17.8$ W m^{-2} compared to GH ($0.9 – 4.2$ W m^{-2}) and R_n ($3.2 – 8.8$ W m^{-2}). Over croplands, during the peak growing month, July, LH has exceeded R_n. To compensate this deficit, SH has been reduced to even below zero.
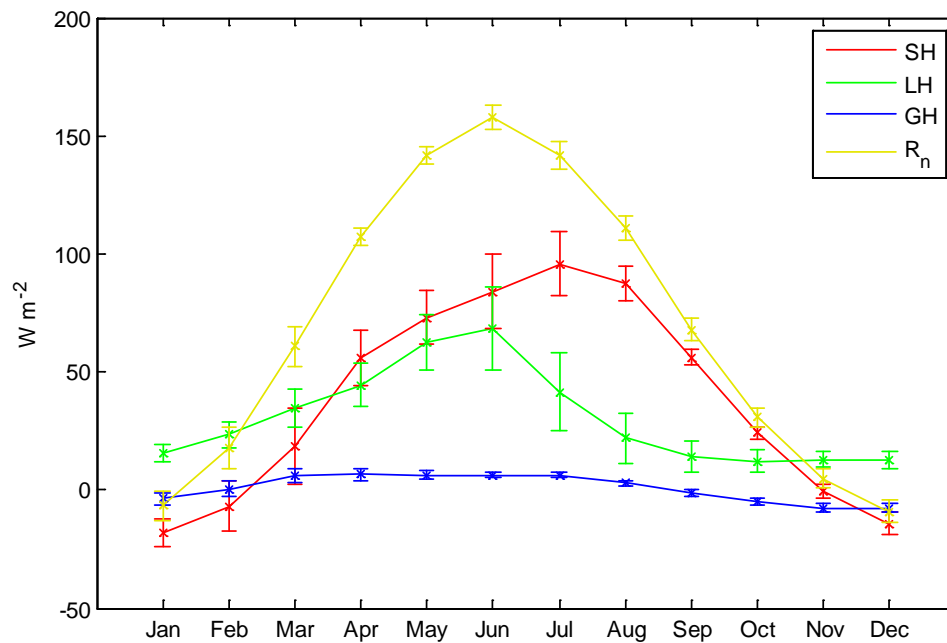
Figure 4.18. Thirty-Year Averages of Monthly Mean Surface Fluxes for Grasslands. The Error Bars Indicate One Standard Deviation.
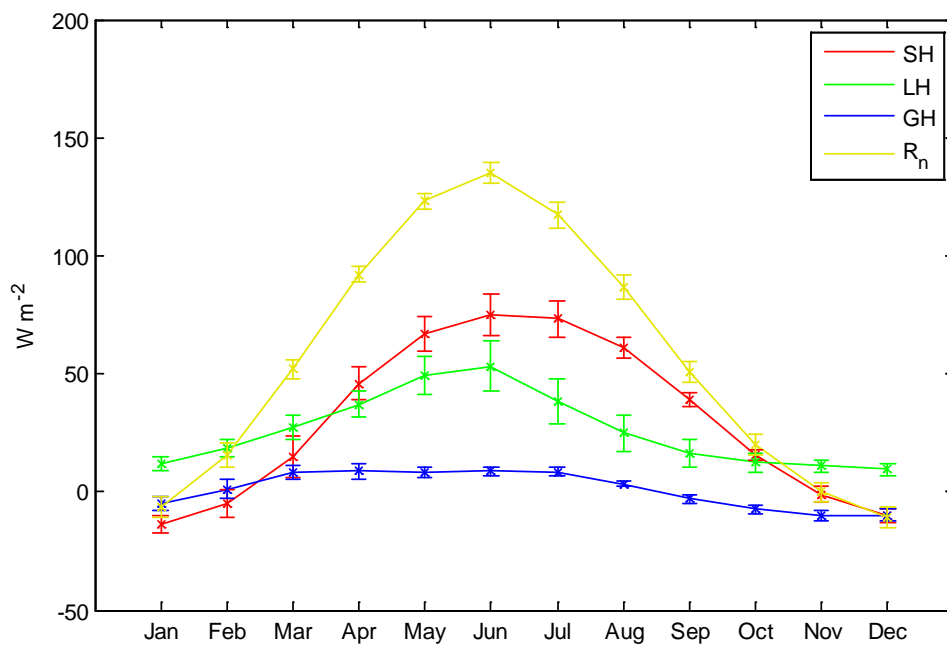
Figure 4.19. Thirty-Year Averages of Monthly Mean Surface Fluxes for Shrublands. The Error Bars Indicate One Standard Deviation.
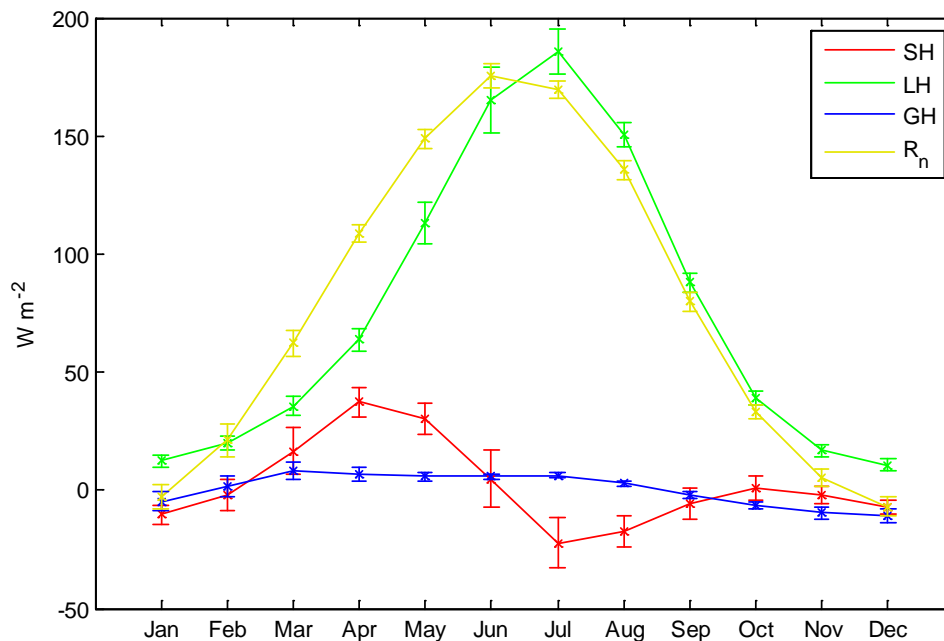
Figure 4.20. Thirty-Year Averages of Monthly Mean Surface Fluxes for Croplands. The Error Bars Indicate One Standard Deviation.

4.8 Conclusions on Irrigation Effects and Long-Term Climatology

This section presents the results from the validation effort of Noah LSM, impacts of irrigation, and long-term climatology of ET and surface fluxes. Model forcing variables, temperature, and precipitation from NARR were evaluated against the field observations to see if there were any errors/ bias. It was observed from the analysis that NARR showed a warm bias for both natural vegetation and irrigated croplands. The bias and RMSE was higher for croplands than the natural vegetation. In the generation of NARR, all the lands in this region were categorized as natural vegetation. The absence of irrigated croplands in the area reduced ET, thus decreased humidity and increased the temperature. Therefore, when these data were compared with field observations, which

have the irrigation effects, the error was larger than that from the natural vegetation. Precipitation was lower from the NARR compared at both natural vegetation sites.

Before the model results were validated with the field observation at HL and RR, the energy balance closure was checked in the measured surface fluxes. An energy budget closure problem in field observations is common, which have been reported from several other studies (Wilson et al., 2002; Foken, 2008; Maayar et al., 2008; Lei and Yang, 2010). As observed in those studies, energy budget was not closed at both sites and showed that SH and/or LH was underestimated. Validation results showed that SH was significantly overestimated at RR. A comparison with METRIC ET maps showed that the Noah LSM with the added irrigation was able to capture the variation of ET spatially and temporally.

During the growing season, irrigation has a significant effect in semiarid agricultural regions. In order to incorporate this fact in Noah LSM, an irrigation scheme was added, which supplied enough moisture source to the crops. Average irrigation water added during the whole growing season for the past 30 years was 620 mm. This changed the surface energy budget mainly by increasing LH and decreasing SH. R_n increased slightly and GH was least affected. In 2010, total ET during the growing season was increased by 540 mm. As a result of this added water, soil moisture was increased and surface cooling was observed, which agreed with Cook et al. (2010). Agreement of Noah ET with METRIC ET emphasized the need and importance of irrigation in agricultural lands.

The long-term trends of ET showed that two main natural vegetations, grasslands and shrublands, had an increasing trend of ET while croplands showed decreasing trends. However, in natural vegetation regions, ET was more related with annual precipitation, where in croplands main moisture input was from irrigation and ET did not depend on the precipitation. Contradicting to the actual ET trends at natural vegetation, PET showed decreasing trends. This was also observed with pan evaporation in this region (Lawrimore and Peterson, 2000; Peterson et al., 1995). As Roderick and Farquhar (2002) showed, decreasing DTR observed in this area is a possible explanation for this decreasing PET. It was shown that ET and PET had a complementary behavior in natural vegetation lands in this region.

CHAPTER FIVE: RESULTS: COMPLEMENTARY RELATIONSHIP

This is a relatively simple method to estimate ET. Since the study domain is mainly comprised of natural vegetations, it was tested if CR can be used to estimate ET from natural vegetation in South Central Idaho with only modeled forcing from NARR and Noah Land Surface Model-simulated flux and ET for the years 2005 and 2010. A well-formulated, physically-based ET estimation technique that is less dependent on ground data will fill the critical gap in the energy balance partitioning studies. This technique was not able to apply for irrigated croplands in this study since those lands were modified by applying irrigation. Since the Noah LSM was run in uncoupled mode, effects of this applied irrigation were not fed back into the atmosphere. Therefore, NARR forcing data and Noah simulated ET were not in a complementary relationship for croplands. Deriving CR for natural vegetation in the area will enable us to understand the feedbacks under the changing climate by studying the variation of ET with predicted warming conditions in the 21st century. Under global warming conditions, long-term measurements have shown that diurnal temperature trends have been decreasing due to the faster increasing rate of minimum temperature compared to the rate of increase in maximum temperature (Easterling et al., 1997). Therefore, proper water management would be essential in this area in which quantification of evapotranspiration is critical.

5.1 Data Preparation for the AA Model

Simulated actual ET_{Noah} was obtained from Noah LSM for 2010 in order to

examine the CR over the two vegetation types. PET was calculated using the Penman

(1948) approach, the NARR weather data, and the Noah LSM output, which includes net

radiation (R_n) and ground heat flux (GH). Minimum, maximum, and mean temperature

and wind speed were obtained from NARR. Actual vapor pressure was calculated from

specific humidity and pressure from NARR data and the calculated vapor pressure and

temperature data were used in saturation vapor pressure calculations. This method was

preferred over the Penman-Monteith (Monteith, 1973) equation because of the absence of

aerodynamic resistance terms, which requires additional information for vegetation and

that can make the computations complex. PET is also computed within Noah LSM.

However, Noah-predicted PET appeared to overestimate when compared with PET

values from other sources such as the Variable Infiltration Capacity (VIC) model and

PET from AgriMet weather stations located in the area. Therefore, instead of using Noah

PET, it was separately calculated by the Penman (1948) method.

$$PET = \frac{\Delta Q_n + \gamma E_a}{(\Delta + \gamma)} \tag{5.1}$$

where Q_n is the available energy (R_n-GH), R_n is net radiation, GH is ground heat flux, Δ

is the slope of the saturation vapor pressure at air temperature, γ is the psychrometric

constant, and E_a is the drying power of air, which is given by

$$E_a = 0.26 \, (1 + \, 0.54 \, U)(e_s - \, e_a) \tag{5.2}$$

A normalization procedure was applied following Kahler and Brutsaert (2006) and Huntington et al. (2011) in order to get a universal relationship with a dimensionless formulation. This was achieved by dividing both ET_{Noah} and PET by ET_w. Priestley and Taylor (1972) introduced an equation to equilibrium ET under minimal advection. ET_w is considered as a constant independent of surface wetness while PET can be related with different surface wetnesses (Yang et al., 2006). This Priestly-Taylor equation which was used in other CR studies (Brutsaert and Stricker, 1979; Kahler and Brutsaert, 2006) to compute ET_w, was used here, which is given below.

$$ET_w = \frac{\propto \Delta Q_n}{(\Delta + \gamma)} \tag{5.3}$$

where α is the Priestly-Taylor coefficient, which is 1.26 for an advection free water surface. In Equation (5.3), Δ was evaluated at wet environment air temperature (T_e) following the method used by Szilagyi and Jozsa (2008) and Huntington et al. (2011). Huntington et al. (2011) showed that using wet environment temperature in calculating the ET_w resulted in symmetric CR. It was an iterative process that used air temperature and humidity to calculate wet environment air temperature using the Bowen ratio (B_0) for a small wet surface as follows.

$$B_0 = \frac{SH}{PET} = \frac{Q_n - PET}{PET} = \gamma\frac{T_{sw} - T_{aw}}{e_{sw} - e_{aw}} \approx \gamma\frac{T_e - T_a}{e^*(T_e) - e_a} \qquad (5.4)$$

where SH is the sensible heat flux, T_{sw} and T_{aw} are surface and air temperature of wet environment, e_{sw} and e_{aw} are vapor pressure at surface and air for the wet environment, and T_a and e_a are temperature and vapor pressure in a water-limited environment. In order to obtain a smooth trend, a 7-day moving average of daily ET_{Noah}, PET, and ET_w was computed centered at the 4th day. The dimensionless terms of ET_{Noah} and PET are

$$E_+ = ET_{Noah}/ET_w \qquad (5.5)$$

$$E_{P+} = PET/ET_w \qquad (5.6)$$

Equations (5.5) and (5.6) also can be written as a function E_{MI} ($E_{MI} = ET_{Noah}$ / PET) and the b factor in Equation (3.29) as follows, which satisfy the relationship as in (3.29). E_{MI} is an indication of the closeness of the landscape to potential conditions (Kahler and Brutsaert, 2006).

$$E_+ = \frac{(1 + b)E_{MI}}{1 + bE_{MI}} \qquad (5.7)$$

$$E_{p+} = \frac{1 + b}{1 + bE_{MI}} \qquad (5.8)$$

5.2 Complementary Relationship in Noah LSM and NARR Data

In this study, we analyzed the simulated results of ET_{Noah} to derive the CR for the period between March and September during 2010. Winter months were excluded from the analysis. During winter months, ET_{Noah} was higher than ET_w in some days making E_+ more than 1. Also, ET_w tends to take negative values representing the formation of dew while ET_{Noah}, output from Noah does not include dewfall. Huntington et al. (2011) showed that adding winter months to the analysis brings scatter in the plot and also causes deviations from the symmetry in CR. This happens mainly due to the low ET and relatively large PET, which increases the ET/PET ratio. Normalized terms of E_+ and E_{p+} were computed by Equations (5.5) and (5.6) using ET_{Noah}, PET from Equation (5.1), and ET_w from Equation (5.3). Figure 5.1 shows the non-normalized CR for the two locations selected for the period from March to November in 2010 (excluding winter months). Modeled ET_{Noah} shows a complementary behavior with the computed PET using NARR data and Noah LSM output for two natural vegetation sites even before normalizing. Even though there is some scatter in the plot, ET_{Noah} and PET behaves complementarily; that is, under high soil moisture conditions, ET_{Noah} increases and PET decreases converging around $1 - 2$ mm day^{-1}.

The normalized ET_{Noah} and PET in Figure 5.2 clearly show this relationship with less scatter. However, still after removing the winter period, E+ shows values higher than 1 for some days especially at the beginning of March and during October and November. In other words, the ratio of ET/ET_w should never be greater than 1. That indicates, for some days ET_{Noah} is higher than ET_w by an averaged amount of 0.22 mm day^{-1} for
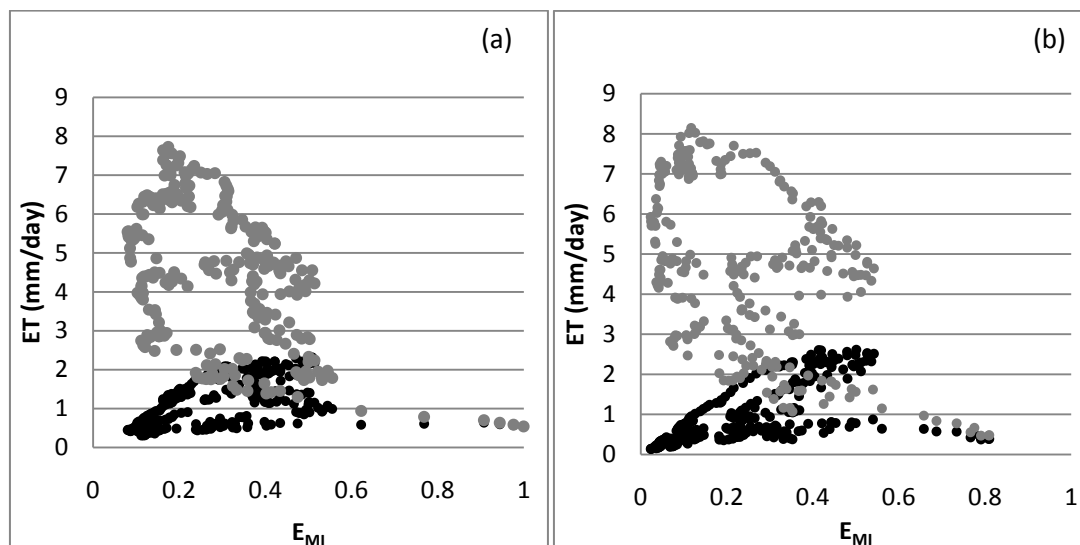
Figure 5.1. The Non-Normalized CR for the Two Selected Locations; (a) Sagebrush, and (b) Cheatgrass. Black Color Circles Indicate Daily Actual ET and Gray Color Circles Indicate Daily PET.

sagebrush and 0.13 mm/day for grassland. ET_w assumes there is no water limitation for evapotranspiration, while ET_{Noah} is subjected to both water and energy limitations, which should be always less than or equal to ET_w (i.e., $ET/ET_w \leq 1$). Time series of E_+, E_{p+} and E_{MI} (Figure 5.3) were analyzed along soil moisture conditions (Figure 5.4) to examine the possible cause. Figure 5.3 shows that E_+ started having unrealistic values (>1) at the end of October for both of the sites. E_{p+} is approximately stable around 2 untill the end of September when it started fluctuating. By studying the hydroclimatology of the region, the main variation during September and October could be attributed to the beginning of the wet season, which resulted in increased soil moisture conditions. According to Figure 5.4, soil moisture at the first layer (0 – 10 cm) starts to rise from 0.11 m^3 m^{-3} to 0.21 m^3 m^{-3} at the sagebrush site and 0.06 m^3 m^{-3} to 0.14 m^3 m^{-3} at the cheatgrass site following
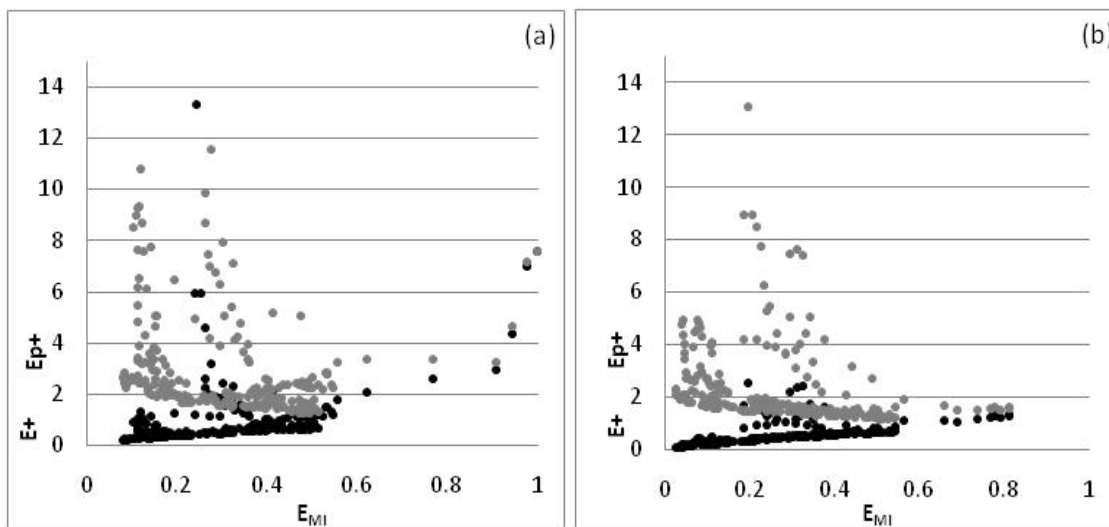
Figure 5.2. The Normalized CR for the Two Selected Locations: (a) Sagebrush, and (b) Cheatgrass. Black Color Circles Indicate Daily Actual ET and Gray Color Circles Indicate Daily PET. E_+ and E_{p+} Are Dimensionless Values

precipitation events in September. This increased soil moisture as simulated by the Noah LSM can cause rise in ET_{Noah} due to increased direct evaporation even though plants may not be transpiring much during this season. When compared against the ET_w, calculated by Priestly-Taylor equation, ET_{Noah} is higher for some days.

It seems like when the soil moisture is the limiting factor of ET, it was evident that the CR theory was holding good for these natural vegetation. On the other hand, when there is enough soil moisture (soil moisture is not the limiting factor for ET), CR appeared to have a loose correlation. However, this was not observed during the spring months (March – May) even though the soil was sufficiently wet with approximate soil moisture contents at the first layer of 0.26 m³ m⁻³ for sagebrush and 0.2 m³ m⁻³ for cheatgrass. Therefore, for further analysis and the derivation of CR for the two sites,
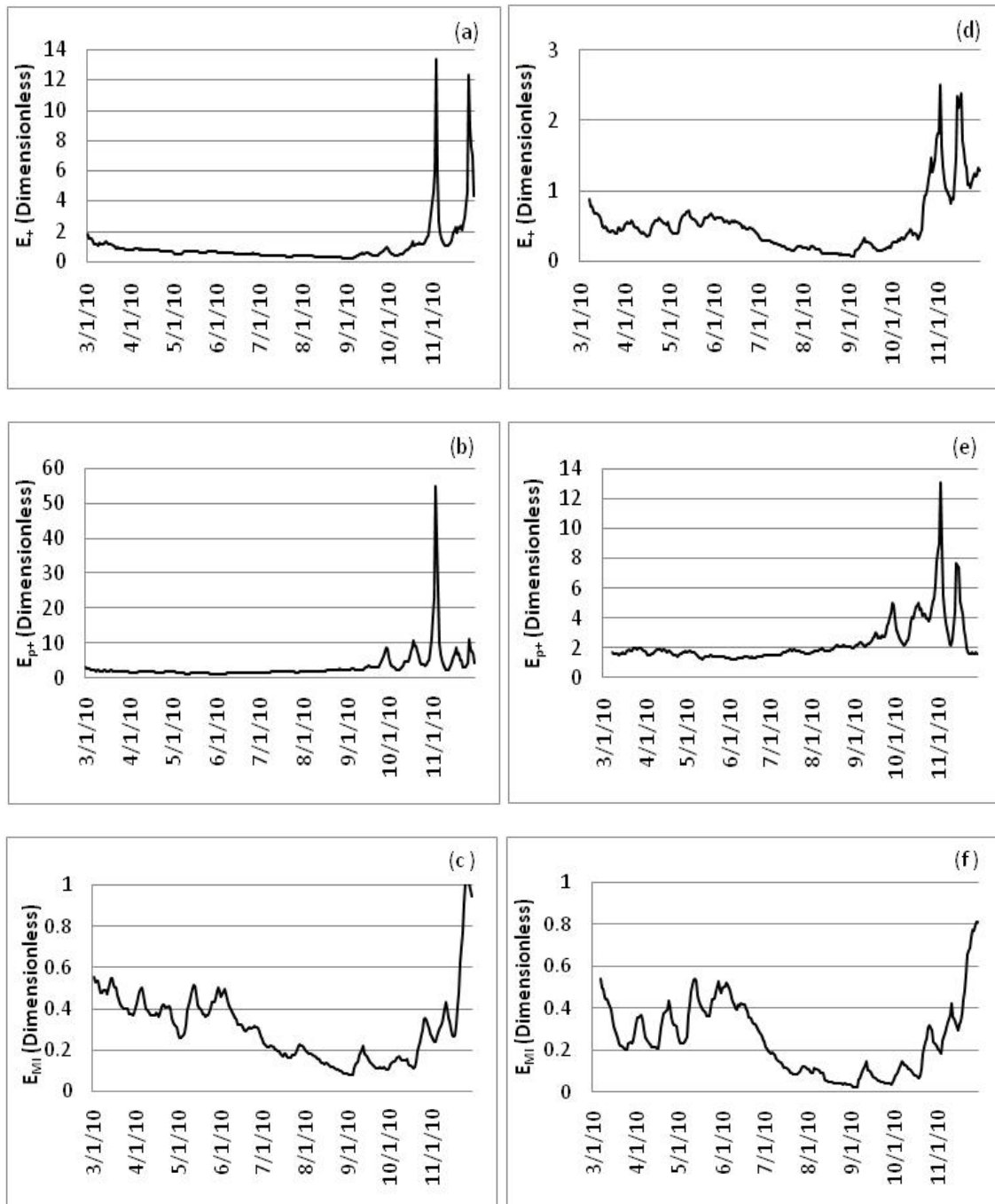
Figure 5.3. Time Series of E₊, E_{p+}, and E_{MI} for Two Sites, Sagebrush (a,b,c) and Cheatgrass (d,e,f), for 2010
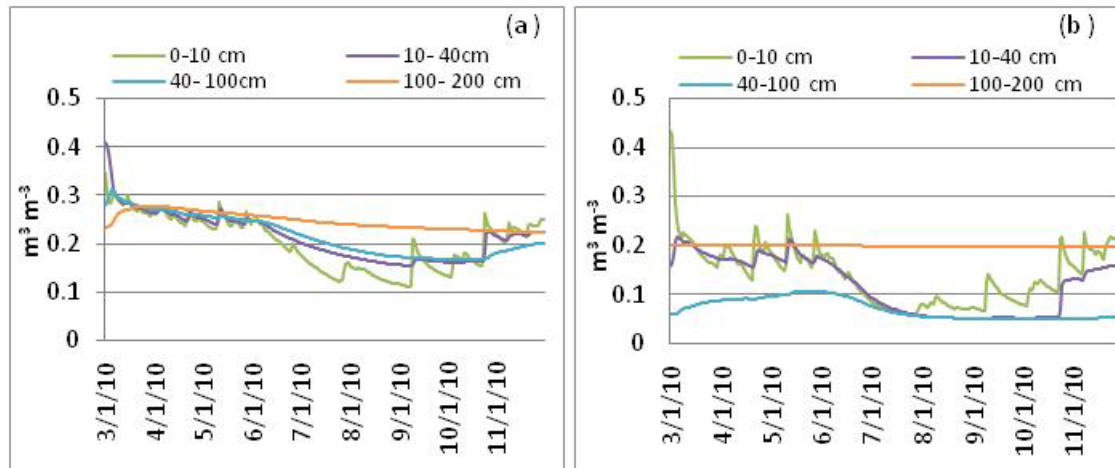
Figure 5.4. Soil Moisture at Four Soil Layers for the Two Sites, (a) Sagebrush and (b) Cheatgrass, Obtained from Noah LSM Output

periods or days when ET_{Noah} was higher than ET_w were not used. The period of 1 March-15 September in 2010 was chosen for further analysis.

5.3 Estimation of CR for Sagebrush and Cheatgrass

In order to find the proportionality constant, b in Equation (3.29), which determines the shape of the CR, normalized ET_{Noah} and PET was used. ET_{Noah} was obtained from Noah LSM and PET was computed using Penman (1948) with NARR weather data and Noah LSM output. E_+ and E_{p+} was also calculated by applying Equation (5.7) and Equation (5.8), which was independent of ET_w. The value of b was found by minimizing the sum of the squared error between the E_+ and E_{p+} calculated by the two methods. It was found that b is 1.933 for the sagebrush site and it is 1.08 for the cheatgrass site by using the wet environment temperature for ET_w for both sites (Figure 5.5). Huntington et al. (2011) obtained a symmetric CR with b=1.008 for phreatophyte
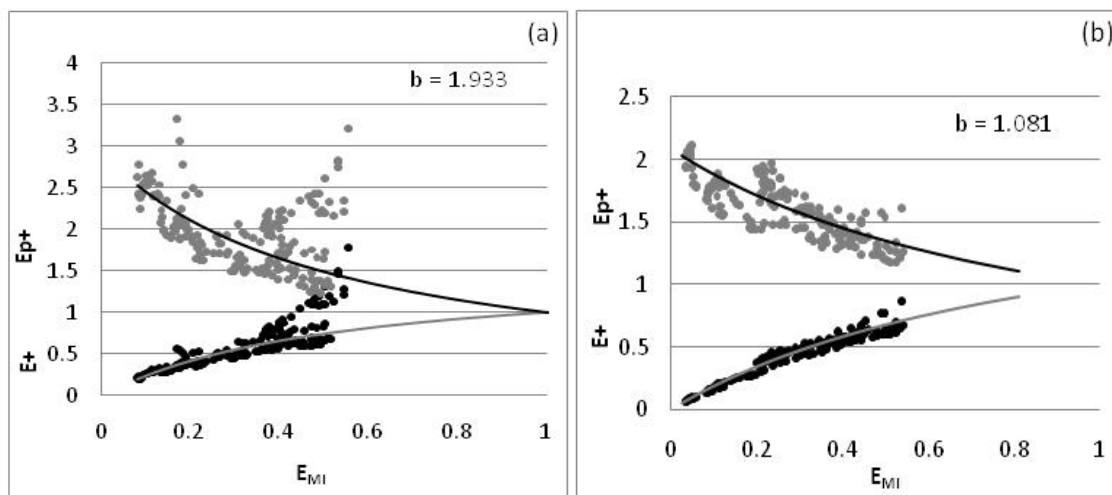
Figure 5.5. Normalized CR Curves and the Optimized Theoretical CR Curves for (a) Sagebrush and (b) Cheatgrass

shrub species in eastern Nevada. However, in this study, CR was not symmetric for the sagebrush site. The difference between b values can be due to the difference in vegetation and also variations in local climatology. Szilagyi (2007) explained that asymmetry in CR occurs in drying environments with increasing surface and air temperatures. In that situation, more energy than available energy, Q_n, is used for PET. The theoretical CR curves achieved convergence when E_{MI} reaches to 1 (unity) at the sagebrush site, but not at the cheatgrass site. According to Figure 5.3, (c) and (f) E_{MI} is close to 1 (unity) over the sagebrush site at the end of November. For the cheatgrass site, maximum E_{MI} is roughly 0.8. The ET_{Noah} at the cheatgrass site is lower when compared with the PET as expected. For the sagebrush site, ET_{Noah} is close to PET at the end of November when the soil is wet, thereby bringing the E_{MI} close to 1 (unity). The derived CR in this study for two sites can be written as

$$(1 + 1.933)ET_w = PET + 1.933 \times ET_{Noah} \tag{5.9}$$

$$(1 + 1.081)ET_w = PET + 1.081 \times ET_{Noah} \tag{5.10}$$

Equation (5.9) is for the sagebrush site and Equation (5.10) is for the cheatgrass site.

5.4 Validation of Complementary Relationship

Based on the CR, the computation of actual ET for a given location is relatively effective as opposed to other methods available to estimate ET. As stated before, it requires only the meteorological measurements in computing ET. As a sort of validation, it is important to check the applicability of CR derived for one time period to other periods. Several studies have evaluated the application of CR to assess the accuracy of estimates either using eddy covariance data (Yan and Shugart, 2010; Huntington et al., 2011) or other methods (Brutsaert and Stricker, 1979; Kahler and Brutsaert, 2006; Xu and Singh, 2005). Given the constraints of the model-model comparison reported in this study, it provides a useful framework for validating the NARR data. Also, it should be noted that since both CR and Noah LSM used the NARR data, the inherent bias in the forcings from NARR can be considered incongruous to our validation efforts.

After deriving independent values of b for two different vegetation types, sagebrush and cheatgrass, the CR-based equations (Equations (5.9) and (5.10)) were
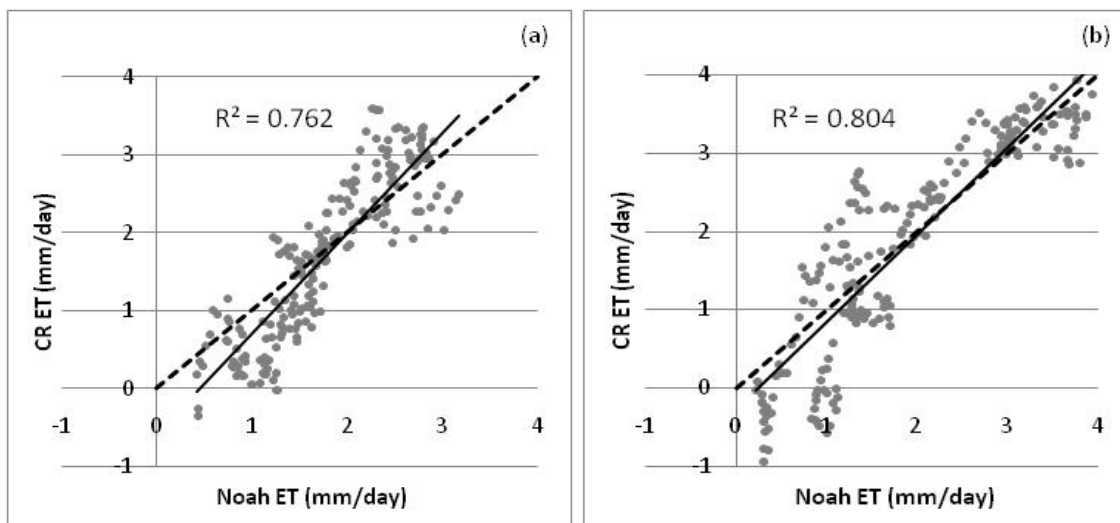
Figure 5.6. Scatter Plots of Noah ET vs ET Derived from the CR for (a) Sagebrush and (b) Cheatgrass in 2005. Dashed Line Is the 1:1 Line and the Solid Line Is the Trend Line.

evaluated by applying them over the same sites for a different year to predict ET, which subsequently compared them against the ET_{Noah}. Results for 2005 are shown in Figures 5.6, 5.7, and 5.8 to see if the derived relationship for 2010 was still valid for a time period other than the period it was derived for. This is necessary due to the lack of field observations from this vast expanse of natural vegetation landscape in Southern Idaho. The 7-day moving averages of ET_{Noah}, as well as PET and ET_w, were computed for 2005. Subsequently, ET was derived from CR (using Equations (5.9) and (5.10)) using the 7-day moving averages of PET and ET_w with the already derived b values for sagebrush and cheatgrass.

Figure 5.6 is the scatter plot of daily values of ET_{Noah} versus ET derived from the CR. ET from 1 March to 15 September was plotted since the b was derived for that period. Both sagebrush and cheatgrass sites showed a good agreement between ET_{Noah}
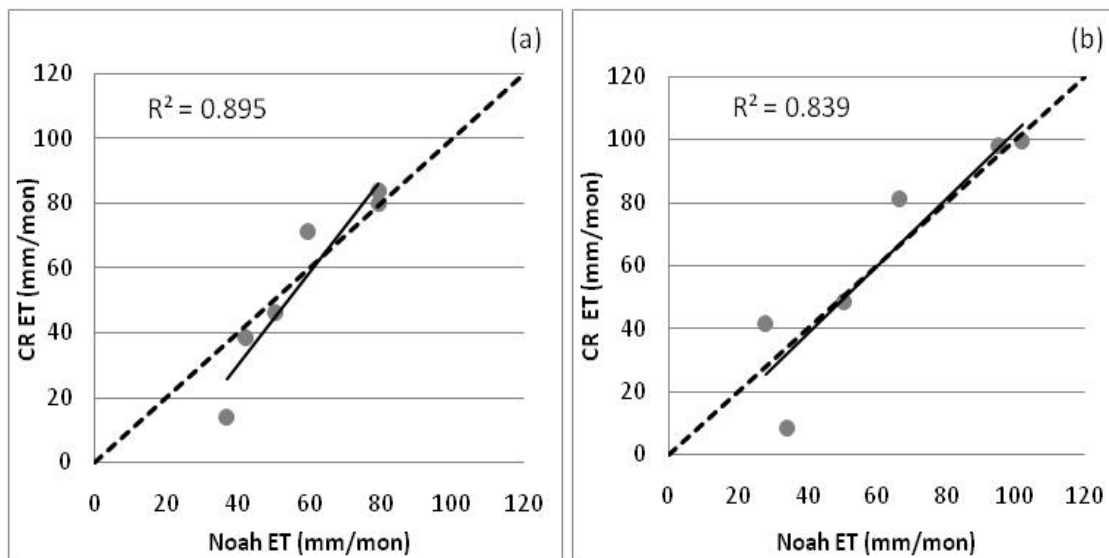
Figure 5.7. Scatter Plots of Noah ET vs ET Derived from the CR for Monthly ET for (a) Sagebrush and (b) Cheatgrass. Dashed Line Is the 1:1 Line and the Solid Line Is the Trend Line.

and ET derived from CR with R^2 of 0.76 and 0.80 for sagebrush and cheatgrass, respectively. Root mean squared errors (RMSE) were 0.53 and 0.61 mm day^{-1} with a negative bias in CR derived ET of 0.075 and 0.57 mm day^{-1}. RMSEs were minimum in June and May at these two locations (Table 5.1). Monthly ET plots (Figure 5.7) indicated the same pattern as in Figure 5.6. RMSEs of monthly total ET are 10.9 mm month^{-1} for the sagebrush site while it was 13.4 mm month^{-1} at the cheatgrass site.

Figure 5.8 is the time series of actual ET derived from the CR and Noah LSM for sagebrush and cheatgrass. CR underestimated ET mostly during early spring and late fall compared to ET$_{Noah}$. This is mainly because PET is higher than ET$_w$ by more than a factor of 2 as observed by Huntington et al. (2011) for winter months. This condition reduces or sometimes results in negative ET as seen in Figure 5.8. The Penman equation that was

Table 5.1. Statistics of Noah LSM ET and ET Derived from CR on Daily Timescale. RMSE: Root Mean Squared Error (mm day^{-1}), MBE: Mean Bias Error (mm day^{-1})

	Sagebrush		Cheatgrass	
	RMSE	MBE	RMSE	MBE
March	0.7654	0.4091	0.9368	0.8447
April	0.4424	0.1924	0.4025	0.0750
May	0.4884	0.7662	0.2217	-0.0881
June	0.4255	-0.4035	0.4211	0.0896
July	0.5828	-0.1444	0.5957	-0.4561
August	0.4339	0.3445	0.6920	-0.4282
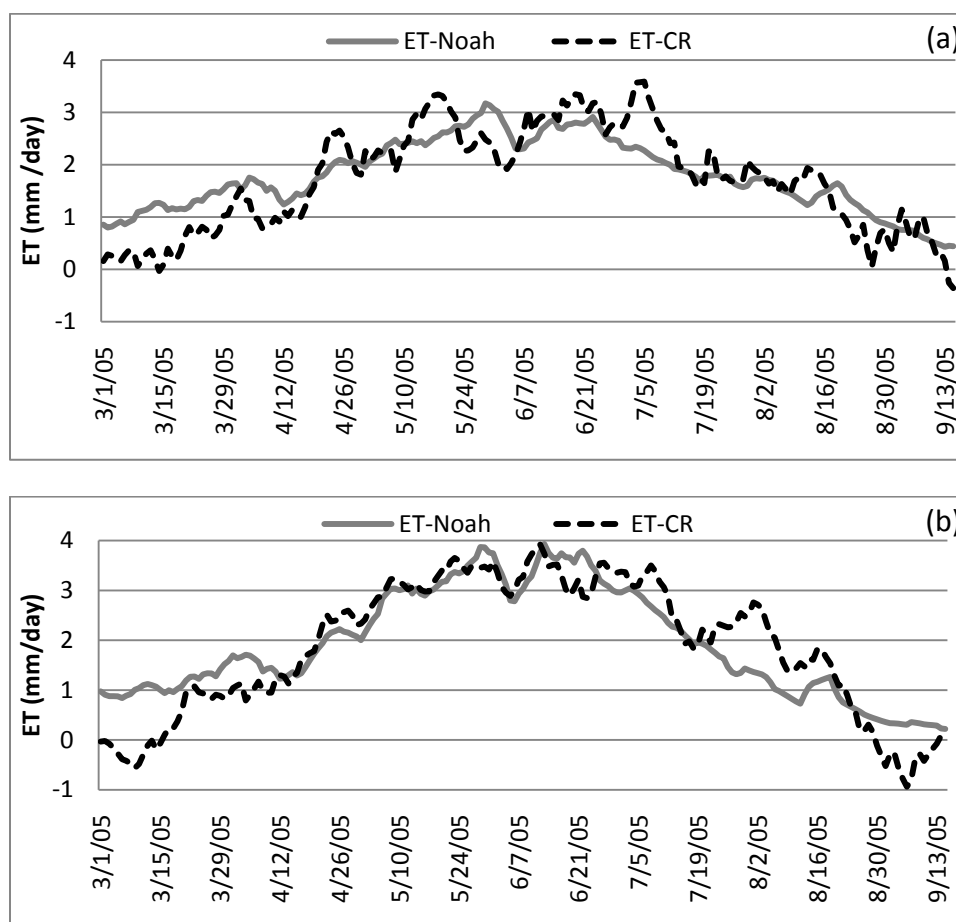
Figure 5.8. Time Series Plots of ET for (a) Sagebrush and (b) Cheatgrass. Gray Solid Line Denotes the Noah Predicted ET and Dotted Line Is ET Derived from CR.

used to calculate PET did not perform well during the winter months when the available energy was negative or very close to zero (Xu and Singh, 2005). At the cheatgrass site, CR derived ET was able to capture the peak ET that closely agreed both in magnitude and time with the ET_{Noah}. CR derived ET at sagebrush showed great variations and missed both the magnitude and timing of peak ET.

5.5 Conclusions on Complementary Relationship

The existence and application of a complementary relationship was tested here for natural vegetation in South Central Idaho with only modeled meteorological variables and without in-situ weather or flux data. Forcing variables were obtained from NARR for three hourly data sets, which were interpolated into hourly in the HRLDAS platform. The flux data, net radiation and ground heat flux, and actual ET were obtained from Noah LSM. PET and ET_w were computed using NARR variables and flux data from Noah LSM. South Central Idaho is a semiarid region mostly consisting of grasslands and shrublands. Two sites were chosen for this study with land cover of cheatgrass and sagebrush.

The analysis clearly showed the complementarity between ET_{Noah} and the PET calculated from the NARR data. Further, the b value was evaluated for both sites and it was found that the CR was asymmetric for two vegetation types with *b* values greater than unity. Applicability of CR was tested for a different year than it was derived for the same two sites. ET derived from the CR agreed well with ET_{Noah}. Low errors and high correlation coefficients gave promising results of using CR to estimate ET.

Given the semiarid conditions and the importance of water-related activities in the Snake River Plain of Southern Idaho, water resources management is a great challenge. Under the changing climate and the expected warming in this region, a change in the timing of water-cycle components is expected. However, understanding ET in this area is limited by the unavailability of long-term meteorological and energy balance components. A relatively simple method based on CR will be beneficial in water resources engineering.

CHAPTER SIX: RESULTS: LAND-ATMOSPHERE COUPLING EFFECTS

6.1 Introduction

The dynamically coupled system of the land and the atmosphere forms by the exchange of heat, moisture, and momentum. This interaction takes place through many processes, and evapotranspiration is one method of interaction through the exchange of moisture between the soil-vegetation-atmosphere continuum. The development of the boundary layer and its evolution both in time and space are greatly affected by the underlying land surface (Pielke et al., 1998; Pielke, 2001; Brubaker and Entekhabi, 1996; Pielke and Avissar, 1990). Surface energy fluxes and their partition between each component, especially into sensible and latent heat flux, influence the near-surface atmospheric properties. This influence varies between different land-cover types. Since this area consists of different vegetation types, assessment of their influence on the near-surface atmosphere was important in regional climate analysis. Also, the coupled model results enabled us to test the importance of coupling and how the coupling was important for different vegetation.

6.2 Coupling Effects on Surface Fluxes

In order to assess the effect of coupling on the surface fluxes, WRF simulations from a parallel project that is going on at Boise State University was compared with Noah LSM. As mentioned earlier, the difference between these two models are related to

the forcing data. In the uncoupled Noah LSM, NARR data provided the atmospheric

forcing, while in the coupled version of Noah LSM, WRF, forcing data for the LSM was

created by the coupled atmospheric models. WRF model results were available from 1

March 2010 to 30 September 2010 during the growing season. Therefore, analyses were

done only for this period. The same irrigation algorithm was applied in both models. The

effects of coupling on surface fluxes, which included sensible heat (SH), latent heat (LH),

ground heat (GH), and net radiation (R_n) were studied by comparing those results from

both coupled and uncouple model simulation and also through the statistics, namely

feedback factor and coupling strength, Ω.

6.2.1 Energy Partitioning

Mean hourly fluxes were calculated for the months during the growing season

from April to September in 2010 for both Noah LSM and WRF. Figures 6.1 (croplands),

6.2 (grasslands), and 6.3 (shrublands) show the mean diurnal energy budget from both

models in May, July, and September in 2010. Fluxes were calculated as hourly averages

for each land-cover type every month. Three months were selected for the analysis to

represent the three seasons, spring (May), summer (July), and fall (September). The time

difference of peak flux was observed between Noah and WRF, as observed between

Noah and field observations. As stated earlier, for Noah LSM, the time difference in

forcing fields caused the time difference in peak. WRF created its own radiation by

radiation scheme and output it every hour. Therefore, WRF captured the actual time of

peak in solar radiation. According to Figure 6.1, peak R_n in Noah tended to be
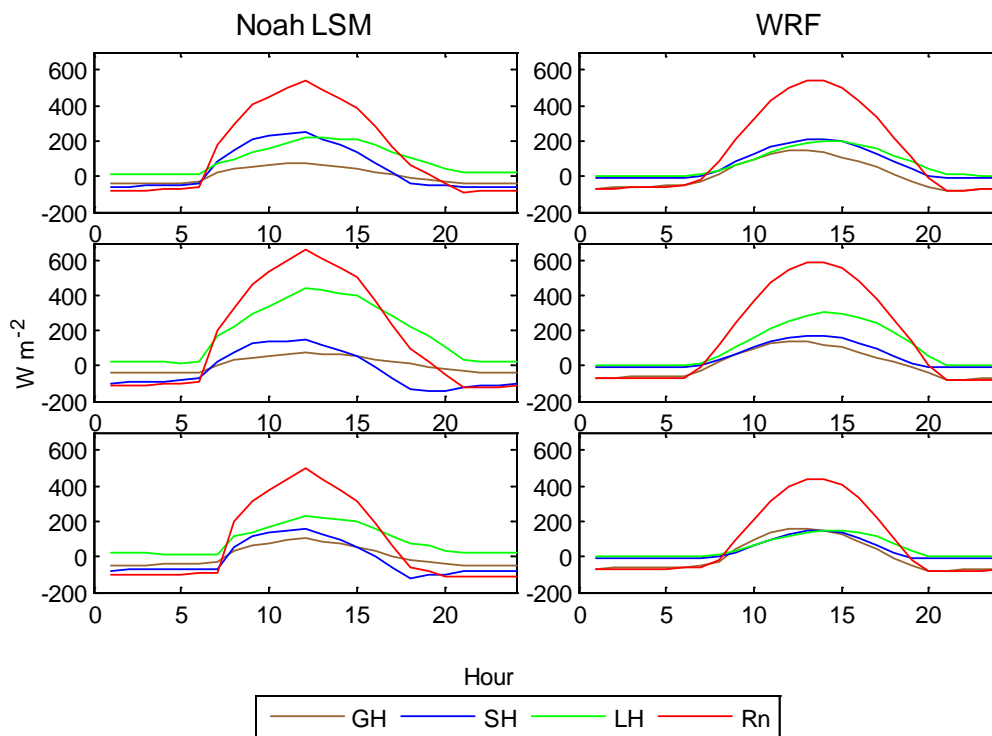
Figure 6.1 Diurnal Energy Budget in Months During the Growing Season, May (First Row), July (Second Row), and September (Third Row) from Noah LSM (Left Column) and WRF (Right Column) Averaged for All Irrigated Crop Cells

overestimated in July compared to that from WRF for croplands by about 77 W m^{-2}.

Also, peak LH was overestimated in Noah for the same months for croplands by 135 W

m^{-2} and the daily averaged LH by 75 W m^{-2} or about 6.5 MJ m^{-2} day^{-1}. This

overestimation in the uncoupled model can also be explained with the forcing data.

During the peak growing season, added moisture flux through high ET increased the

humidity and reduced the vapor pressure deficit close to the land surface. As a result, at

the next time step, actual ET should be reduced according to the complementary concept

by Bouchet (1963). However, since there was no feedback between the land surface and

the atmosphere in the uncoupled model, increased ET did not have an effect on the specific humidity at the next time step. Therefore, Noah LSM tended to overestimate ET during the peak growing season. In WRF, effects of land-surface processes were reflected in near-surface atmospheric properties through feedback mechanism. Compared to WRF, peak GH in Noah was low in July and September. During July, peak GH in Noah was 76 W m^{-2} while from the peak GH from WRF was 136 W m^{-2}. The peak value of SH was approximately the same for both models for all three months analyzed. Considering the daily average of fluxes for the three months, underestimation of SH and overestimation of LH for the irrigated cropland in Noah LSM was significant compare to GH or R_n.

Energy partitioning of two natural vegetation, grasslands and shrublands, was approximately the same in both models (Figures 6.2 and 6.3). However, R_n in the uncoupled Noah LSM was lower compared to WRF in all three months for grasslands. In July, R_n from Noah LSM ranged from -120 to 590 W m^{-2}, and from WRF the range was from -84 to 646 W m^{-2}. The daily average of fluxes indicated that this underestimation in R_n resulted in the underestimation of LH in Noah LSM for grasslands.

In May, energy was partitioned more towards the sensible heat flux than the latent and ground heat fluxes in natural vegetation lands (averaging about 54 % of R_n). WRF partitioned approximately the same amount of R_n (about 47 %) into SH and LH, while Noah favored more towards LH (66% into LH and 32 % into SH) in croplands. In July, during the peak growing season, net radiation was partitioned more into latent heat flux at croplands in both the Noah and WRF models. This was due to the irrigation water received by this area increasing the soil moisture, which increases ET, creating more
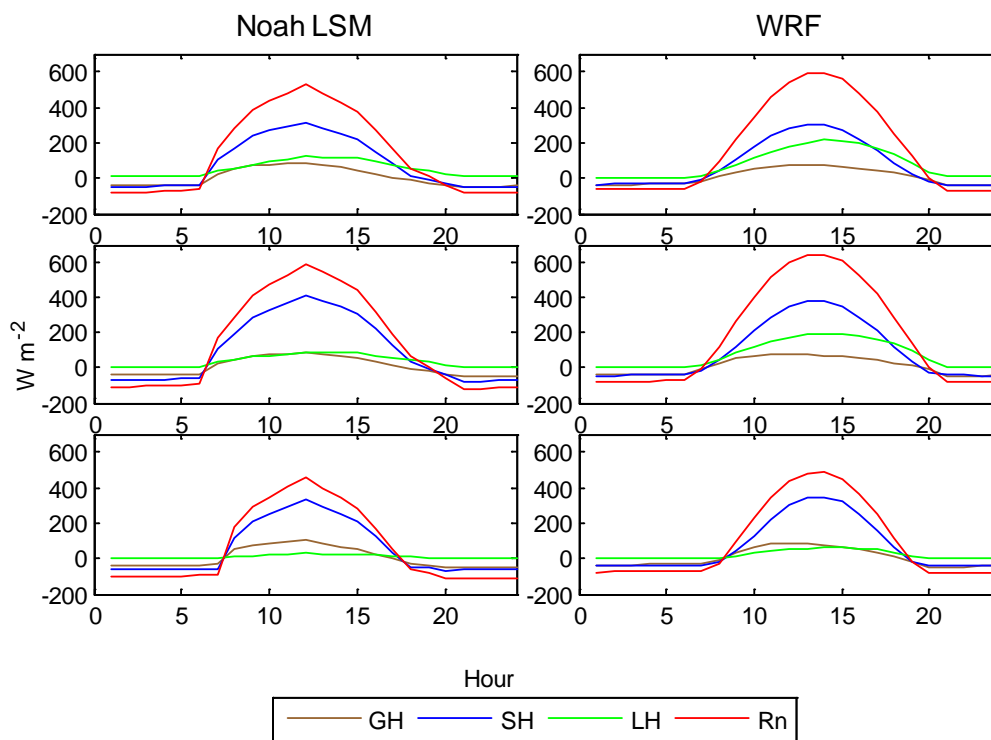
Figure 6.2 Diurnal Energy Budget in Months During the Growing Season, May (First Row), July (Second Row), and September (Third Row) from Noah LSM (Left Column) and WRF (Right Column) Averaged for All Grassland Cells

latent heat flux. For the other two land-cover types, the same pattern as in April was seen,

mainly due to the low soil moisture conditions during this time of the year. In summer,

precipitation was less and the soil was dry, which caused vegetation to be water stressed,

reducing transpiration. Therefore, a large fraction of net radiation was converted to

sensible heat flux (Avissar and Peilke, 1991). SH in croplands in July was greatly

underestimated by Noah when the total energy was considered (i.e., SH from Noah was

-1.96 MJ m^{-2} day^{-1} and from WRF, it was 4.32 MJ m^{-2} day^{-1}). In Section 4.7.3, it was

stated that the LH was higher than even R_n during the peak growing month in Noah LSM
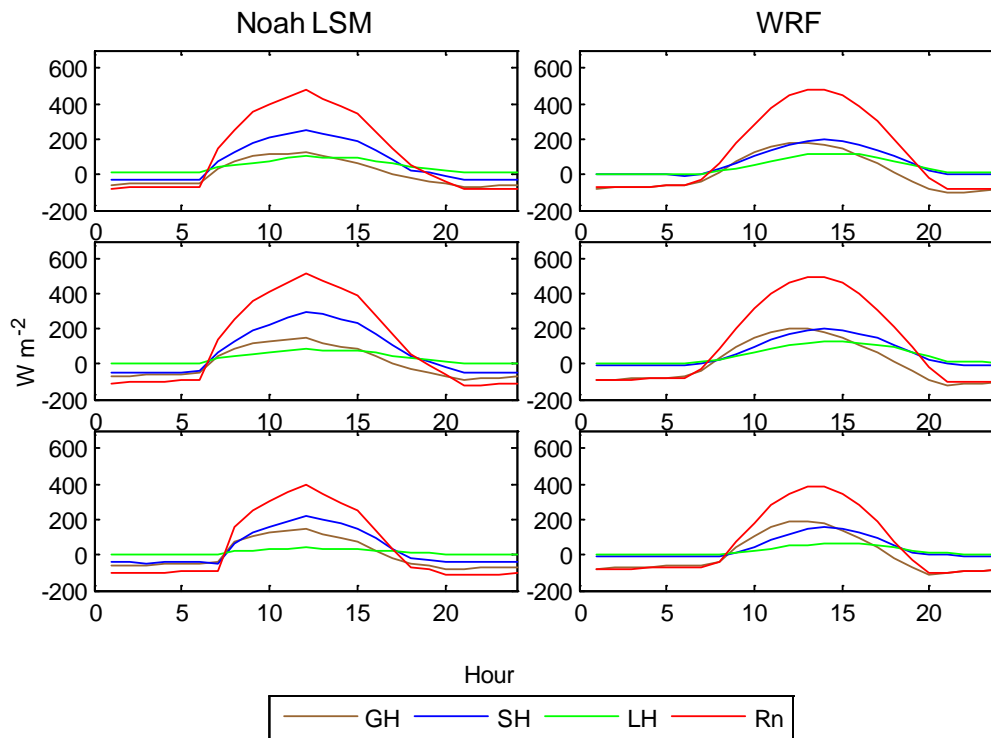
Figure 6.3 Diurnal Energy Budget in Months During the Growing Season, May (First Row), July (Second Row), and September (Third Row) from Noah LSM (Left Column) and WRF (Right Column) Averaged for All Shrubland Cells

and SH went below zero. This condition was similar to the analysis here.

Underestimation of SH from Noah LSM could be caused by the increased LH in the

absence of feedbacks.

In most cases, energy partitioning in September followed the same pattern as May

for natural vegetations (more than 60% of R_n into SH), but LH lower than in May

(averaging about 80% less LH). Soil moisture was higher in May than in September,

caused by the winter precipitation, and a considerable portion of R_n was used for LH. By

September, soil was very dry (less than 0.1 m^3 m^{-3} for grasslands and for shrublands less

than 0.15 m^3 m^{-3}) with very low summer precipitation leading to high SH (more than 300

W m^{-2} for grasslands and more than 150 W m^{-2} for shrublands from both models) and

very low LH, which was less than 100 Wm^{-2} with Noah LSM, predicting less than

50 Wm^{-2}. Over croplands, there may be some soil moisture remaining from irrigation

during the growing season and the LH was higher than for natural vegetation.

6.2.2 Feedback Factor

In order to assess the feedbacks between the land and the atmospheric processes,

feedback factor Φ_x was calculated for coupled and uncoupled simulations (Huang and

Margulis, 2010) as

$$\varphi_x = \frac{Simulated\ x_{coupled} - Simulated\ x_{uncoupled}}{Simulated\ x_{coupled}} \tag{6.1}$$

where x is the temporally averaged flux for a given vegetation type. If the value of Φ_x is

zero, it can be considered as the effect of atmospheric feedback on the flux *'x'* is zero.

Positive values indicate positive atmospheric feedbacks and the negative values indicate

the negative feedbacks. This Φ_x has been used to measure the effects of spatial variability

of atmospheric properties on a particular flux as reported by Huang and Margulis (2010)

and Hu and Islam (1997). Huang and Margulis (2010) checked the feedback factor from

multiple simulations with different coupling states of the near-surface atmospheric

properties. They identified that air humidity feedback is relatively unimportant compared

to air-temperature and wind-speed feedbacks in estimating the surface fluxes. However, since the two cases used here were fully coupled (WRF) and fully uncoupled (Noah LSM) systems, it was difficult to measure which particular atmospheric property caused more feedback effects.

Figure 6.4 shows the feedback factor of the energy budget components for each vegetation type representing three months. Monthly averaged fluxes were used here. According to Figure 6.4, R_n has a positive feedback in all the cases if there is any. Coupling had created positive feedbacks on SH and negative effects on LH for croplands. That was, by coupling the land surface and the atmosphere, SH had been increased and LH had been decreased for croplands. Compared to the other fluxes, R_n showed the least effect of coupling through feedbacks for croplands. GH always showed a positive feedback in the growing season and for all vegetation. During September, coupling had created positive feedbacks on all four flux over both sagebrush and grassland communities.

An important point to note here is that the coupling has increased SH more than 100% in July and September for croplands. When SH was analyzed for these months, it was observed that Noah LSM had a high negative bias during the night time. In July, monthly averaged night time SH went below -100 Wm^{-2} when the lowest night time SH for WRF was only about -10 Wm^{-2}. This negative bias in Noah LSM during the night time resulted in negative SH when averaged for the whole month. Therefore, the difference between the two models was more than 100%, which gave a feedback factor of more than 100%.
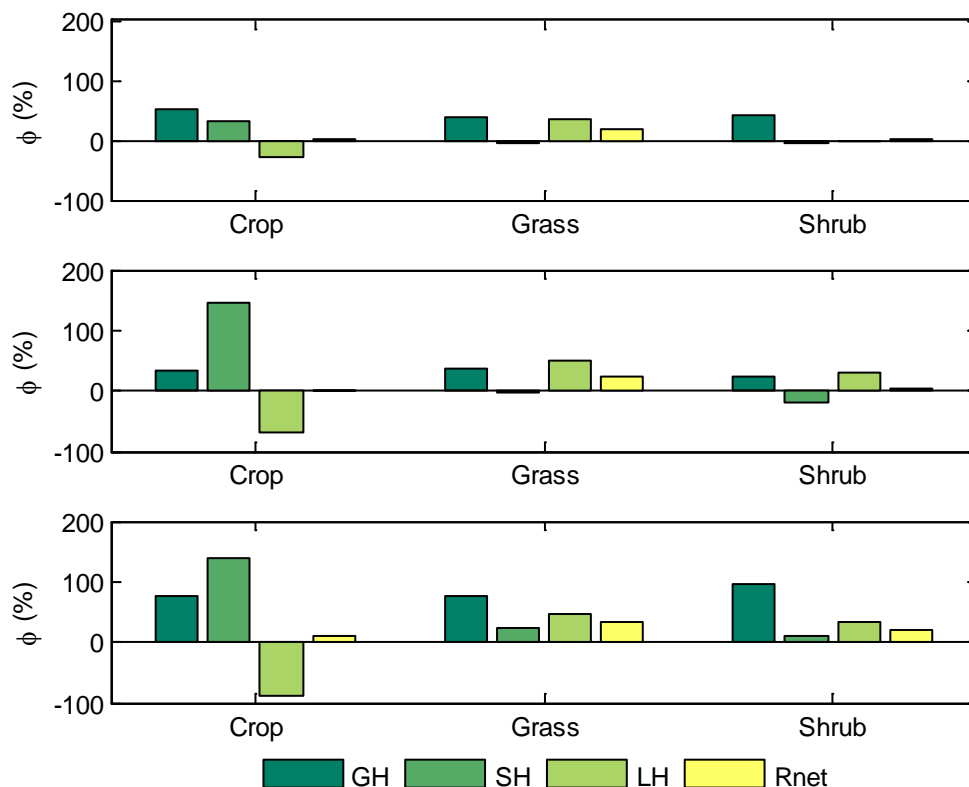
Figure 6.4 Feedback Factor for the Months During the Growing Season, May (First Row), July (Second Row), and September (Third Row) for Croplands, Grasslands, and Shrublands

In croplands, R_n is least affected by the coupling. A negative feedback factor in

LH for croplands was an indication of higher LH from Noah LSM compared to WRF. In

other words, LH has been reduced with coupling, indicating that Noah LSM

overestimates LH and thus ET. This overestimation can lead to the underestimation of

SH. Over grasslands and shrublands, LH has been underestimated by the Noah LSM. SH

was the least affected in grasslands. GH has been changed with coupling for all

vegetation in all the months analyzed. Noah LSM predicted GH is lower in all cases. In

September, the feedback factor is more than 75% for all vegetation for GH.

6.2.3 Coupling Strength

In order to measure the coupling strength, a metric developed by Koster et al. (2000) was computed, which is denoted by Ω. It measures the conformity of a time series of a variable from different model simulations. This metric has been usually used to measure the conformity across a range of ensemble members that have been initialized differently (Koster et al., 2002; Dirmeyer et al., 2006). However, in this study, the difference between the two models were related to the coupling only. It can take values between 0 and 1. The values closer to 1 indicate a strong relationship between the predicted variable from the two models. Daily averaged LH and SH was selected for this analysis since these two terms have a great effect on the evolution of the planetary boundary layer. For SH and LH, Ω_{SH} and Ω_{LH} were calculated for each grid cell in the domain and for the period from 1 March 2010 to 30 September 2010 as

$$\Omega_V = \frac{16\sigma_{\bar{V}}^2 - \sigma_V^2}{15\sigma_V^2} \qquad (6.2)$$

where V is the variable that is SH or LH, σ_V^2 is the variance of all data of SH or LH for a cell for the above time period, and $\sigma_{\bar{V}}^2$ is the variance of mean SH or LH of Noah LSM and WRF for a cell for the above period.

Figures 6.5 and 6.6 show the Ω_{SH} and Ω_{LH}, respectively, for the main four land-cover types in the domain, namely grasslands, shrublands, croplands, and forests. SH had a weak correlation between the two models for all croplands compared to the other types
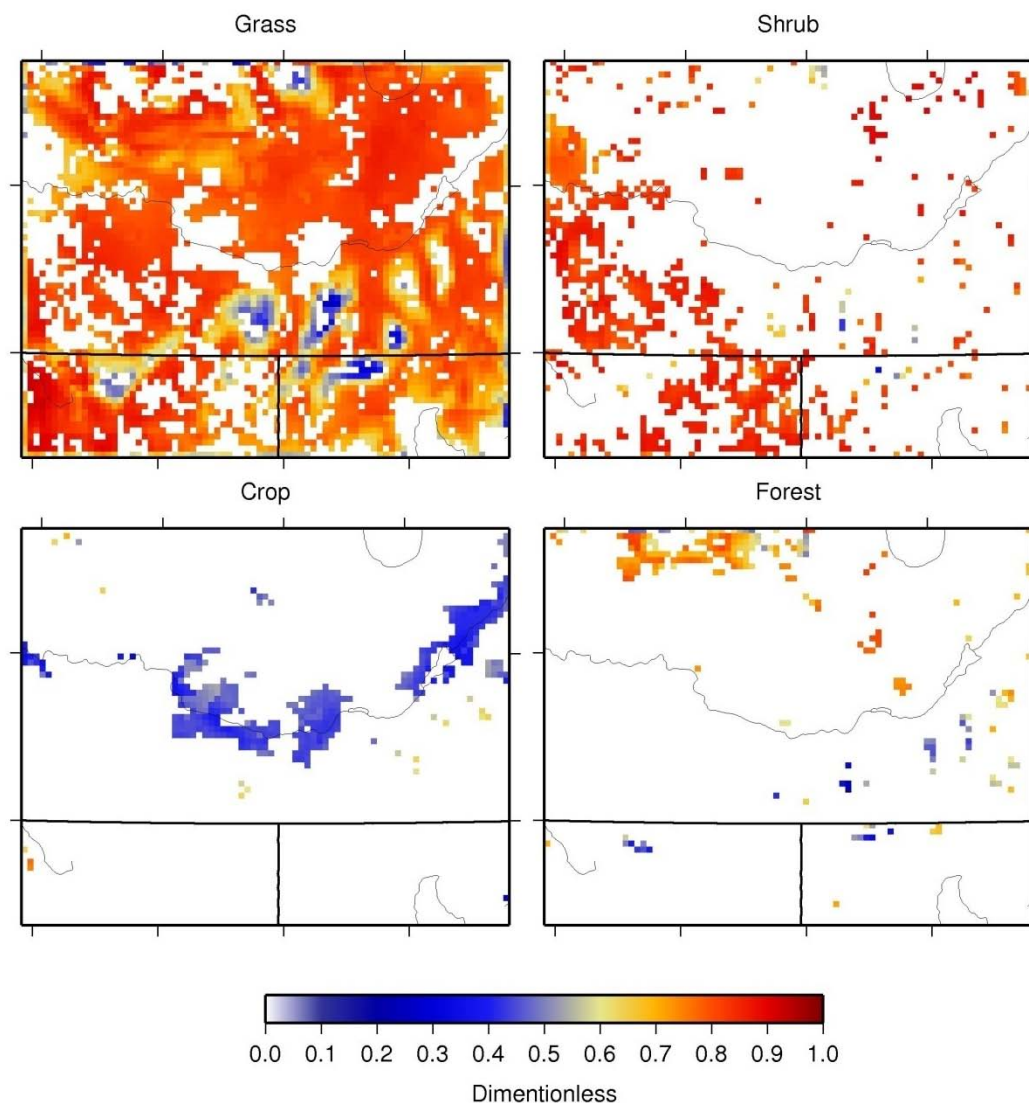
Figure 6.5 Coupling Strength, Ω, of Sensible Heat Flux for Four Main Land-Cover Types in the Domain

with an average of 0.45 (Figure 6.5). This was also observed with high feedback factors

(Figure 6.4) for SH. Shrublands showed a higher correlation of SH. The average Ω for all

shrublands was 0.82. LH had the weakest correlation for forests (average Ω = 0.36). For

shrublands, average Ω was 0.73, which showed a high correlation in LH from both
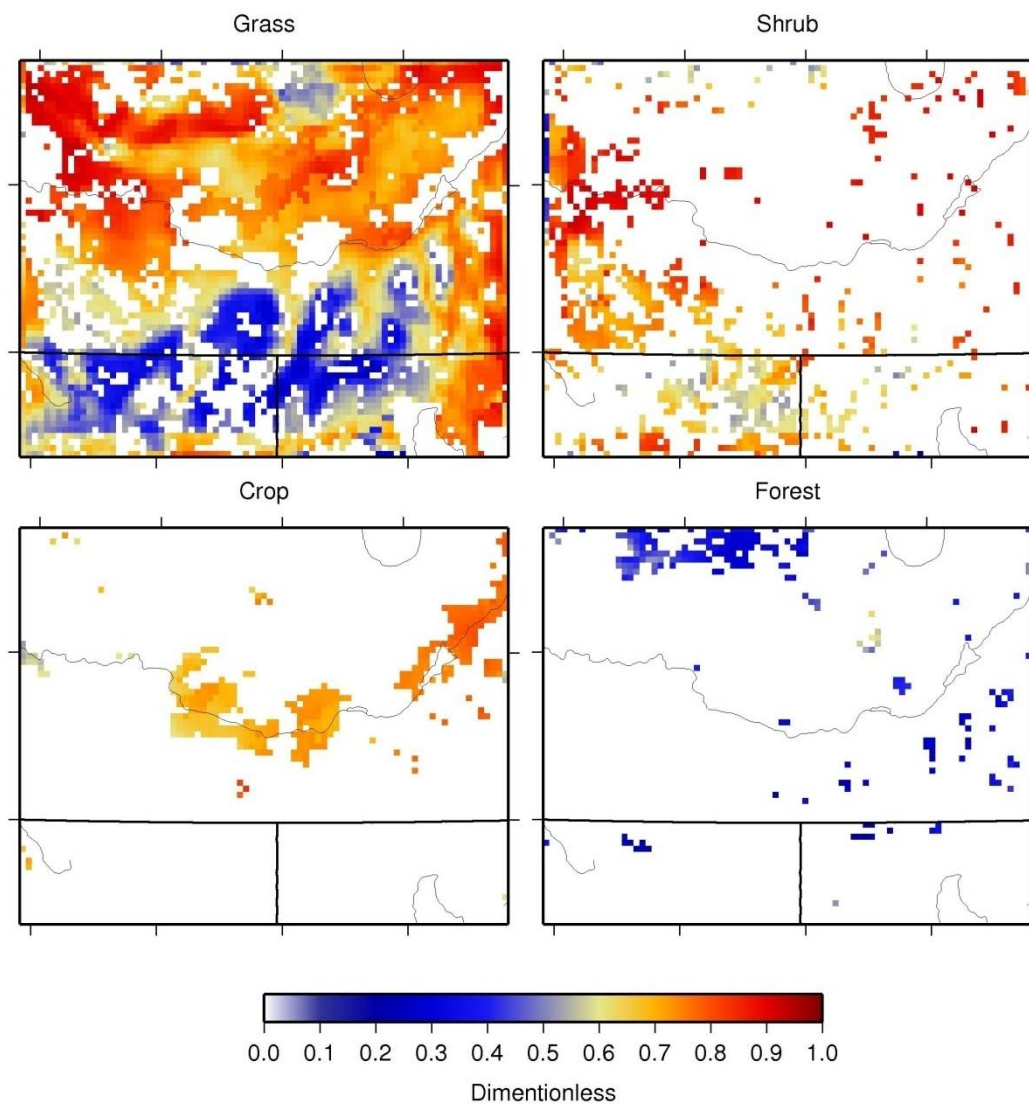
Figure 6.6 Coupling Strength, Ω, of Latent Heat Flux for Four Main Land-Cover Types in the Domain

models. All crop cells showed a high correlation with an average Ω of 0.72, indicating

that with the new irrigation scheme LH had been predicted approximately similarly.

Even though croplands showed a high correlation in LH, low Ω for SH showed

that coupling was important for croplands in order to better simulate surface fluxes. Since

the energy partitioning was impacted by the irrigation applied externally, coupling was critical in croplands to change the atmospheric properties, such as temperature and humidity, to represent the irrigated conditions. Forests also showed the necessity of coupling with high Ω for SH and low Ω for LH. Coupling was least important for grasslands and shrublands with high Ω for both SH and LH.

6.3 Evaluation of Near-Surface Atmospheric Properties

Planetary boundary layer (PBL), also known as the atmospheric boundary layer, is directly affected by the underlying land surface and its processes. In order to examine the effects of land-surface processes from different vegetation types, near-surface atmospheric properties, potential temperature, and specific humidity were examined. Monthly averaged values of potential temperature and specific humidity were computed for each vertical level in WRF averaged for three main land-cover types, croplands, grasslands, and shrublands.

6.3.1 Potential Air Temperature

The resulting temperature of an air parcel, if it was brought adiabatically to a standard pressure level, is called the potential temperature (PT). The vertical profile of the PT determines the planetary boundary layer depth. Usually, when the earth surface is warmer than the air above, PBL is said to be unstable and PBL is stable when the earth surface is colder than the air (Stull, 2006). Figures 6.7, 6.8, and 6.9 show the vertical profiles of potential temperature (PT) of the first 20 vertical levels in May, July, and
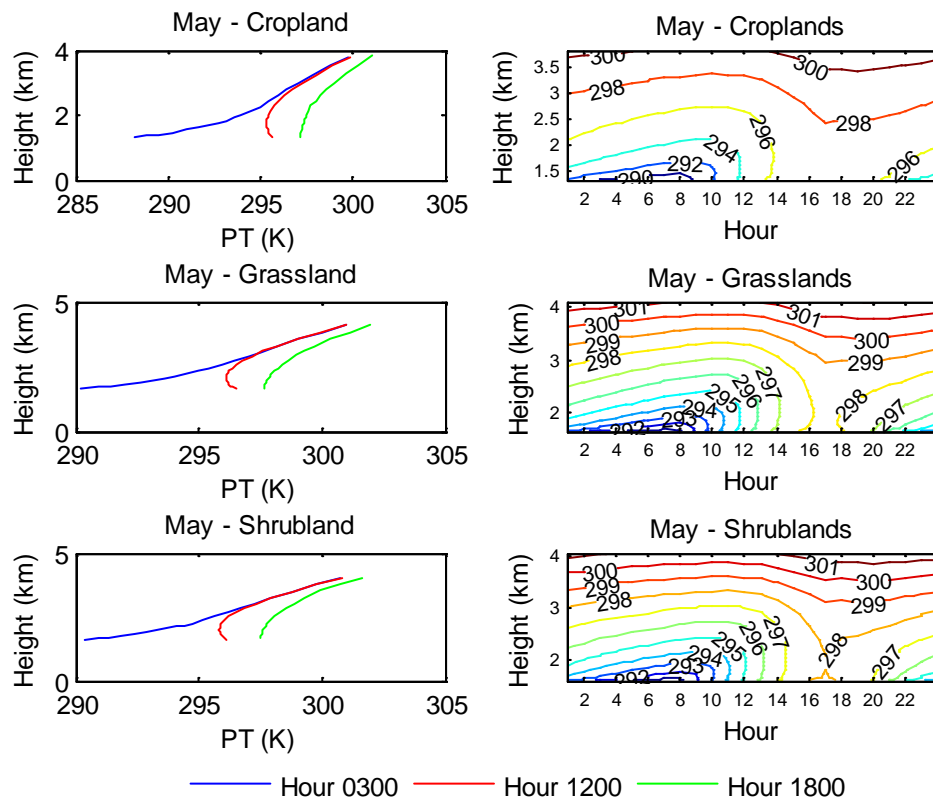
Figure 6.7. Vertical Profiles of Potential Temperature (PT) for Croplands, Grasslands, and Shrublands in May. Height in Y-axis Is the Height from Sea Level. First Column Shows the Vertical Profiles at Three Time Steps and the Second Column Shows the Evolution of the Vertical Profile During a Day

September, respectively. The first column shows the vertical profiles at three time steps (3 a.m., 12 noon, and 6 p.m.) and the second column is the evolution of the vertical profile during a day. The potential temperature in May was the lowest during the morning and increased by 6 p.m. (hour 1800) for all three land-cover types. At 12 noon, the atmosphere close to the ground showed unstable conditions (PT decreases with height) and by 6 p.m. (hour 1800), became more stable (PT increases with height). September showed the same conditions as in May but with a shallower unstable layer, which was
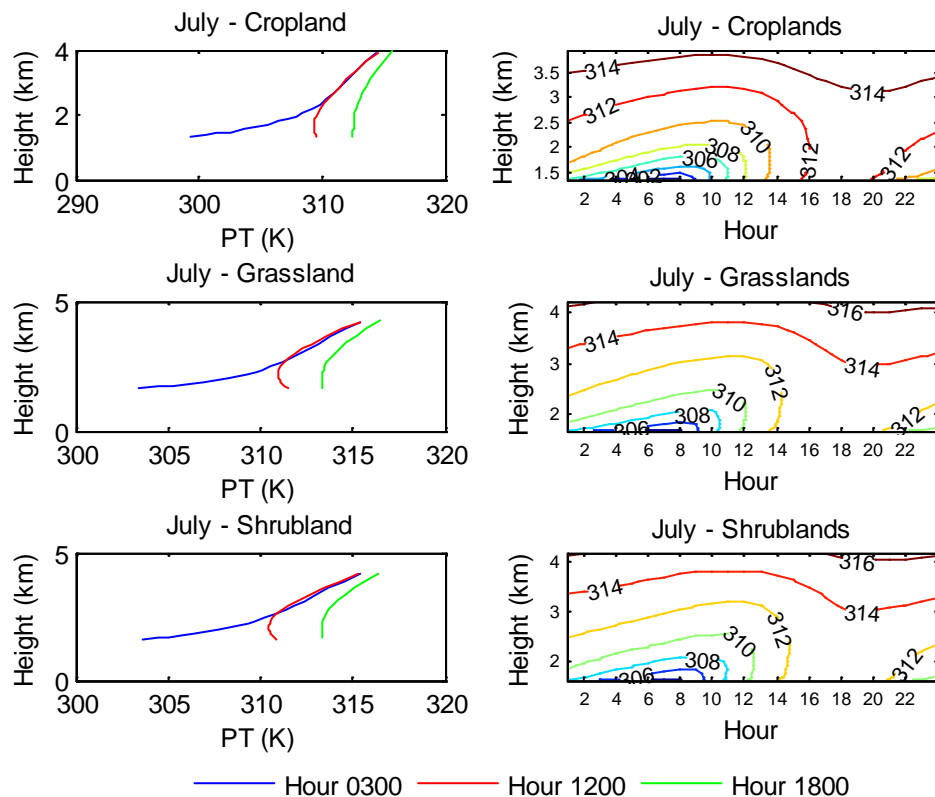
Figure 6.8. Vertical Profiles of Potential Temperature (PT) for Croplands, Grasslands, and Shrublands in July. Height in Y-axis Is the Height from Sea Level. First Column Shows the Vertical Profiles at Three Time Steps and the Second Column Shows the Evolution of the Vertical Profile During a Day

0.45 m less than in May as an average.

Figure 6.10 shows the development of the planetary boundary layer during the day with and without the application of irrigation. Only monthly averages of May, July, and September are shown here. PBL height was maximum during the daytime when the earth surface was warmer than the air above. During the night time, the height ranged approximately 100 – 200 m from the ground. During May, irrigation had not affected the
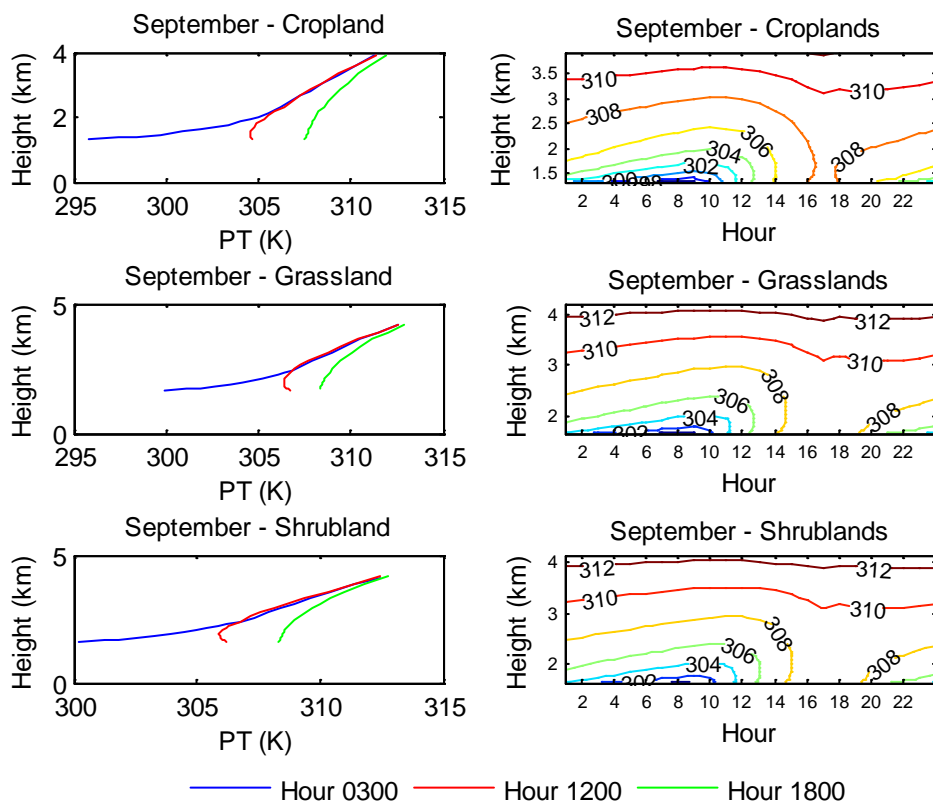
Figure 6.9. Vertical Profiles of Potential Temperature (PT) for Croplands, Grasslands, and Shrublands in September. Height in Y-axis Is the Height from Sea Level. First Column Shows the Vertical Profiles at Three Time Steps and the Second Column Shows the Evolution of the Vertical Profile During a Day

development of the PBL, and the PBL height ranged from 1.6 km – 1.8 km for the three

vegetation types. In WRF, irrigation first started in July and therefore May did not have

any effects from irrigation. In July (peak growing month), irrigation had brought down

the peak PBL height for croplands by approximately 150 m. For natural vegetations, the

peak height was around 2.2 km and 2.3 km. The reduction in peak PBL height over

croplands in September was around 350 m. This reduction was higher than that of July

because without irrigation, September was very dry for all vegetation. In July, even
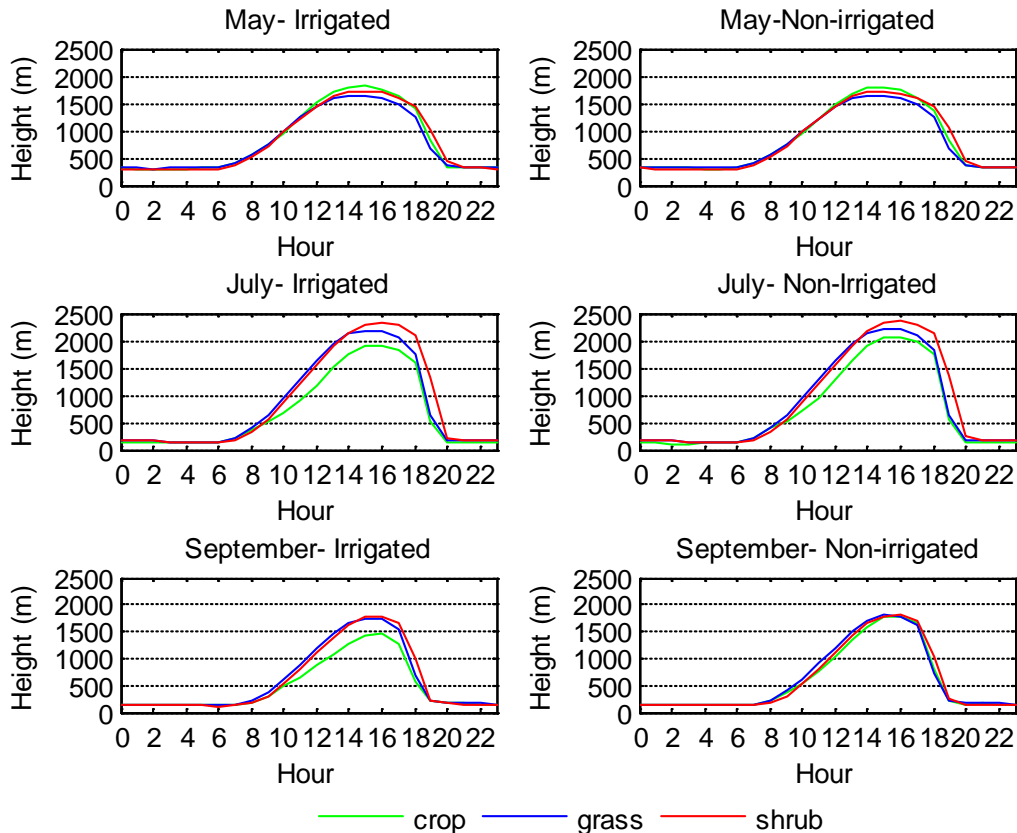
Figure 6.10. Evolution of Planetary Boundary Layer Height During a Day Over Three Vegetations in May (First Row), July (Second Row), and September (Third Row) with (First Column) and without (Second Column) Irrigation

without irrigation, PBL height over croplands was lower than other natural vegetation (2 km for croplands and 2.2 – 2.3 km for natural vegetation) because of the high green vegetation fraction in the growing season, which resulted in a cooler surface over the croplands than for natural vegetation. Therefore, the reduction in height compared to non-irrigated conditions was less for July.
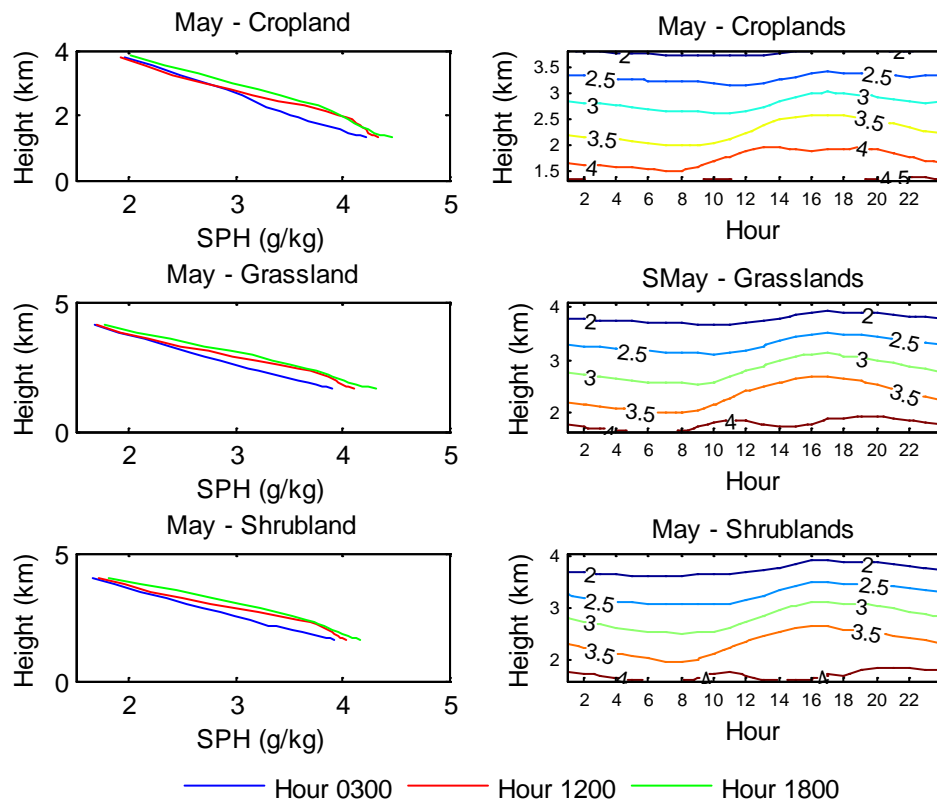
Figure 6.11. Vertical Profiles of Specific Humidity (SPH) for Croplands, Grasslands, and Shrublands in May. Height in Y-axis Is the Height from Sea Level. First Column Shows the Vertical Profiles at Three Time Steps and the Second Column Shows the Evolution of the Vertical Profile During a Day

6.3.2 Specific Humidity

Due to the soil moisture added from the land surface through evapotranspiration (ET), the specific humidity close to the ground was higher and rapidly decreased with the height. Figure 6.11, 6.12, and 6.13 show the vertical profiles of specific humidity for May, July, and September, respectively, for the three main vegetation types, croplands, grasslands, and shrublands. During May, conditions were the same for all three vegetations. However, in July and September, there was a clear difference between
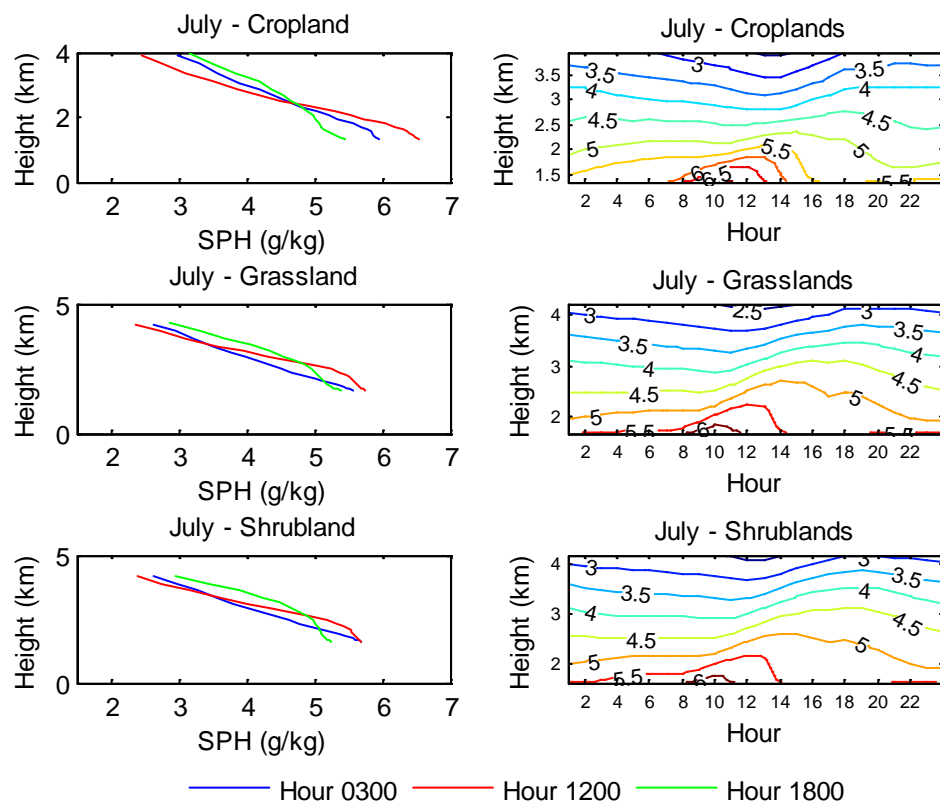
Figure 6.12. Vertical Profiles of Specific Humidity (SPH) for Croplands, Grasslands, and Shrublands in July. Height in Y-axis Is the Height from Sea Level. First Column Shows the Vertical Profiles at Three Time Steps and the Second Column Shows the Evolution of the Vertical Profile During a Day

croplands and natural vegetation. The increase in ET due to irrigation had caused an increase in specific humidity close to the land surface in croplands during the mid day. At 12 noon (1200 hour) in July, specific humidity close to the ground over croplands was 6.55 g kg^{-1}, while for grasslands and shrublands they were 5.75 g kg^{-1} and 5.69 g kg^{-1}, respectively. Variations in specific humidity during the day were high for croplands (ranged from 5.43 g kg^{-1} to 7 g kg^{-1}), while it did not vary much over grasslands and shrublands (average range was 5.21 g kg^{-1} to 6.20 g kg^{-1}).
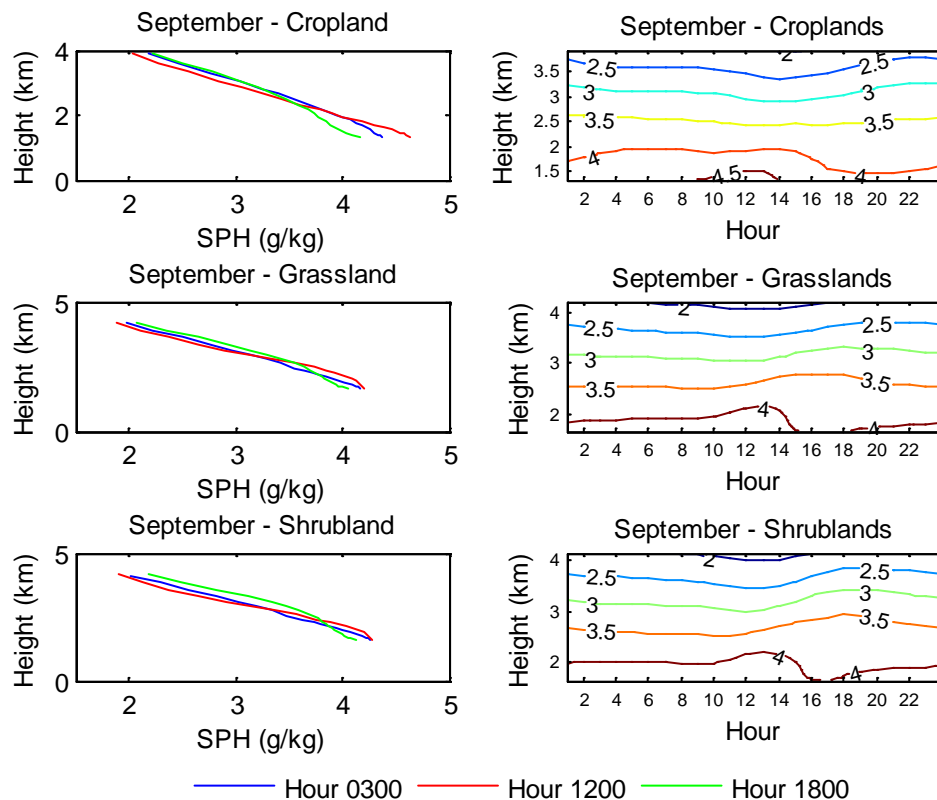
Figure 6.13. Vertical Profiles of Specific Humidity (SPH) for Croplands, Grasslands, and Shrublands in September. Height in Y-axis Is the Height from Sea Level. First Column Shows the Vertical Profiles at Three Time Steps and the Second Column Shows the Evolution of the Vertical Profile During a Day

6.4 Conclusions on Land-Atmosphere Coupling Effects

This section investigated the impacts and the importance of coupling and the influence of land-surface processes in the lower atmosphere. The result from a parallel project, which uses the coupled Noah LSM, WRF, was used to achieve the objectives. An analysis was done from April 2010 to September 2010 and only three months were presented in this section. Coupling effects were analyzed through surface fluxes and two

statistics. The near-surface atmospheric properties, potential temperature, and specific humidity were used to evaluate the effects of land-surface processes.

The irrigation during the growing season produces increased LH from both of the models for croplands. The results showed that LH was overestimated by Noah LSM with irrigation over croplands. In order to compensate this, SH was reduced and greatly underestimated. This was also shown by the feedback factor and the coupling strength, Ω. It was noticed that feedback factor was positive for SH and negative for LH in croplands. Low values of Ω_{SH} indicated that there was a weak correlation between SH from two models. Effects of coupling on grasslands and shrublands were minimal. Coupling strength analysis stressed the importance of feedback coupling in croplands and also in forests.

Irrigation caused the reduction in PBL height over croplands due to lower heating over the croplands. Due to the effects of vegetation on the ground, the atmosphere close to the land was unstable. Night time showed stable conditions with very shallow PBL height. Another effect of irrigation on the atmosphere was the increased specific humidity.

CHAPTER SEVEN: CONCLUSIONS

Based on all the results and analysis, the conclusions can be summarized as follows.

Irrigation was identified as a key process in semiarid agricultural regions that should be included in LSM in simulating energy budget and water budget components. Irrigation had significant effects on both energy and water budget components (soil moisture). The implemented irrigation algorithm produced reasonable results that agreed with spatial and temporal variations of ET compared with METRIC ET maps. The main impacts of irrigation were increased growing season ET or LH, reduced SH, increased soil moisture, and surface cooling.

Long term analysis showed that variations of ET from grasslands and shrublands were more correlated with the variations of precipitation. Both land types showed increasing ET trends for the past 30 years. A decreasing diurnal temperature range could be considered as one cause for this trend. An important behavior noticed in the analysis was the complementary relationship between Noah simulated ET and PET calculated from NARR meteorological variables and Noah output in grasslands and shrublands. The complementary relationship was symmetric with the proportionality constant, b, being greater than unity.

A comparison between coupled and uncoupled Noah LSM showed that the uncoupled model tended to overestimate LH and underestimate SH over croplands.

A feedback factor and coupling strength analysis showed that coupling was important in croplands and forest regions where coupling had the least effect over grasslands and shrublands. Slower heating resulted from irrigation, and reduced the PBL height during the daytime over croplands. Increased ET through irrigation added more moisture to the lower atmosphere and increased the specific humidity.

In this study, the same irrigation conditions were applied for all crop types with an implemented irrigation algorithm. In reality, different crop types behave in different ways. Also, there is more than one irrigation method available in the field with different conditions (different parameters). An investigation of different irrigation methods that treat the variations in crop types would be an extension to this work in the future. Because of the limitation of the period of site observations available, they were not used in derivation of the complementary theory in this study. However, the long-term coverage of field measurements can give a good opportunity to test the complementary behavior in grasslands and shrublands in the future.

REFERENCES

Adegoke, J.O., R. Pielke, and A.M. Carleton (2007). "Observational and modeling studies of the impact of agriculture-related land use change on planetary boundary layer processes in the central U.S.," *Agricultural and Forest Meteorology*, 142, 203-215.

Adegoke, J.O., R.A. Pielke, J. Eastman, R. Mahmood, and K.G.Hubbard (2003). "Impact of irrigation on midsummer surface fluxes and temperature under dry synoptic conditions: A regional atmospheric model study of the U.S. High Plains," *Monthly Weather Review*, 131, 556-564.

AgriMet (2011). "AgriMet weather Data," Internet: http://www.usbr.gov/pn/agrimet/wxdata.html. Accessed 02/09/2011.

Alfieri, J.G., X. Xiao, D. Niyogi, R.A. Pielke, F. Chen, and M.A. LeMone (2009). "Satellite-based modeling of transpiration from the grassland in the southern Great Plains, USA," *Global and Planetary Change*, 67 (2009), 78-86.

Allen, R.G., M. Tasumi, A. Morse, R. Trezza, J.L. Wright, W. Bastiaanssen, W. Kramber, I. Lorite, and C.W. Robison (2007a). "Satellite-based energy balance for mapping evapotranspiration with internalalized calibration (METRIC) - applications," *Journal of Irrigation and Drainage Engineering*, ASCE, 395-406.

Allen, R.G., M. Tasumi, and R. Trezza (2007b). "Satellite-based energy balance for mapping evapotranspiration with internalized calibration (METRIC) - Model," *Journal of Irrigation and Drainage Engineering*, ASCE, 133(4), 380-394.

Anthes, R.A. (1984). "Enhancement of convective precipitation by mesoscale variations in vegetative cover in semiarid regions," *Journal of Climate and Applied Meteorology*, 23, 541-554.

Avissar, R., and R.A. Pielke (1991). "The impact of plant stomatal control on mesoscale atmospheric circulations," *Agricultural and Forest Meteorology*, 54, 353-372.

Avissar, R., C.P. Weaver, D.Werth, R.A. Pielke Sr., R. Rabin, A.J. Pitman, M.A.S. Dias (2004). "The regional climate," *Vegetation, water, humans and the climate*, P. Kabat, M. Claussen, P.A. Dirmeyer, J.H.C. Gash, L.B. De Guenni, M. Meybeck, R.A. Pielke Sr., C.J. Vorosmarty, R.W.A. Hutjes, S. Lutkemeier, eds., , Springer Verlag, 21-32.

Bastiaanssen, W.G.M., M. Menenti, R.A. Feddes, and A.A.M. Holtslag (1998). "A remote sensing surface energy balance algorithm (SEBAL). 1: Formulation," *Journal of Hydrology*, 212-213, 198-212.

Betts, A.K., F. Chen, K.E. Mitchell, and Z. Janjic (1997). "Assessment of the land surface and boundary layer models in the two operational versions of the NCEP Eta model using FIFE data," *Monthly Weather Review*, 125, 2896-2916.

Blyth E.M., A.J. Dolman, and J. Noilhan (1994). "The effect of eorest on mesoscale rainfall: An example from HAPEX-MOBILHY," *Journal of Applied Meteorology*, 33, 445-454.

Bouchet, R.J. (1963). "Evapotranspiration r'eelle et potentielle, signification climatique," *Int. Assoc. Sci. Hydrol.*, Gentbrugge, Belgium, 62, 134-142.

Brubaker, K.L., and D. Entekhabi (1996). "Analysis of feedback mechanisms in land-atmosphere interaction," *Water Resources Research*, 32, 1343-1357.

Brutsaert, W., and M.B. Parlange (1998). "Hydrologic cycle explains the evaporation paradox," *Nature*, 396, 30.

Brutsaert, W., and H. Stricker (1979). "An advection-aridity approach to estimate actual regional evapotranspiration," *Water Resources Research*, 15(2), 443-450.

Charney, J.G. (1975). "Dynamics of deserts and drought in the Sahel," *Quarterly Journal of the Royal Meteorological Society*, 101, 193-202.

Chen, F. and J. Dudhia (2001a). "Coupling an advanced land surface-hydrology model with the Penn State-NCAR MM5 modeling system. Part I:Model implementation and sensitivity," *Monthly Weather Review*, 129, 569-585.

Chen, F. and J. Dudhia (2001b). "Coupling an advanced land surface–hydrology model with the Penn State–NCAR MM5 modeling system. Part II: Preliminary model validation," *Monthly Weather Review*, 129, 587- 604.

Chen, F., Z. Janjic, and K.E. Mitchell (1997). "Impact of atmospheric surface-layer parameterizations in the new land-surface scheme of the NCEP mesoscale Eta model," *Boundary Layer Meteorology*, 85, 391-421.

Chen, F., K.W. Manning, M.A. LeMone, S.B. Trier, J.G. Alfieri, R. Roberts, M. Tewari, D. Niyogi, T.W. Horst, S.P. Oncley, J.B. Basara, and P.D. Blanken (2007). "Description and evaluation of the characteristics of the NCAR high-resolution land data assimilation system," *Journal of Applied Meteorology and Climatology*, 46, 694-713.

Chen, F., K. Mitchell, J. Schaake, Y. Xue, H. Pan, V. Koren, Q.Y. Duan, M. Ek, and A. Betts (1996). "Modeling of land surface evaporation by four schemes and comparison with FIFE observations," *Journal of Geophysical Research*, 101, 7251-7268.

Chen, Y., K. Yang, D. Zhou, J. Qin, and X. Guo (2010). "Improving the Noah land surface model in arid regions with an appropriate parameterization of the thermal roughness length," *Journal of Hydrometeorology*, 11, 995-1006.

Chen, F., D.N. Yates, H. Nagai, M.A. Lemone, K. Ikeda, and R.L. Grossman (2003). "Land surface heterogeneity in the cooperative atmosphere surface exchange study (CASES-97). Part I: Comparing model surface flux maps with surface-flux tower and aircraft measurements," *Journal of Hydrometeorology*, 4, 196-218.

Chen, F., and Y. Zhang (2009). "On the coupling strength between the land surface and the atmosphere: From viewpoint of surface exchange coefficients," *Geophysical Research Letters*, 36, L10404, doi:10.1029/2009GL037980.

Cook, B.I., M.J. Puma, and N.Y. Krakauer (2010). "Irrigation induced surface cooling in the context of modern and increased greenhouse gas forcing," *Climate Dynamics*, DOI 10.1007/s00382-010-0932-x.

Dirmeyer, P.A., R.D. Koster, and Z. Guo (2006). "Do global models properly represent the feedback between land and atmosphere?," *Journal of Hydrometeorology*, 7, 1177-1198.

Easterling, D.R., B. Horton, P.D. Jones, T.C. Peterson, T.R. Karl, D.E. Parker, M.J. Salinger, V. Razuvayev, N. Plummer, P. Jamason, and C.K. Folland (1997). "Maximum and minimum temperature trends," *Science*, 277, 364-366

Ek, M., and L. Mahrt (1991). *OSU 1-D PBL model user's guide*, Department of Atmospheric Science, Oregon State University, Corvallis, Oregon.

Ek, M.B., K.E. Mitchell, Y. Lin, E. Rogers, P. Grunmann, V. Koren, G. Gayno, and J.D. Tarpley (2003). "Implementation of Noah land surface model advances in the National Centers for Environmental Prediction operational mesoscale Eta model," *Journal of Geophysical Research*, 108, 8851, doi:10.1029/2002JD003296.

Evans, J.P., and B.F. Zaitchik (2008). "Modeling the large-scale water balance impact of different irrigation systems," *Water Resources Research*, 44, W08448, doi:10.1029/2007WR006671.

Foken, T. (2008). "The energy balance closure problem: An overview," *Ecological Applications*, 18(6), 1351-1367.

Godfrey, C.M., and D.J. Stensrud (2010). "An empirical latent heat flux parameterization for the Noah land surface model," *Journal of Applied Meteorology and Climatology*, 49, 1696-1713.

Granger, R.J., and D.M. Gray (1989). "Evaporation from natural nonsaturated surfaces," *Journal of Hydrology*, 111, 21-29.

Grell, G., J. Dudhia, and D. Stauffer (1994). "A Description of the fifth-generation Penn State/NCAR mesoscale model (MM5)," *NCAR Technical Note*, NCAR/TN-398 + STR, 117 pgs.

Gutman, G., and A. Ignatov (1998). "Derivation of green vegetation fraction from NOAA/AVHRR for use in numerical weather prediction models," *International Journal of Remote Sensing*, 19(8), 1533-1543.

Haddeland, I., D.P. Lettenmaier, and T. Skaugen (2006). "Effects of irrigation on the water and energy balances of the Colorado and Mekong river basins," *Journal of Hydrology*, 324 (2006), 210-223.

Henderson-Sellers, A., R.E. Dickinson, T.B. Durbidge, P.J. Kennedy, K. McGuffle and A.J. Pitman (1993). "Tropical deforestation; Modeling local- and regional-scale climate change," *Journal of Geophysical Research*, 98, 7289-7315.

Hobbins, M.T., J.A. Ramírez and T.C. Brown (2004). "Trends in pan evaporation and actual evapotranspiration across the conterminous U.S.: Paradoxical or complementary?," *Geophysical Research Letters*, 31, L13503, doi:10.1029/2004GL019846.

Hobbins, M.T., J.A. Ramírez, and T.C. Brown (2001). "The complementary relationship in estimation of regional evapotranspiration: An enhanced advection-aridity model," *Water Resources Research*, 37 (5), 1389-1403.

Hogue, T.S., L. Bastidas, H. Gupta, S. Sorooshian, K. Mitchell, and W. Emmerich (2005). "Evaluation and transferability of the Noah land surface model in semiarid environments," *Journal of Hydrometeorology*, 6, 68-84.

Hu, Z., and S. Islam (1997). "Effects of spatial variability on the scaling of land surface parameterizations," *Boundary Layer Meteorology*, 83, 441-461.

Huang, H.-Y., and S.A. Margulis (2010). "Evaluation of a fully-coupled LES-LSM model and its diagnosis of land atmosphere feedbacks," *Water Resources Research*, 46, W06512, doi:10.1029/2009WR008232.

Huntington, J. L., J. Szilagyi, S. W. Tyler, and G. M. Pohll (2011). "Evaluating the complementary relationship for estimating evapotranspiration from arid shrublands," *Water Resources Research*, 47, W05533, doi:10.1029/2010WR009874.

Idaho NSF-EPSCoR (2010). "Climate Change Impacts Project- Flux Measurement," Internet: http://www.kimberly.uidaho.edu/epscor/. Accessed 09/08/2010.

Jacquemin, B., and J. Noilhan (1990). "Sensitivity study and validation of a land surface parameterization using the HAPEX-MOBILHY data set," *Journal of Boundary Layer Meteorology*", 52, 93-134.

Janjic, Z. I. (1990). "The step-mountain coordinate: Physical package," *Monthly Weather Review*, 118, 1429–1443.

Janjic, Z. I. (1996). "The surface layer in the NCEP Eta model," *Eleventh Conference on Numerical Weather Prediction*, Norfolk, VA, 19–23 August; Amer. Meteor. Soc., Boston, MA, 354–355.

Janjic, Z. I. (2002). "Nonsingular implementation of the Mellor–Yamada level 2.5 scheme in the NCEP meso model," *NCEP Office Note*, No. 437, 61 pgs.

Kahler, D.M., and W. Brutsaert (2006) "Complementary relationship between daily evaporation in the environment and pan evaporation," *Water Resources Research*, 42, W05413, doi:10.1029/2005WR004541.

Kenny, J.F., N.L. Barber, S.S. Hutson, K.S. Linsey, J.K. Lovelace, and M.A. Maupin (2009). "Estimated use of water in the United States in 2005," *U.S. Geological Survey Circular 1344*, 52pgs.

Kjelstrom, L.C. (1995). "Streamflow gains and losses in the Snake River and ground-water budgets for the Snake River Plain, Idaho and eastern Oregon," *US Geological Survey Water-Resources Investigation Report*, 03-4244.

Koren, V., J.C. Shaake, K.E. Mitchell, Q.Y. Duan, F. Chen, and J. Baker (1999). "A parameterization of snowpack and frozen ground intended for NCEP weather and climate models," *Journal of Geophysical Research*, 104, 19,569-19,585.

Koster, R.D., P.A. Dirmeyer, A.N. Hahmann, R. Ijpelaar, L. Tyahla, P. Cox, and M.J. Suarez (2002). "Comparing the degree of land-atmosphere interaction in four atmospheric general circulation models," *Journal of Hydrometeorology*, 3, 363-375.

Koster, R.D., M.J. Suarez, and M. Heiser (2000). "Variance and predictability of precipitation at seasonal-to-interannual timescales," *Journal of Hydrometeorology*, 1, 26-46.

Lawrimore, J.H., and T.C. Peterson (2000). "Pan evaporation trends in dry and humid regions of the United States," *Journal of Hydrometeorology*, 1, 543-546.

Lei, H., and D. Yang (2010). "Interannual and seasonal variability in evapotranspiration and energy partitioning over an irrigated cropland in the North China Plain," *Agricultural and Forest Meteorology*, 150, 581-589.

LeMone, M.A., M. Tewari, F. Chen, J. Alfieri, and D. Niyogi (2008). "Evaluation of the Noah land surface model using data from a fair-weather IHOP_200 day with heterogeneous surface fluxes," *Monthly Weather Review*, 136, 4915-4941.

Lin, Y.-L., R. D. Farley, and H. D. Orville (1983). "Bulk parameterization of the snow field in a cloud model," *Journal of Climate and Applied Meteorology*, 22, 1065–1092.

Lu, L., R.A. Pielke, G.E. Liston, W.J. Parton, D. Ojima, and M. Hartman (2001). "Implementation of a Two-Way Interactive Atmospheric and Ecological Model

and Its Application to the Central United States," *Journal of Climate*, 14, 900-919.

Luo, Y., E.H. Berbery, K.E. Mitchell, and A.K. Betts (2007). "Relationships between land surface and near-surface atmospheric variables in the NCEP North American Regional Reanalysis," *Journal of Hydrometeorology*, 8, 1184-1203.

Maayar, M.E., J.M. Chen, and D.T. Price (2008). "On the use of field measurements of energy fluxes to evaluate land surface models," *Ecological Modeling*, 214 (2008), 293-304.

Mahmood, R., and K.G. Hubbard (2002). "Anthropogenic land use change in the North American tall grass–short grass transition and modification of near surface hydrologic cycle," *Climate Research*, 21, 83–90.

Mahrt, L., and K. Ek (1984). "The influence of atmospheric stability on potential evaporation," *Journal of Climate and Applied Meteorology*, 23, 222-234.

Mahrt, L., and H.L. Pan (1984). "A two-layer model of soil hydrology," *Boundary Layer Meteorology*, 29, 1-20.

Mellor, G. L., and T. Yamada (1982). "Development of a turbulence closure model for geophysical fluid problems," *Reviews of Geophysics and Space Physics*, 20, 851–875.

Mesinger, F., G. DiMego, E. Kalnay, K. Mitchell, P.C. Shafran, W. Ebisuzaki, D. Jović, J. Woollen, E. Rogers, E.H. Berbery, M.B. Ek, Y. Fan, R. Grumbine, W. Higgins, H. Li, Y. Lin, G. Manikin, D. Parrish, and W. Shi (2006). "North American Regional Reanalysis," *Bulletin of American Meteorological Society*, 87, 343-360.

Miao, J.-F., D. Chen, and K. Borne (2007). " Evaluation and comparison of Noah and Pleim-Xiu land surface models in MM5 using GÖTE2001 data: Spatial and temporal variations in near-surface air temperature," *Journal of Applied Meteorology and Climatology*, 46, 1587-1605.

Monin, A.S. and A.M. Obukhov (1954). "Basic laws of turbulent mixing in the surface layer of the atmosphere," *Contrib. Geophys. Inst. Acad. Sci., USSR*, (151), 163–187 (in Russian).

Monteith, J.L. (1973). *Principles of Environmental Physics,* Elsevier, New York, 241pgs.

Monteith, J.L. (1975). *Vegetation and the Atmosphere*, Case Studies, Academic Press, New York, 278pgs.

Morton, F.I. (1983). "Operational estimates of areal evapotranspiration and their significance to the science and practice of hydrology," *Journal of Hydrology*, 66, 1-76.

NCAR (2010). "ARW Version3 Modeling System User's Guide, January 2010-version 3.1," 312 pgs.

NCEP (2010). "WGRIB," Internet: http://www.cpc.ncep.noaa.gov/products/wesley/wgrib.html. Accessed 07/02/2010.

Nishida, K., R.R. Nemani, S.W. Running, and J.M. Glassy (2003). "An operational remote sensing algorithm of land surface evaporation," *Journal of Geophysical Research*, 108(D9), 4270, doi:10.1029/2002JD002062.

Orlowsky, B., and S.I. Seneviratne (2010). "Statistical analyses of land-atmosphere feedbacks and their possible pitfalls," *Journal of Climate*, 23, 3918-3932.

Oudin, L., C. Michel, V. Andréassian, F. Anctil, and C. Loumagne (2005). "Should Bouchet's hypothesis be taken into account in rainfall-runoff modeling? An assessment over 308 catchments," *Hydrological Processes*, 19, 4093-4106.

Ozdogan, M., M. Rodell, H.K. Beaudoing, and D.L. Toll (2010). "Simulating the effects of irrigation over the United States in a land surface model based on satellite-derived agricultural data," *Journal of Hydrometeorology*, 11, 171-184.

Ozdogan, M., G.D. Salvucci, and B.T. Anderson (2006). "Examination of the Bouchet-Morton complementary relationship using a mesoscale climate model and observations under a progressive irrigation scheme," *Journal of Hydrometeorology*, **7**, 235-251.

Pan, H.L., and L. Mahrt (1987). "Interaction between soil hydrology and boundary layer development," *Boundary-Layer Meteorology*, 38, 185-202.

Paulson, C.A. (1970). "The mathematical representation of wind speed and temperature profiles in the unstable atmospheric surface layer," *Journal of Applied Meteorology*, 9, 857-861.

Penman, H.L. (1948). "Natural evaporation from open water, bare soil and grass," *Proceedings of the Royal Society of London*, A193, 120-146.

Pervez, S., J.F. Brown, and S. Maxwell (2008). "Evaluation of remote sensing-based irrigated area map for the conterminous United States," *Percora 17- The Future of Land Imaging… Going Operational*, Denver, Colorado.

Peterson, T.C., V.S. Golubev, and P.Ya. Groisman (1995). "Evaporation losing its strength," *Nature*, 377, 687-688.

Pielke, R.A. (2001). "Influence of the spatial distribution of vegetation and soil on the prediction of cumulus convective rainfall," *Reviews of Geophysics*, 39, 151-177.

Pielke, R.A., and R. Avissar (1990). "Influence of landscape structure on local and regional climate," *Landscape Ecology*, 4, 133-155.

Pielke, R.A., R. Avissar, M. Raupach, A.J. Dolman, X. Zeng, and A.S. Denning (1998). "Interactions between the atmosphere and terrestrial ecosystems: Influence on weather and climate," *Global Change Biology*, 4, 461-475.

Priestley, C.H.B., and R.J. Taylor (1972). "On the assessment of surface heat flux and evaporation using large-scale parameters," *Monthly Weather Review*, 100, 81-92.

Radell, D.B., and C.M. Rowe (2008). "An observational analysis and evaluation of land surface model accuracy in the Nebraska Sand Hills," *Journal of Hydrometeorology*, 9, 601-621.

Rana, G., and N. Katerji (2000). "Measurement and estimation of actual evapotranspiration in the field under Mediterranean climate: A review," *European Journal of Agronomy*, 13(2000), 125-153.

Raupach M.R. (1998). "Influence of local feedbacks on land-air exchanges of energy and carbon," *Global Change Biology*, 4, 477-494.

Rodell, M., P.R. Houser, A.A. Berg, and J.S. Famiglietti (2005). "Evaluatuaion of 10 methods for initializing a land surface model," *Journal of Hydrometeorology*, 6, 146-155.

Roderick, M.L., and G.D. Farquhar (2002). "The cause of decreased pan evaporation over the past 50 years," *Science*, 298, 1410-1411.

Rosero, E., Z.-L.Yang, L.E. Gulden, and G.-Y. Niu (2009). "Evaluating enhanced hydrological representation in Noah LSM over transition zones: Implications for model development," *Journal of Hydrometeorology*, 10, 600-622.

Rosero, E., Z.-L.Yang, T. Wagener, L.E. Gulden, S. Yatheendradas, and G.-Y. Niu (2010). "Quantifying parameter sensivity, interaction, and transferability in hydrologically enhanced versions of the Noah land surface model over transition zones during the warm season," *Journal of Geophysical Research*, 115, D03106, doi:10.1029/2009JD012035.

Rutledge, S. A., and P. V. Hobbs (1984). "The mesoscale and microscale structure and organization of clouds and precipitation in midlatitude cyclones. XII: A diagnostic modeling study of precipitation development in narrow cloud-frontal rainbands," *Journal of the Atmospheric Sciences*, 20, 2949–2972.

Schaake, J.C., V.I. Koren, Q.-Y. Duan, K.E. Mitchell, and F. Chen (1996). "Simple water balance model for estimating runoff at different spatial and temporal scales," *Journal of Geophysical Research*, 101, 7461-7475.

Shelton, M.L. (2009). *Hydroclimatology Perspectives and Applications*, Cambridge University Press, 426 pgs.

Shukla, J., C. Nobre, and P. Sellers (1990). "Amazon deforestation and climate change," *Science*, 247, 1322-1325.

Skamarock, W. C., J. B. Klemp, J. Dudhia, D. O. Gill, D. M.Barker, W. Wang, and J. G. Powers (2005). "A description of the advanced research WRF," *Version 2. NCAR Technical Note*, NCAR/TN-468_STR, 88 pgs.

Sridhar, V., R.L. Elliott, F. Chen, and J.A. Brotzge (2002). "Validation of the NOAH_OSU land surface model using surface flux measurements in Oklahoma," *Journal of Geophysical Research*, 107, 4418, doi:10.1029/2001JD001306.

Sridhar, V., R.L. Elliott, and F. Chen (2003). "Scaling effects on modeled surface energy-balance components using the NOAH-OSU land surface model," *Journal of Hydrology*, 280(2003), 105-123.

Stull, R. (2006). "The atmospheric boundary layer," *Atmospheric Scinence: An Introductory Survey,* J.M. Wallace, and P.V. Hobbs, eds, Elsevier Inc., 375-417.

Suyker, A.E., and S.B. Verma (2009). "Evapotranspiration of irrigated and rainfed maize-soybean cropping systems," *Agricultural and Forest Meteorology*, 149(2009), 443-452.

Szilagyi, J. (2007). "On the inherent asymmetric nature of the complementary relationship of evaporation," *Geophysical Research Letters*, 34, L02405.

Szilagyi, J., and J. Jozsa (2008). "New findings about the complementary relationship-based evaporation estimation methods," *Journal of Hydrology*, 354, 171-186.

Tang, Q., T. Oki, S. Kanae, and H. Hu (2007). "The influence of precipitation variability and partial irrigation within grid cells on a hydrological simulation," *Journal of Hydrometeorology*, 8, 499-512.

Tang, Q., S. Peterson, R.H. Cuenca, Y. Hagimoto, and D.P. Lettenmaier (2009). "Satellite-based near-real-time estimation of irrigation crop water consumption," *Journal of Geophysical Research*, 114, D05114, doi:10.1029/2008JD010854.

Tang, R., Z.L-. Li, and B. Tang (2010). "An application of the Ts-VI triangle method with enhanced edges determination for evapotranspiration estimation from MODIS data in arid and semi-arid regions: Implementation and validation," *Remote Sensing of Environment*, 114(2010), 540-551.

Twin Falls Canal Company (2011)."System Information," Internet: http://www.tfcanal.com/system_information.htm. Accessed 02/10/2011.

USDA (2010). "2009 Cropland Data Layer (CDL)," Internet: http://www.nass.usda.gov/research/Cropland/SARS1a.htm. Accessed 03/25/2010.

Walter, M.T., D.S. Wilks, J.Y. Parlange, and R.L. Schneider (2004). "Increasing evapotranspiration from the conterminous United States," *Journal of Hydrometeorology*, 5, 405-408.

Wilson, K., A. Goldstein, E. Falge, M. Aubinet, D. Baldocchi, P. Berbigier, C. Bernhofer, R. Ceulemans, H. Dolman, C. Field, A. Grelle, A. Ibrom, B.E. Law, A. Kowalski, T. Meyers, J. Moncrieff, R. Monson, W. Oechel, J. Tenhunen, R. Valentini, and S. Verma (2002). "Energy balance closure at FLUXNET sites," *Agricultural and Forest Meteorology*, 113 (2002), 223-243.

Xiu, A., and J.E. Pleim (2001). "Development of a land surface model. Part I: Application in a mesoscale meteorological model," *Journal of Applied Meteorology*, 40, 192-209.

Xu, C.-Y., and V.P. Singh (2005), "Evaluation of three complementary relationship evapotranspiration models by water balance approach to estimate actual regional

evapotranspiration in different climatic regions," *Journal of Hydrology*, 308, 105-121.

Yan, H., and H.H. Shugart (2010). "An air relative-humidity-based evapotranspiration model from eddy covariance data," *Journal of Geophysical Research*, 115, D16106, doi:10.1029/2009JD13598.

Yang, Z.-L., R.E. Dickinson, A. Henderson-Sellers, and A.J. Pitman (1995). "Preliminary study of spin-up processes in land surface models with the first stage data of project for intercomparison of land surface parameterization schemes phase 1(a)," *Journal of Geophysical Research*, 100, D8, 16,553-16,578.

Yang, D., F. Sun, Z. Liu, Z. Cong, and Z. Lei (2006). "Interpreting the complementary relationship in non-humid environments based on the Budyko and Penman hypotheses," *Geophysical Research Letters*, 33, L18402, doi:10.1029/2006GL027657.

Zilitinkevich, S.S. (1995). "Non-local turbulent transport: Pollution dispersion aspects of coherent structure of convective flows, air pollution III," *Air Pollution Theory and Simulations,* H. Power, N. Moussiopoulos, and C.A. Brebbia, eds., Vol. I, Computational Mechanics Publications, 53-60.

APPENDIX A

Vegetation Parameter Table

Table A.1. Vegetation Parameter Table for MODIS-Based Classification. The 17 Columns Include (1) Vegetation Type Number, (2) SHDFAC - Plant Shade Factor, (3) NROOT - Number of Root Layers, (4) RS - Stomatal Resistance, (5) RGL - Parameters Used in Radiation Stress Function, (6) HS - Parameter Used in Vapor Pressure Deficit Function, (7) SNUP - Threshold Snow Depth (in Water Equivalent m), (8) MAXALB - Upper Bound on Maximum Albedo over Deep Snow, (9) LAIMIN - Minimum Leaf Area Index, (10) LAIMAX - Maximum Leaf Area Index, (11) EMISSMIN - Minimum Emissivity, (12) EMISSMAX- Maximum Emissivity, (13) ALBEDOMIN- Minimum Albedo, (14) ALBEDOMAX- Maximum Albedo, (15) Z0MIN - Minimum Roughness Length, (16) Z0MAX - Maximum Roughness Length, and (17) Vegetation Type (Page 146).

(1)	(2)	(3)	(4)	(5)	(6)	(7)	(8)	(9)	(10)	(11)	(12)	(13)	(14)	(15)	(16)	(17)
1	0.7	4	125	30	47.35	0.08	52	5	6.4	0.95	0.95	0.12	0.12	0.5	0.5	Type 1
2	0.95	4	150	30	41.69	0.08	35	3.08	6.48	0.95	0.95	0.12	0.12	0.5	0.5	Type 2
3	0.7	4	150	30	47.35	0.08	54	1	5.16	0.93	0.94	0.14	0.15	0.5	0.5	Type 3
4	0.8	4	100	30	54.53	0.08	58	1.85	3.31	0.93	0.93	0.16	0.17	0.5	0.5	Type 4
5	0.8	4	125	30	51.93	0.08	53	2.8	5.5	0.93	0.97	0.17	0.25	0.2	0.5	Type 5
6	0.7	3	300	100	42	0.03	60	0.5	3.66	0.93	0.93	0.25	0.3	0.01	0.05	Type 6
7	0.7	3	170	100	39.18	0.035	65	0.6	2.6	0.93	0.95	0.22	0.3	0.01	0.06	Type 7
8	0.7	3	300	100	42	0.03	60	0.5	3.66	0.93	0.93	0.25	0.3	0.01	0.05	Type 8
9	0.5	3	70	65	54.53	0.04	50	0.5	3.66	0.92	0.92	0.2	0.2	0.15	0.15	Type 9
10	0.8	3	40	100	36.35	0.04	70	0.52	2.9	0.92	0.96	0.19	0.23	0.1	0.12	Type 10
11	0.6	2	70	65	55.97	0.015	59	1.75	5.72	0.95	0.95	0.14	0.14	0.3	0.3	Type 11
12	0.8	3	40	100	36.25	0.04	66	1.56	5.68	0.92	0.985	0.17	0.23	0.05	0.15	Type 12
13	0.1	1	200	999	999	0.04	46	1	1	0.88	0.88	0.15	0.15	0.5	0.5	Type 13
14	0.8	3	40	100	36.25	0.04	68	2.29	4.29	0.92	0.98	0.18	0.23	0.05	0.14	Type 14
15	0	1	999	999	999	0.02	82	0.01	0.01	0.95	0.95	0.55	0.7	0.001	0.001	Type 15
16	0.01	1	999	999	999	0.02	75	0.1	0.75	0.9	0.9	0.38	0.38	0.01	0.01	Type 16
17	0	0	100	30	51.75	0.01	70	0.01	0.01	0.98	0.98	0.08	0.08	0.0001	0.0001	Type 17
18	0.6	3	150	100	42	0.025	55	0.41	3.35	0.93	0.93	0.15	0.2	0.3	0.3	Type 18
19	0.6	3	150	100	42	0.025	60	0.41	3.35	0.92	0.92	0.15	0.2	0.15	0.15	Type 19
20	0.3	2	200	100	42	0.02	75	0.41	3.35	0.9	0.9	0.25	0.25	0.05	0.1	Type 20

Vegetation Types

Type 1   - Evergreen Needle Leaf Forest

Type 2   - Evergreen Broad Leaf Forest

Type 3   - Deciduous Needle Leaf Forest

Type 4   - Deciduous Broad Leaf Forest

Type 5   - Mixed Forests

Type 6   - Closed Shrublands

Type 7   - Open Shrublands

Type 8   - Woody Savannas

Type 9   - Savannas

Type 10   - Grasslands

Type 11   - Permanent Wetlands

Type 12   - Croplands

Type 13   - Urban and Built-Up

Type 14   - Croplands/ Natural Vegetation Mosaic

Type 15   - Snow and Ice

Type 16   - Barren or Sparsely Vegetated

Type 17   - Water

Type 18   - Wooded Tundra

Type 19   - Mixed Tundra

Type 20   - Barren Tundra

APPENDIX B

Soil Parameter Table

Table B.1. Soil Parameter Table. The Column Names Stands for: BB - B Parameter, DRYSMC - Air Dry Soil Moisture Content, F11 - Soil Thermal Diffusivity/Conductivity Coefficient, MAXSMC - Maximum Soil Moisture Content, REFSMC - Reference Soil Moisture Content, SATPSI - Saturated Soil Potential Coefficient, SATDK - Saturated Soil Conductivity Coefficient, SATDW - Saturated Soil Diffusivity Coefficient, WLTSMC - Wilting Point Soil Moisture Content, QTZ - Soil Quartz Content. Soil Types Names Are on Page 149.

Soil Type Number	BB	DRYSMC	F11	MAXSMC	REFSMC	SATPSI	SATDK	SATDW	WLTSMC	QTZ	Soil Type
1	2.79	0.01	-0.472	0.339	0.236	0.069	1.07E-06	6.08 E-07	0.01	0.92	Type 1
2	4.26	0.028	-1.044	0.421	0.383	0.036	1.41 E-05	5.14 E-06	0.028	0.82	Type 2
3	4.74	0.047	-0.569	0.434	0.383	0.141	5.23 E-06	8.05 E-06	0.047	0.6	Type 3
4	5.33	0.084	0.162	0.476	0.36	0.759	2.81 E-06	2.39 E-05	0.084	0.25	Type 4
5	5.33	0.084	0.162	0.476	0.383	0.759	2.81 E-06	2.39 E-05	0.084	0.1	Type 5
6	5.25	0.066	-0.327	0.439	0.329	0.355	3.38 E-06	1.43 E-05	0.066	0.4	Type 6
7	6.66	0.067	-1.491	0.404	0.314	0.135	4.45 E-06	9.90 E-06	0.067	0.6	Type 7
8	8.72	0.12	-1.118	0.464	0.387	0.617	2.04 E-06	2.37 E-05	0.12	0.1	Type 8
9	8.17	0.103	-1.297	0.465	0.382	0.263	2.45 E-06	1.13 E-05	0.103	0.35	Type 9
10	10.73	0.1	-3.209	0.406	0.338	0.098	7.22 E-06	1.87 E-05	0.1	0.52	Type 10
11	10.39	0.126	-1.916	0.468	0.404	0.324	1.34 E-06	9.64 E-06	0.126	0.1	Type 11
12	11.55	0.138	-2.138	0.468	0.412	0.468	9.74 E-07	1.12 E-05	0.138	0.25	Type 12
13	5.25	0.066	-0.327	0.439	0.329	0.355	3.38 E-06	1.43 E-05	0.066	0.05	Type 13
14	0	0	0	1	0	0	0	0	0	0.6	Type 14
15	2.79	0.006	-1.111	0.2	0.17	0.069	1.41 E-04	1.36 E-04	0.006	0.07	Type 15
16	4.26	0.028	-1.044	0.421	0.283	0.036	1.41 E-05	5.14 E-06	0.028	0.25	Type 16
17	11.55	0.03	-10.472	0.468	0.454	0.468	9.74 E-07	1.12 E-05	0.03	0.6	Type 17
18	2.79	0.006	-0.472	0.2	0.17	0.069	1.41 E-04	1.36 E-04	0.006	0.52	Type 18
19	2.79	0.01	-0.472	0.339	0.236	0.069	1.07 E-06	6.08 E-07	0.01	0.92	Type 19

<u>Soil Types</u>

Type 1   - Sand

Type 2   - Loamy Sand

Type 3   - Sandy Loam

Type 4   - Silt Loam

Type 5   - Silt

Type 6   - Loam

Type 7   - Sandy Clay Loam

Type 8   - Silty Clay Loam

Type 9   - Clay Loam

Type 10   - Sandy Clay

Type 11   - Silty Clay

Type 12   - Clay

Type 13   - Organic Material

Type 14   - Water

Type 15   - Bedrock

Type 16   - Other (Land-Ice)

Type 17   - Playa

Type 18   - Lava

Type 19   - White Sand

APPENDIX C

General Parameters

General Parameters

- SLOPE_DATA

  9
  0.1
  0.6
  1.0
  0.35
  0.55
  0.8
  0.63
  0.0
  0.0

- SBETA_DATA   = -2.0

- FXEXP_DATA   = 2.0

- CSOIL_DATA   = 2.00E+6

- SALP_DATA   = 2.6

- REFDK_DATA   = 2.0E-6

- REFKDT_DATA = 3.0

- FRZK_DATA   = 0.15

- ZBOT_DATA   = -8.0

- CZIL_DATA   = 0.1

- SMLOW_DATA = 0.5

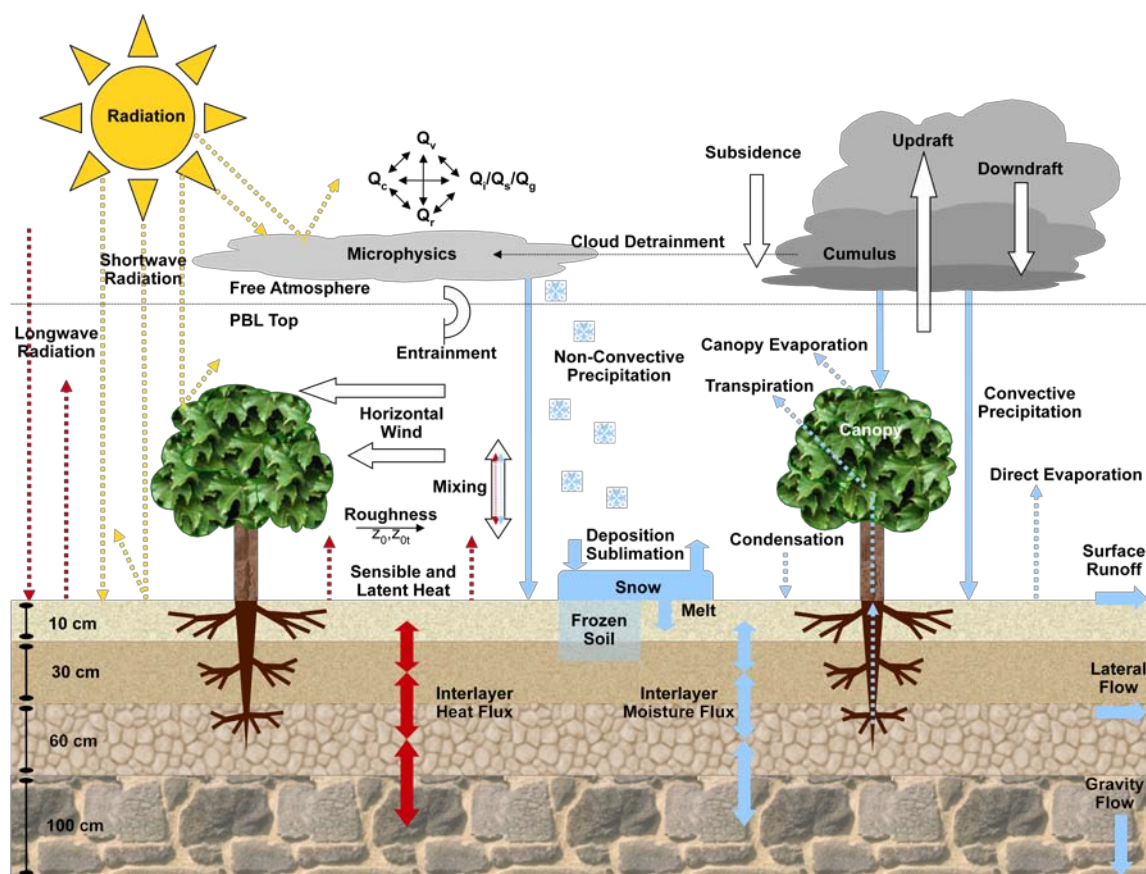- SMHIGH_DATA = 3.0

APPENDIX D

Schematic Diagram of WRF
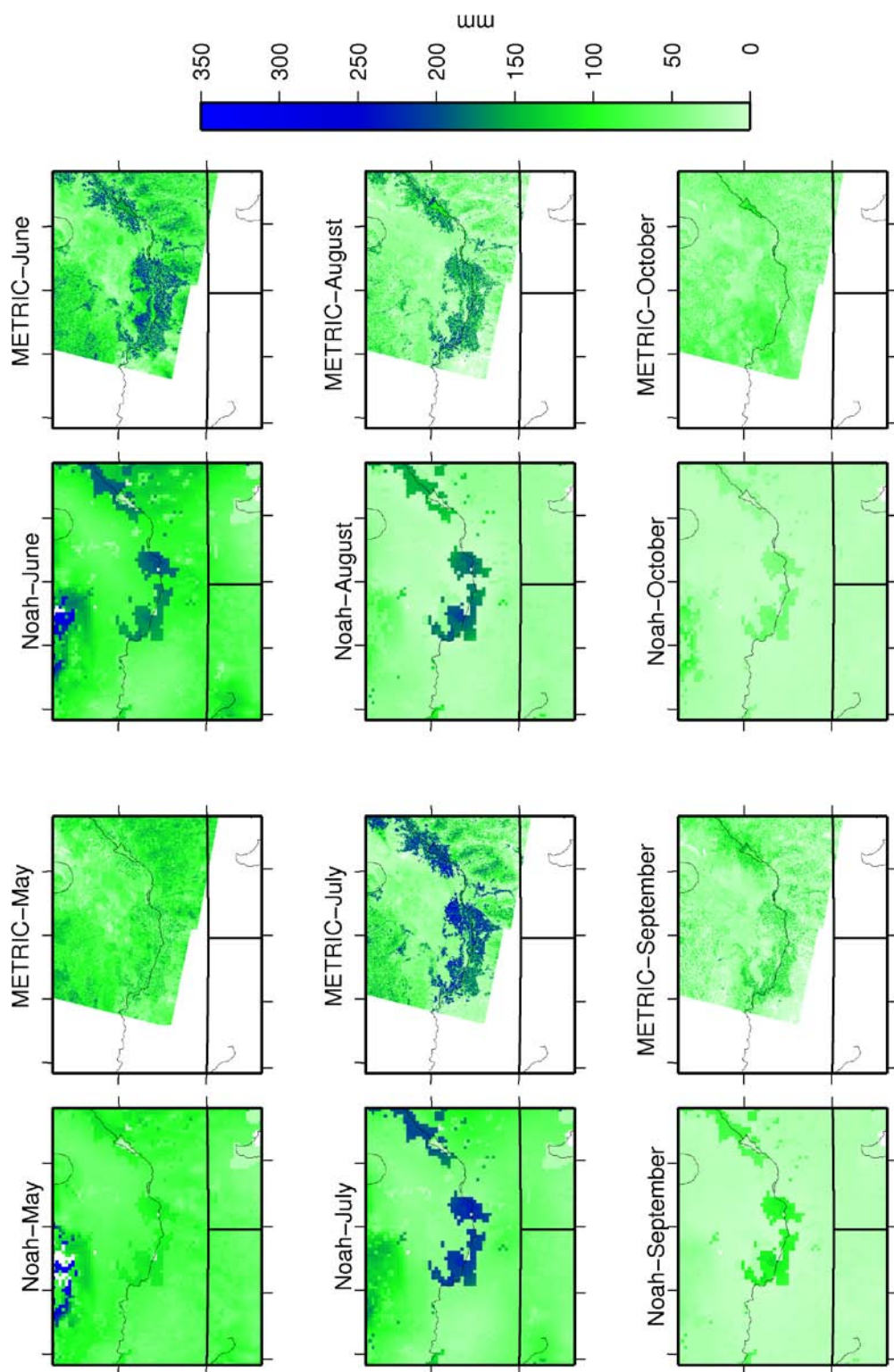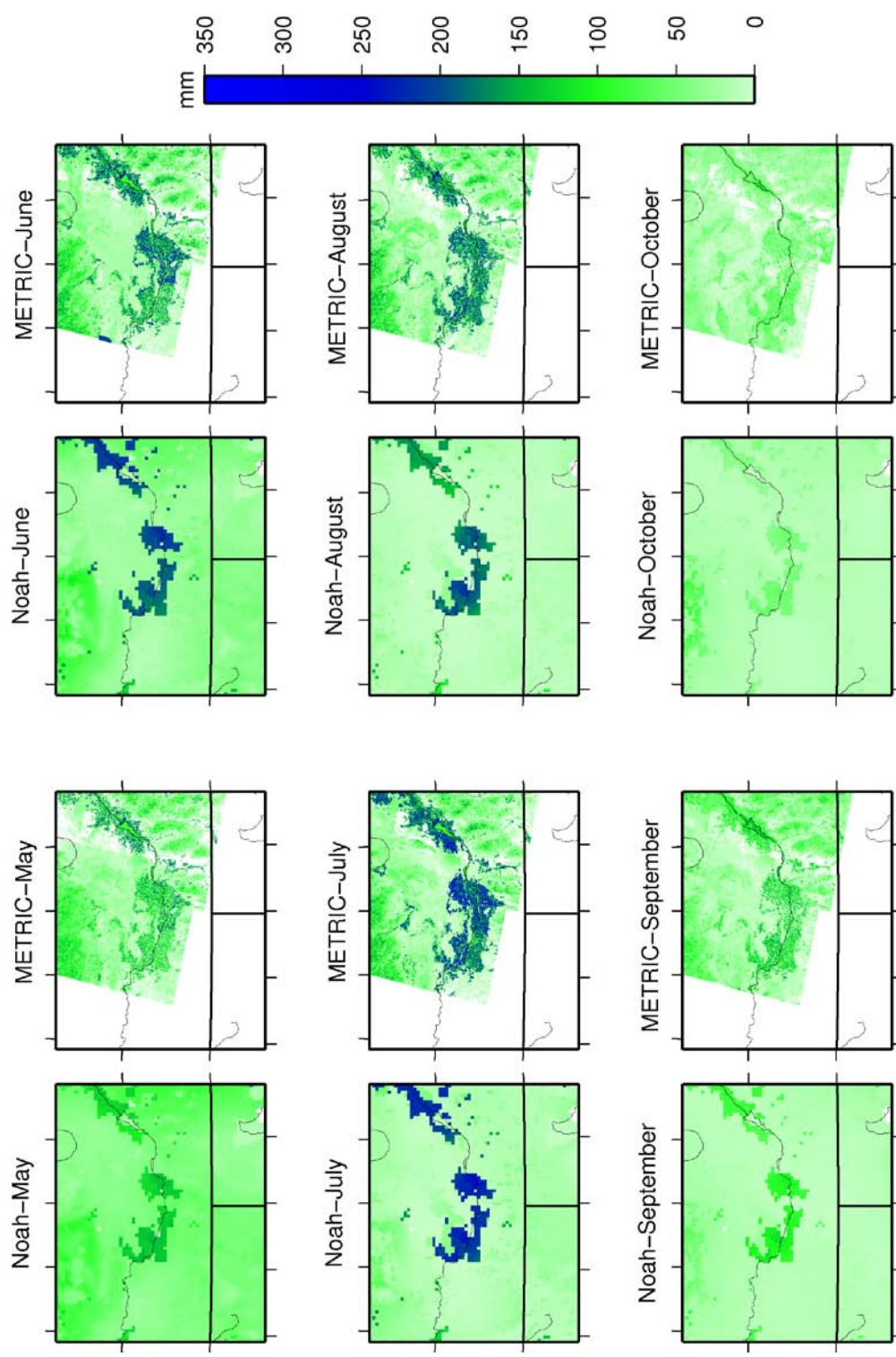
**Figure D.1. Schematic Diagram of WRF.**

APPENDIX E

Comparison of METRIC ET Maps with Noah Simulated Spatial Maps for the

Months in the Growing Season in the Years 1996, 2000, and 2002.

Figure E.1. Spatial Distribution of Monthly Total ET from METRIC and Noah LSM from May to October in 1996.

Figure E.2. Spatial Distribution of Monthly Total ET from METRIC and Noah LSM from May to October in 2000.
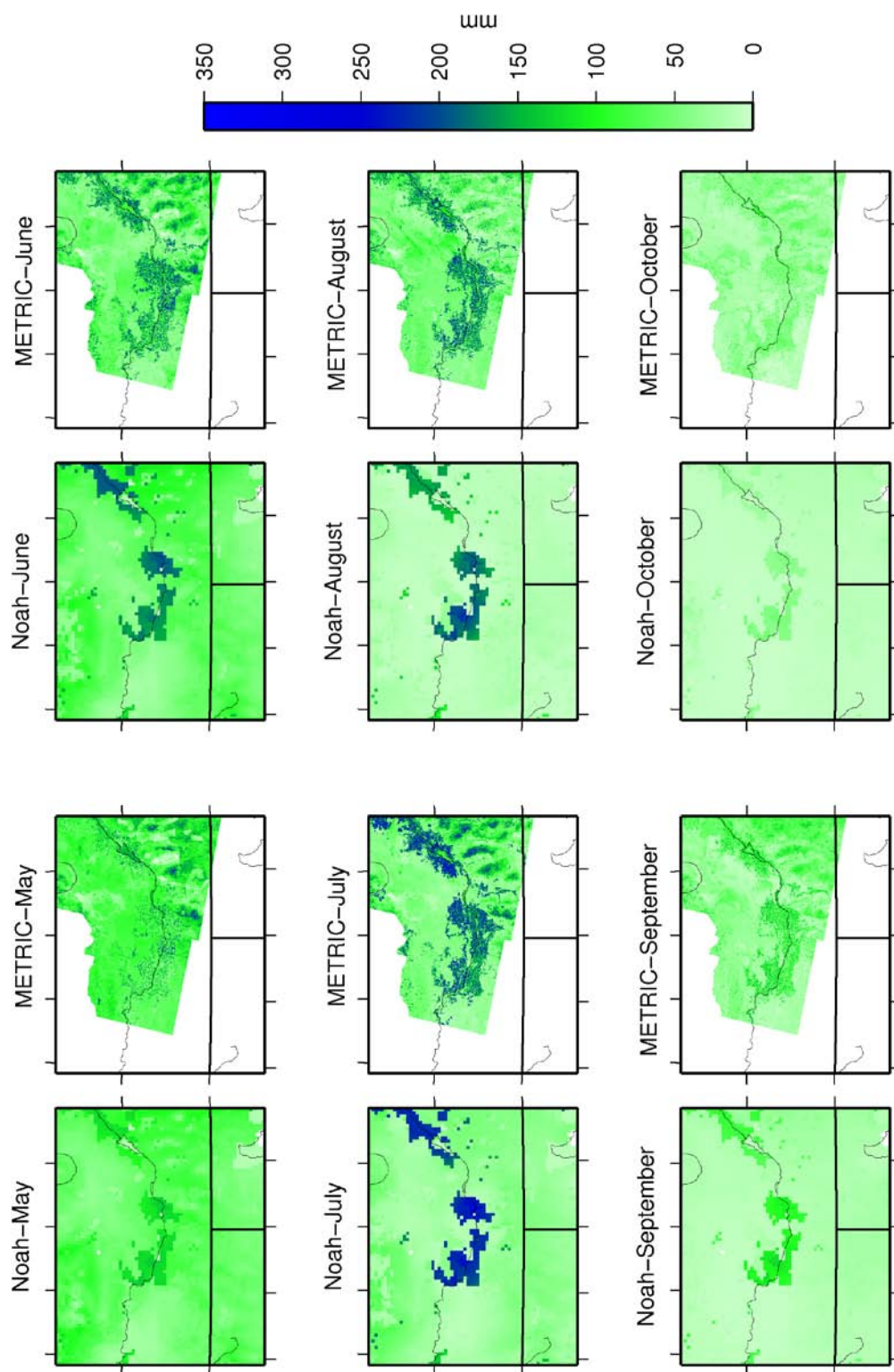
Figure E.3. Spatial Distribution of Monthly Total ET from METRIC and Noah LSM from May to October in 2002.